Korea Institute of Science and Technology

Green City Technology Institute (GCTI)

GREEN CITY MEGA PLAN

Empowering Sustainable Energy and Environmental Network

KIST Today Vol. 5 No. 2 November 2012

Vol. 5 No. 2 November 2012
ISSN 2005-9043

Leading to the world of tomorrow

KIST Today

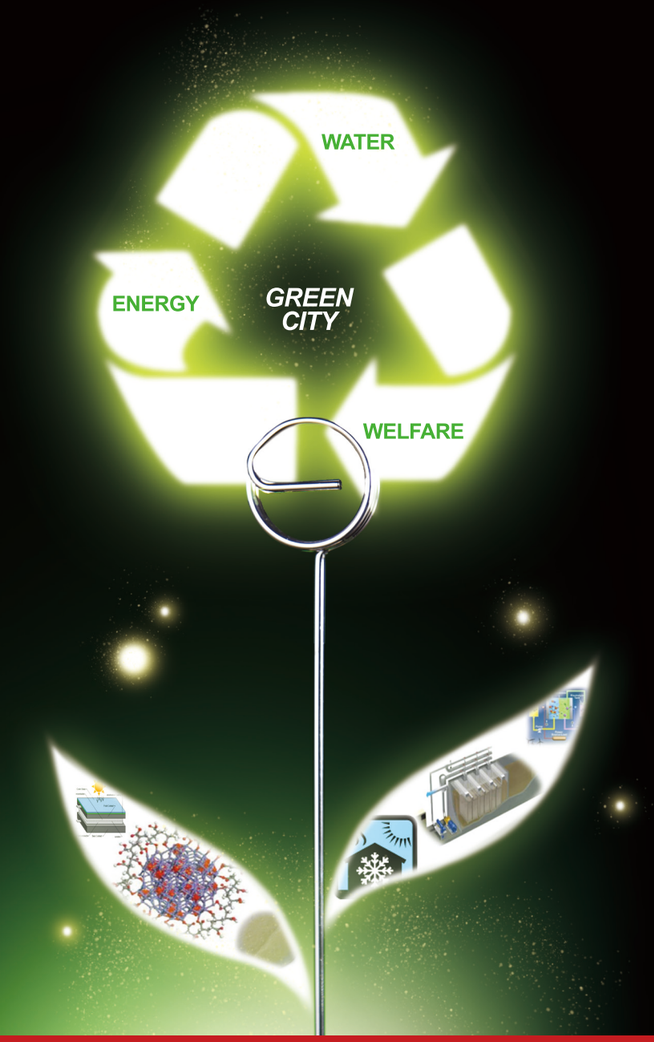

GCTI (Green City Technology Institute)

The goal of the GCTI of KIST is to support both national and global agendas relating to urban energy and the environment. The activities of the institute consists of the development in energy and environmental technologies in order to create a "green city with a high-quality welfare system" that is efficient in the resource consumption such as energy, natural water and air as well as information technology in a sustainable way, leading to a dramatic reduction both in greenhouse gases through near zero carbon emission and in water and air pollutants through cyclic metabolism.

VISION

To develop an eco-friendly self-sustainable green city through the convergence of core technologies

- Develop the fundamental technologies for green energy
- Apply core technologies to a model green city
- Commercialize green technology
- Become a Global Leader in Sustainable Energy and Environmental Research

RESEARCH AREAS

- Water Resource Cycle Research
- Environment, Health & Welfare Research
- Urban Energy Systems Research
- Energy Convergence Research
- Integrated Risk Research

Korea Institute of Science and Technology

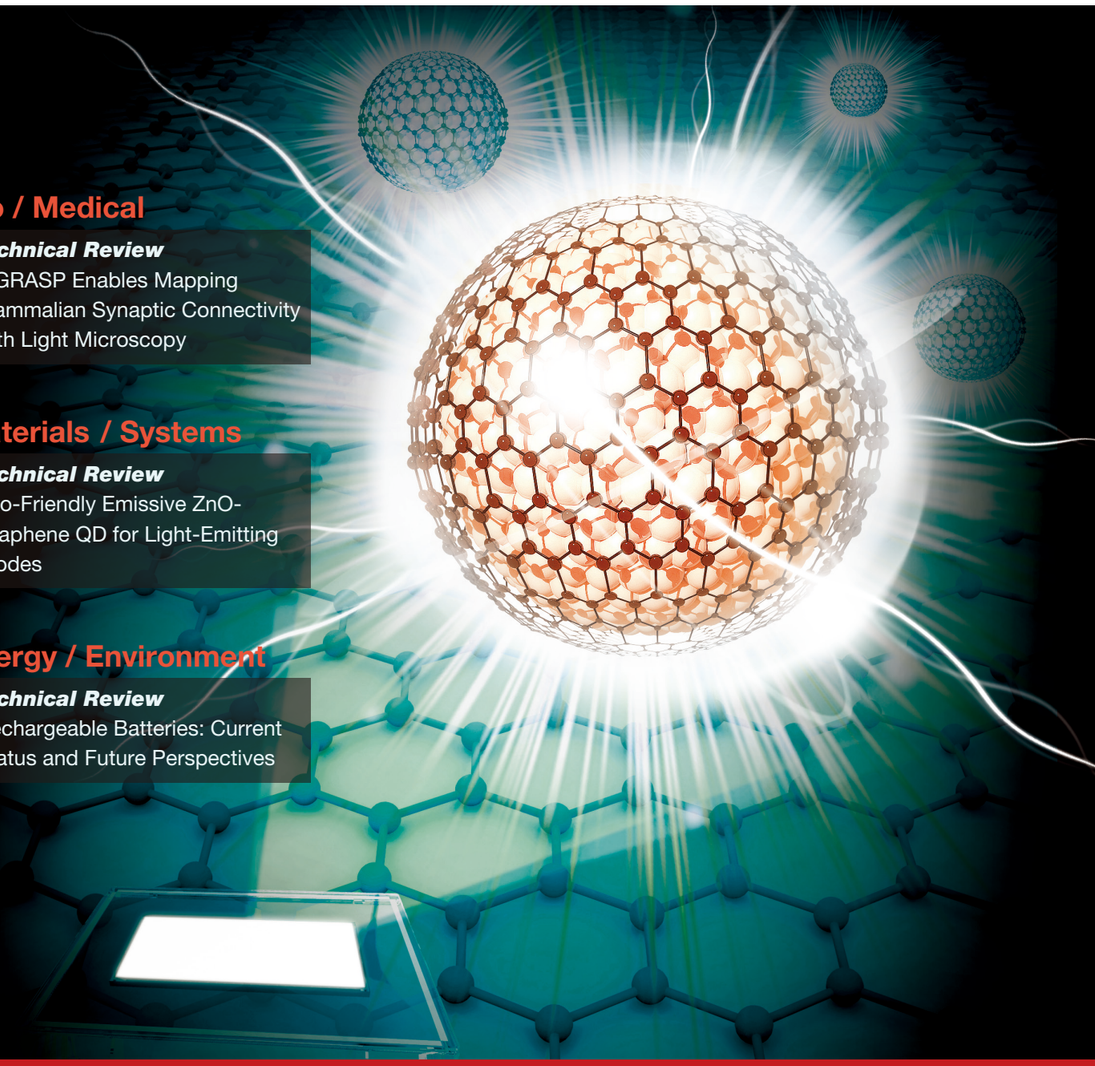

Bio / Medical

- ***Technical Review***
  mGRASP Enables Mapping Mammalian Synaptic Connectivity with Light Microscopy

Materials / Systems

- ***Technical Review***
  Eco-Friendly Emissive ZnO-Graphene QD for Light-Emitting Diodes

Energy / Environment

- ***Technical Review***
  Rechargeable Batteries: Current Status and Future Perspectives

Contents

Foreword

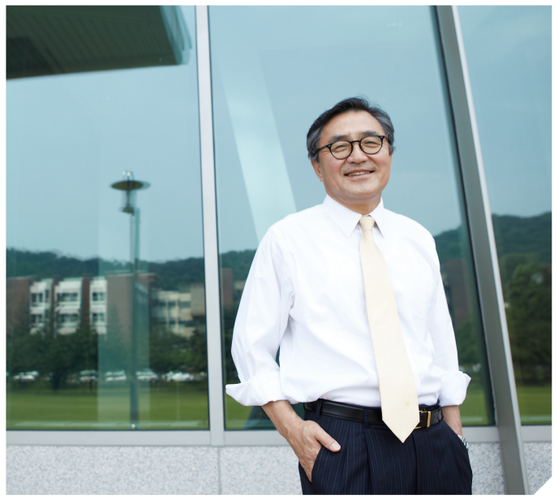

Beginning with its first issue in the summer of 2008, *KISToday* has been providing its readers with highlights of the many exciting developments taking place in our research community. We've continued to expand and adapt the content of our magazine, making it more comprehensive and highlighting the ways we are using our expertise and cutting-edge research to put Korea at the heart of global scientific and technological leadership.

Last summer KIST hosted the 1st Hong-Neung Forum. Research and educational institutions located within the Hong-Neung research complex, long a national mecca for economics, science and technology, and advanced education, gathered to discuss ways to establish Hong-Neung as a leading international think-tank and develop it as a unique brand name identified with Korea. The Hong-Neung Forum was an essential first step to identify and develop ways to capitalize on the accumulated knowledge and expertise of the entire Hong-Neung research complex to benefit not only Korean society but societies worldwide.

One particularly exciting aspect of the Forum involved discussion of plans for the future growth of the Hong-Neung complex in areas related to green technology. KIST lent considerable expertise to this discussion since it already has successfully established a green technology research center in Hong-Neung. Though much work lies ahead, we are confident that KIST as well as its fellow institutions in Hong-Neung will help develop innovative solutions for a cleaner, healthier, and more sustainable future. We look forward to describing this research in upcoming issues.

Dr. Kil-Choo Moon
President of KIST

[**Technical Review**]

mGRASP Enables Mapping Mammalian Synaptic Connectivity with Light Microscopy

Chaehyun Yook
Center for Functional Connectomics,
CFC-KAIST PhD program
chaehyun@kaist.ac.kr

Jinhyun Kim
Center for Functional Connectomics
kimj@kist.re.kr

Introduction

More than a century ago, the visionary Spanish neuroanatomist Santiago Ramón Cajal (Nobel Laureate, 1906) suggested the so-called "neuron-doctrine," the idea that neurons are structural and functional units in the brain, and explored the complex architecture of circuit networks between neurons. Neurons in networks communicate with one another through a special bridgelike structure called a synapse. Now, neuroscientists continue to investigate neuronal circuits by developing advanced techniques to map synaptic connectivity [1-3]. The focus of this technical review is to introduce a new technology called mGRASP for mapping the location of synapses quickly, accurately, and with high spatial resolution.

Background

In previous studies, the extent of overlap between the axonal arbor of a presynaptic neuron and the dendritic arbor of a postsynaptic neuron has been used to infer the presence of synaptic connectivity [4], based on the fact that synapse formation requires physical contacts. However, this method can only provide an estimate of the probability of a connection, as it has been shown that less than half of the axons within reach of a given postsynaptic dendrite actually form functional synaptic contacts [5].

The presence and statistical characteristics of actual synaptic connectivity can be determined by using nanometer-resolution electron microscopy (EM). But even with recent advances in EM-associated methodology, it remains a relatively time- and labor-intensive and volume-limited endeavor to reconstruct substantial regions of neuronal tissue [6, 7]. Recently, fluorescence-based methods such as array tomography, Brainbow, trans-synaptic tracing, and green fluorescent protein (GFP) reconstitution across synaptic partners (GRASP) have emerged as alternative approaches for mapping neuronal circuitry, enabled by sophisticated techniques for genetic manipulation of animal models [8–11].

In the GRASP technique, GFP is split into two fragments (called GFP1–10 and GFP11), which makes them non-fluorescent individually. Each of these two split-GFP fragments then get tethered to the specified synaptic membranes of two separate neuronal populations, i.e., GFP11 is tethered to presynaptic membranes and GFP1-10 is tethered to postsynaptic membranes. When two neurons, each expressing one of the fragments, are tightly opposed through a synaptic cleft, functional complementation of split GFP occurs, fluorescent GFP is reconstituted (Figure 1a), and the location of synapses can be visualized by GFP fluorescence. To date, GRASP has been applied to map synaptic connectivity in the nematode and the fruit fly [11, 12]. However, before GRASP can be used for synapse visualization in the mammalian brain, several important modifications are required because of the variability of synaptic architecture across organisms [13].

Here we describe optimized GRASP for mapping long-range circuits as well as microcircuits in the mammalian brain (mGRASP). Using computer simulation-based protein design, we engineered chimeric synaptic mGRASP components that would target split-GFP fragments to pre- and postsynaptic membranes separately and match the ~20-nm-wide synaptic cleft of mammalian synapses. We validated the synaptic distribution of the designed pre- and postsynaptic mGRASP components with electron microscopy, verified that the reconstitution of mGRASP could be detected in well-studied synapses of various brain regions (for example, Schaffer collateral synapses of the hippocampus), and determined that our technique led to no substantial change in synapse formation and elimination. We also verified that mGRASP can be used specifically to detect actual synapses, not potential synapses, by examining sites where synapses are known to be absent even if fully surrounded by nontargeting axons. In addition, we report analysis strategies and computational programs for the three-dimensional reconstruction of neurons that allowed us to investigate

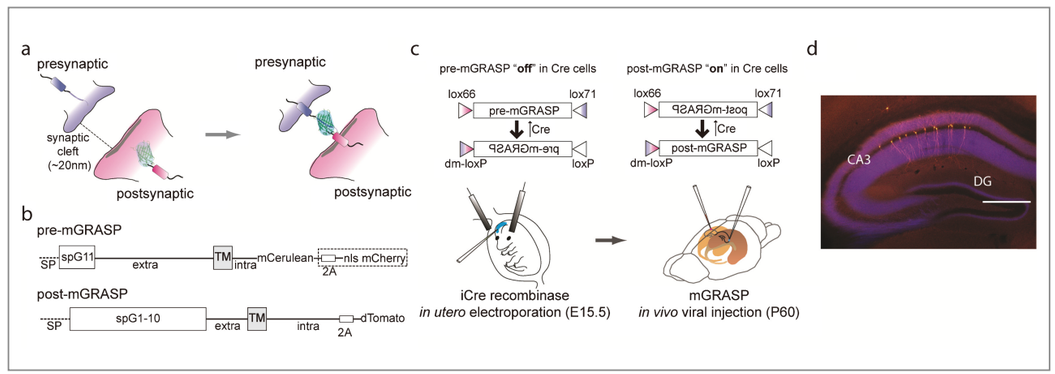

Figure 1. Synaptic mGRASP components and gene delivery strategy.

the localization and detailed subcellular distribution of synapses. Our results show that mGRASP is a powerful tool to characterize both inhibitory and excitatory neuronal circuits in the mouse brain.

mGRASP design and gene-delivery strategy

Our design goals were to produce pre- and postsynaptic proteins that would allow split-GFP reconstitution over synaptic clefts in the mouse brain without causing spurious synapse formation or inappropriate reconstitution at nonsynaptic regions. To do so, we searched for suitable transmembrane molecules that are localized restrictedly at synapses. In the mammalian central nervous system, overexpression of certain synaptic molecules, such as neurexin and neuroligin, can cause changes in synapse morphology leading to increased maturation of excitatory synapses and respective changes in physiology and behavior [14–16]. Thus, we designed *in silico* chimeric pre- and postsynaptic mGRASP components, synthesized from publicly available sequences (US National Center for Biotechnology Information; NCBI) and codon-optimized for Mus musculus (Online Methods). We wanted to ensure that mGRASP components were targeted to and maintained at synapses and that the extracellular domains including the split-GFP fragments fit appropriately in the synaptic cleft (Figure 1a).

Both pre- and postsynaptic mGRASP components were composed of an N-terminal signal peptide followed by a split-GFP fragment, an extracellular domain, a transmembrane domain, an intracellular domain and a fluorescent protein for neurite visualization (Figure 1b). For the presynaptic mGRASP component (pre-mGRASP), we used as a signal peptide the first 29 residues of the nematode β-integrin (PAT-3, residues 1–29) followed by the 16-residue GFP11, two Gly-Gly-Gly-Gly-Ser (GGGGS) linkers, and the extracellular domain and predicted transmembrane domain of human CD4-2 (residues 25–242, as in the original GRASP) [11]. To target and maintain this construct specifically in presynaptic sites, we included as an intracellular domain the 55-residue C terminus of rat neurexin-1β (residues 414–468) containing the PDZ-binding motif necessary for endoplasmic reticulum and Golgi exit and synaptic targeting [14].

Finally, to visualize pre-mGRASP, we fused monomeric (m)Cerulean to the construct. For the postsynaptic mGRASP component (post-mGRASP), we used mouse neuroligin-1 as the main skeleton. Full-length neuroligin-1 contains 575 residues of a catalytically inactive esterase domain (residues 52–626) that are known to interact with presynaptic neurexin, leading to synapse formation [15]. Thus, we deleted residues 52–626 completely to avoid nonspecific synaptogenesis via interactions with endogenous neurexin. We inserted the 648-residue GFP1-10 fragment after the signal peptide (residues 1–49) of the esterase-truncated neuroligin-1. The rest of post-mGRASP consisted of the 71-residue extracellular domain, the 19-residue predicted transmembrane domain and the 127-residue C terminus of mouse neuroligin-1. In addition, we fused dimeric (d)Tomato to the cytosolic end of post-mGRASP via the self-cleavable 2A peptide [17] to visualize the morphology of the postsynaptic cells.

Before deciding on these configurations we attempted other combinations that all led to failures: different signal peptides (for example, of neurexin and the Drosophila cuticle protein CP3); different extracellular and transmembrane domains (for example, of neurexin and CD8); and different intracellular domains (for example, of Kv4.2 and the myosin-binding domain of mouse melanophilin). Most of these constructs resulted in cytotoxicity, inadequate synaptic expression and/or no fluorescence reconstitution (Supplementary Figure 1). Notably, the CD4-based GRASP system, previously used in the nematode and the fruit fly [11, 12] appeared to be nonspecific for endogenous synapse visualization in mammals. Rat hippocampal neurons separately transfected with vectors containing CD4-GFP1-10 and CD4-GFP11 and cultured together, as well as mouse brain tissue transduced with recombinant adeno-associated virus (rAAV) vectors for the expression of CD4–GFP1-10 and CD4-GFP11, showed nonspecific line-like fluorescence patterns in addition to the expected puncta-like fluorescence.

Our next challenge was to deliver the pre- and post-mGRASP components into defined neuronal populations without expressing them together in the same cell. To test our pre- and post-mGRASP constructs in the mouse brain, we focused on the well-studied CA3-CA1 connectivity of the hippocampus. We sought to sparsely label postsynaptic CA1 neurons to enable resolution of individual cells and their dendrites in a way suitable for subsequent automated reconstruction. To achieve cell type–specific and sparse gene delivery, we used a combination of in utero electroporation [18] of Cre recombinase expression plasmids with spatially restricted injection of Cre recombinase–dependent or –independent rAAV vectors for the expression of mGRASP components to ipsilateral and contralateral sides of the hippocampus (Figure 1c). Thus we achieved selective and sparse labeling in ~50–200 postsynaptic CA1 pyramidal neurons without overlap with presynaptic CA3 neurons (Figure 1d).

The combination of gene-delivery strategies allowed us not only to control the sparseness of labeling but also to avoid long-term expression of exogenous synaptic proteins. In addition, the Cre recombinase–dependent viral vectors allow a wide choice of cell type–specific expression of mGRASP components by use of preexisting and newly generated Cre transgenic mouse lines (for example, Gene Expression Nervous System Atlas; GENSAT). To test this, we applied Cre recombinase–dependent 'switch off ' pre-mGRASP and 'switch on' post-mGRASP to mouse lines with cell type–specific Cre recombinase expression (Figure 1c). As discussed below, this strategy is especially suitable for labeling of distinct but spatially close cell populations and for mapping local synaptic connectivity.

Synaptic expression of pre-and post-mGRASP

To determine the synaptic expression of pre- and post-mGRASP, we introduced them separately into CA3 and CA1 neurons in the mouse hippocampus and examined their distribution using light and electron microscopy (Figure 2). In the CA3 region, injected with rAAV vector expressing pre-mGRASP fused to mCerulean (aavCAG–pre-mGRASP–mCerulean), we detected blue fluorescence only in axonal projections, making it difficult to identify the infected neurons (Figure 2). Thus, to facilitate the visualization of infected cells, we generated a new construct including mCerulean-fused pre-mGRASP followed by the self-cleavable 2A peptide and nucleus-targeted nuclear localization sequence (NLS)-mCherry (aavCAG–pre-mGRASP– mCerulean-2A-NLS-mCherry). We injected rAAV vectors for the Cre recombinase–independent expression of pre-mGRASP– mCerulean-2A-NLS-mCherry into the CA3 area (Figure 1b). Under light microscopy, we observed strongly labeled blue axons in both ipsilateral and contralateral sides of hippocampi. High-magnification images of infected CA3 areas showed

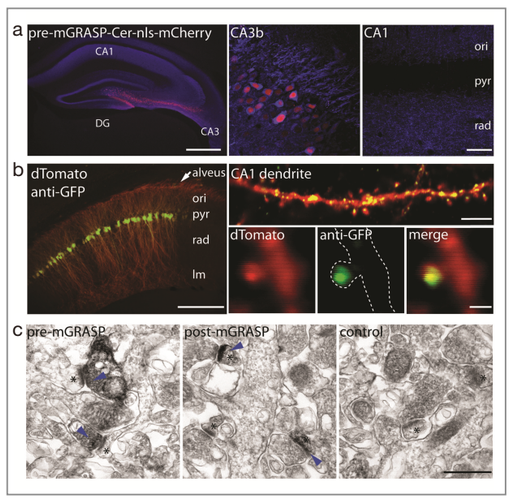

Figure 2. Synaptic expression of mGRASP components.

infected cell nuclei labeled with NLS-mCherry and their mCerulean-labeled axonal projections, whereas images of the non-infected CA1 area showed only axonal projections of CA3 neurons (Figure 2a) and confirmed primary axonal expression of pre-mGRASP. In addition, under electron microscopy, silver-gold immunolabeling of mCerulean with an antibody to GFP allowed us to confirm that the pre-mGRASP component was effectively targeted to presynaptic sites (Figure 2c).

Detection of mGRASP in the mouse brain

We next assayed mGRASP reconstitution in the mouse brain. As we aimed to reconstruct postsynaptic neurons, we labeled postsynaptic CA1 neurons sparsely while densely labeling presynaptic CA3 neurons. We used in utero electroporation to provide plasmid encoding improved (i)Cre recombinase [19] (paavCAG-iCre) to the right ventricle of embryos, and, two months later, we injected rAAV vectors into the same mice for the expression of Cre recombinase–independent pre-mGRASP (aavCAG-pre-mGRASP-mCerulean) and Cre recombinase–dependent 'switch-on' post-mGRASP (aavCAG-Jx-rev–post-mGRASP–2A-dTomato) components into CA3 neurons of the left hemisphere and CA1 neurons of the right hemisphere, respectively. We found that, although neither split-GFP fragment fluoresced when expressed individually, mGRASP was reconstituted trans-synaptically, revealing discrete puncta of fluorescence along dTomato-labeled CA1 apical and basal dendrites in locations where mCerulean-labeled CA3 axons and dTomato-labeled CA1 dendrites intersect (Figure 3). Fluorescence signals of reconstituted mGRASP were clearly evident in both the apical and basal dendritic structures of a CA1 neuron, whereas no signals were evident along tuft dendrites in the stratum lacunosum-moleculare where axons from CA3 do not project (Figure 3b). High-magnification images showed strong mGRASP signals in the spine heads of both apical and basal dendrites where mCerulean-labeled axons intersected with red dendrites (Figure 3c).

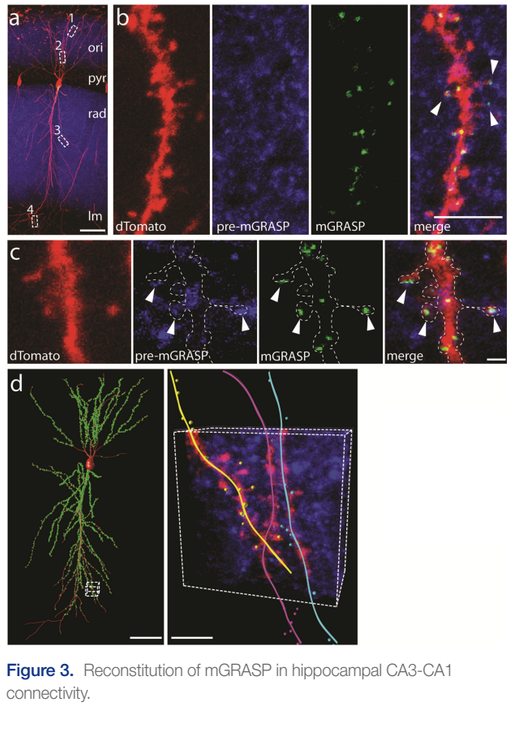

Figure 3. Reconstitution of mGRASP in hippocampal CA3-CA1 connectivity.

Furthermore, we tested mGRASP reconstitution in another long-range circuit, the thalamocortical circuit, connecting the ventral posterior medial nucleus of the thalamus with layer 4 (L4) neurons of the somatosensory cortex. Using rAAV viral injection, sequences encoding Cre recombinase–independent pre-mGRASP and Cre recombinase–dependent 'switch-on' post- mGRASP were transduced respectively into the thalamic ventral posterior medial nucleus and somatosensory cortex of Six3-Cre mice, expressing Cre recombinase mainly in layer-4 neurons [20]. Similar to results obtained with mGRASP in the hippocampus, we detected clear and strong reconstituted mGRASP puncta in sites where dTomato-labeled L4 neurons and mCerulean-labeled thalamic axons intersected (Figure 4).

To investigate the localization and distributions of synapses using mGRASP in dendritic compartments and in single cells, we developed analysis strategies and computational programs (Figure 5). Using our mGRASP detection program, the number and locations of synapses at the level of dendritic branches were automatically detected in three dimensions (Figure 3c) with ~93.5% accuracy, verified by comparison with annotation of randomly selected subvolumes (128 × 128 × 77 voxels) of neuTube-reconstructed neurons by multiple individuals (Online Methods, Supplementary Note 2 and Supplementary Software).

Validation of mGRASP

To test whether mGRASP can be used to detect synapses in the mouse brain without introducing artifacts, we first examined whether mGRASP induces changes in synaptic organization. We analyzed a region of massively reconstituted mGRASP signals with conventional electron microscopy to check the morphology and abundance of excitatory synapses identified by the ultrastructure of postsynaptic densities and presynaptic vesicles. We found no differences in the number of excitatory synapses between hippocampi infected with both pre- and post-mGRASP, non-infected hippocampi and hippocampi infected with only single mGRASP components. Notably, our method for gene delivery did not cause any alteration in the number of synapses, compared to nontransduced neurons.

To measure whether mGRASP detects actual synapses rather than neurite touches, we analyzed cell populations known to be synaptically connected as well as ones known not to be synaptically connected (that is, CA1 pyramidal neurons–oriens-lacunosum moleculare (OLM) interneurons as a synaptic pair, and CA3 pyramidal neurons–OLM interneurons as a nonsynaptic pair) [21, 22]. This test is powerful because axons of both CA3 and CA1 neurons intersect with dendrites of OLM cells, but mGRASP should detect only actual synaptic contacts from CA1 axonal projections and not from CA3 neurons. To express post-mGRASP selectively in OLM cells, we used the Cre recombinase– dependent 'switch-on' post-mGRASP in a genetically manipulated mouse line expressing Cre recombinase under the control of the endogenous somatostatin promoter via knock-in (sst-Cre). To label a negative presynaptic partner of the OLM interneurons, we injected rAAV vectors expressing Cre recombinase–independent pre-mGRASP into CA3 neurons.

For a positive presynaptic partner of the OLM interneurons, we injected the Cre recombinase–dependent 'switch-off ' pre-mGRASP into CA1 neurons to

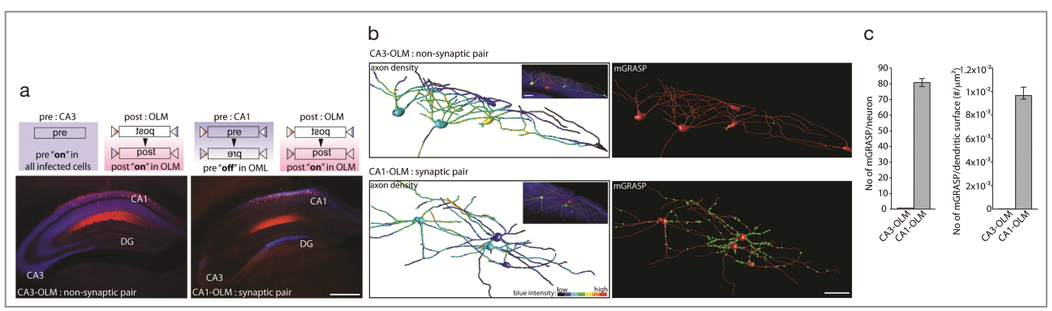

Figure 4. mGRASP detects actual synapses with high specificity.

avoid expressing both mGRASP components in the same cell, as described above, because they are spatially close to one another (Figure 1b and 4a). To measure connection probability, we quantified the availability of axons in the local environment surrounding OLM dendrites by measuring the average intensity of blue signal in the same expanded tubes of reconstructed OLM dendrites that we used for mGRASP detection (radius of the traced tube plus ~2.5 μm) (Figure 4b).

In the case of the negative synaptic CA3-OLM connections, we detected little or no reconstituted mGRASP puncta, although we saw many axon-dendrite intersections (Figure 4b, 4c). Of the few mGRASP puncta detected in CA3-OLM connections, over 78% occurred on somata and likely reflect innervations from other interneurons in CA1 neurons.

By contrast, we observed many reconstituted mGRASP puncta in CA1-OLM connections, especially on dendrites of OLM cells. Overall, we found clear results in mGRASP detection from negative and positive synaptic partners with the same postsynaptic populations: as predicted, we detected mGRASP signals exclusively in CA1-OLM connections and not in CA3-OLM connections. Additionally, using antibodies to GFP shown to have preferred specificity for reconstituted forms of GFP [12], we detected immuno-gold particles by electron microscopy in the synapses (Supplementary Figure 7). Together, these results indicate that with high specificity, mGRASP detected actual synapses rather than neurite touches and induced no obvious artifact effects on synaptic organization.

Thus mGRASP expression fulfills our criteria for specific labeling of actual synapses without inducing aberrant synapse formation.

Excitatory and inhibitory synapses with mGRASP

Our automated reconstruction and detection programs can detect synapses and distinguish them from the dendritic compartments of other nearby neurons (Figure 5). We then sought to develop an automated method to distinguish between excitatory and inhibitory synapses based on the size and shape of mGRASP signals. Taking advantage of reports that all synaptic inputs converging onto the perisomatic area of CA1 pyramidal neurons are inhibitory [23], we compared fluorescent mGRASP signals from somata and from dendrites of CA1 neurons. We observed that mGRASP fluorescent puncta on somata

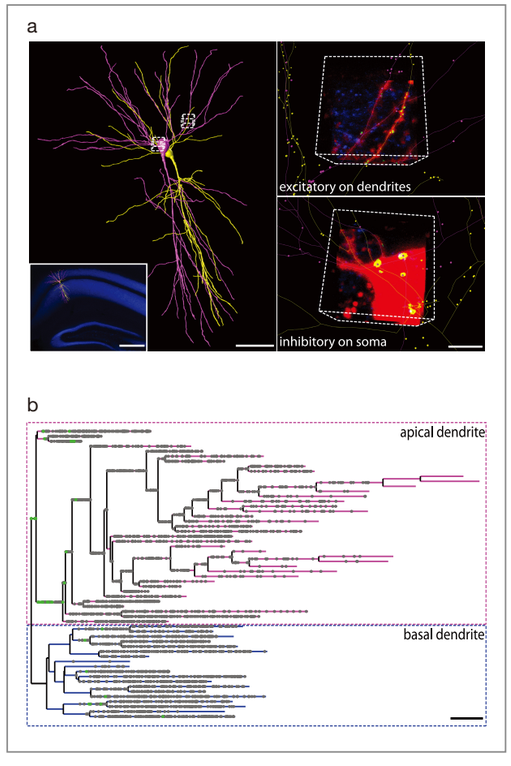

Figure 5. Distribution of excitatory and inhibitory synapses revealed by mGRASP.

were always large and elliptical, whereas those on dendrites were small and round (Figure 5), supporting a classification scheme. In addition, to confirm contralateral inhibitory synapses, as we used contralateral presynaptic projections in this study, we examined contralateral projections of CA3 interneurons using a genetically manipulated mouse line expressing Cre recombinase under the control of the endogenous glutamic acid decarboxylase promoter via knock-in (GAD-iCre). We observed contralateral projections of GAD interneurons in both oriens and radiatum of CA1 when we delivered Cre recombinase–dependent rAAV vector for the expression of dTomato specifically into GAD interneurons in CA3. This indicates that large and strong signals from reconstituted mGRASP puncta on the main trunk of the CA1 neuron were likely inhibitory inputs (Figure 3a). To investigate the locations and distributions of synapses in depth in dendritic compartments and in single cells, we constructed dendrograms with separate apical and basal dendrites of CA1 and plotted the locations of synapses on them as detected by mGRASP (Figure 5b). Detailed descriptions of the synaptic distributions on dendritic compartments will be critical for a full understanding of their contribution to synaptic signaling and dendritic integration.

Discussion

We presented our initial efforts to determine the location and distribution of synapses in the mouse brain using mGRASP. The method can allow rapid and precise characterization of synaptic connectivity in neuronal circuits in conditions of health as well as in models of neurological disorders that may be caused by abnormal synaptic connectivity, such as autism [24].

In recent years, new optogenetic approaches (for example, based on channelrhodopsin expression) have accelerated the light microscopy–based analysis of synaptic connectivity and synaptic strength [25, 26], yet these techniques operate at relatively low levels of resolution and can yield ambiguous results.

More recent studies have approached 'functional connectomics' by combining light microscopy–based calcium imaging with electron microscopy–based connectivity mapping in locations such as the mammalian retina and visual cortex [3, 27]. However, only relatively small brain volumes, and in particular thin vertical ranges (~50–60 μm), can presently be imaged, mainly because electron microscopy image acquisition and analysis remains a formidable challenge. Alternatively, Brainbow, a light microscopy–based technique integrating genetic manipulation of neurons, can allow synapses to be inferred from neurite contacts by coloring individual neuronal processes differently. This technique, however, appears to be effective for only a subset of synaptic connections [9]. Another light microscopy–compatible method relies on the anterograde and retrograde trans-synaptic tracing of neuronal circuits, but, to date, toxicity issues and biased cell-type specificity of trans-synaptic tracers have limited the utility of the technique [10]. Finally, array tomography, a combination of light microscopy– and electron microscopy–based approaches used to resolve proteomic details at synapses by immunolabeling of multiple synaptic markers, relies entirely on the efficiency of antibody staining and preserved tissue antigenicity, and can result in potentially ambiguous and incomplete results [28]. Our optimized mGRASP system, combined with computer-based three-dimensional (3D) reconstruction of neurons, will complement electron microscopy and optogenetic efforts toward an integrated 3D brain atlas, and can greatly accelerate comprehensive studies of synaptic long-range circuits and microcircuits.

By rapidly revealing the patterns of synaptic connectivity, this approach will enable future studies, but additional challenges and promises remain. To investigate synaptic connectivity in different brain areas, the mGRASP system may need specialized optimizations for different

types of synapses. As outlined here, these optimizations could include tailored computational analysis routines and additional versions of mGRASP components with different transmembrane carriers to provide a range of proximities between synaptic membranes. When possible, care should be taken to apply the appropriate validation methods described above to any additional brain regions under study. Furthermore, it will be essential to expand the genetic toolbox for targeting dense or sparse gene expression in desired cell types in different brain areas. Additional promoters for individual cell types, new combinations of multiple genetic switches, different viral systems and creative combinations of all the above with well-characterized transgenic lines (for example, GENSAT) will expand the range of possible experiments. Also, split fluorescent proteins of different colors or photoactivable versions of these proteins will allow the reconstruction of multiply innervated networks with overlapping connectivity patterns. In addition, activity-dependent mGRASP systems can allow the determination of how certain circuits relate to specific behavioral tasks. Thus, additional purpose-driven optimization of mGRASP can provide information about synaptic variation, development and abnormality in intricate networks.

Note

This article and images are cited from “mGRASP enables mapping mammalian synaptic connectivity with light microscopy” in *Nature Methods*, Vol. 9 (1), pp. 96-102.

References

[1] Neher E, Sakmann B. *Nature* 1976; 260: 799–802.
[2] Buzsaki G. *Nat. Neurosci.* 2004; 7: 446–451.
[3] Bock DD et al. *Nature* 2011; 471: 177–182.
[4] Sotelo C. *Nat. Rev. Neurosci.* 2003; 4: 71–77.
[5] Mishchenko Y et al. *Neuron* 2010; 67: 1009–1020.
[6] Denk W, Horstmann H. *PLoS Biol.* 2004; 2: e329.
[7] Knott G, Marchman H, Wall D, Lich B. *J. Neurosci.* 2008; 28: 2959–2964.
[8] Micheva KD, Smith SJ. *Neuron* 2007; 55: 25–36.
[9] Livet J et al. *Nature* 2007; 450: 56–62.
[10] Wickersham IR et al. *Neuron* 2007; 53: 639–647.
[11] Feinberg EH et al. *Neuron* 2008; 57: 353–363.
[12] Gordon MD, Scott K. *Neuron* 2009; 61: 373–384.
[13] Zhai RG, Bellen HJ. *Physiology* 2004; 19: 262–270.
[14] Fairless R et al. *J. Neurosci.* 2008; 28: 12969–12981.
[15] Dean C, Dresbach T. *Trends Neurosci.* 2006; 29: 21–29.
[16] Zhang C et al. *Neuron* 2010; 66: 403–416.
[17] Tang W et al. J. *Neurosci.* 2009; 29: 8621–8629.
[18] Navarro-Quiroga I, Chittajallu R, Gallo V, Haydar TF. *J. Neurosci.* 2007; 27: 5007–5011.
[19] Shimshek DR et al. *Genesis* 2002; 32: 19–26.
[20] Liao GY, Xu B. *Genesis* 2008; 46: 289–293.
[21] Lacaille JC, Mueller AL, Kunkel DD, Schwartz kroin PA. J. *Neurosci.* 1987; 7: 1979–1993.
[22] Klausberger T, Somogyi P. *Science* 2008; 321: 53–57.
[23] Megías M, Emri Z, Freund TF, Gulyás AI. *Neuroscience* 2001; 102: 527–540.
[24] Belmonte MK et al. *J. Neurosci.* 2004; 24: 9228– 9231.
[25] Petreanu L, Huber D, Sobczyk A, Svoboda K. *Nat. Neurosci.* 2007; 10: 663–668.
[26] Wang H et al. *Proc. Natl. Acad. Sci. USA 2007*; 104: 8143–8148.
[27] Briggman KL, Helmstaedter M, Denk W. *Nature* 2011; 471: 183–188.
[28] Micheva KD, Busse B, Weiler NC, O’Rourke N, Smith SJ. *Neuron* 2010; 68: 639–653.

[**Feature Articles**]

Bidirectional Modulation of Fear Extinction by Mediodorsal Thalamic Firing in Mice

Sukchan Lee
Center for Neuroscience
echany@kist.re.kr

Introduction

A conditioned fear response can be extinguished by repeated exposure to a neutral conditioned stimulus (CS) in the absence of a noxious unconditioned stimulus (US). This process, termed fear extinction, is the basis of the general therapeutic process used to treat human fear disorders. Although the role that both the cortical and subcortical limbic systems play in this process has received considerable attention, the neural mechanism of fear extinction is not yet fully understood. The mediodorsal thalamic nucleus (MD), a part of the basolateral limbic system, has strong interconnections with the medial prefrontal cortex (mPFC) as well as with the amygdala, and these regions together form a tight triangular circuitry [1-3]. The two brain regions connected to the MD are known to be key in the formation and extinction of conditioned fear memory [4,5].

In humans, damage to the MD may lead to complex disorders of PFC-dependent cognitive functions, including learning deficits, memory loss, attention problems, or emotional changes [6,7]. In previous lesion studies performed in animals, the MD, when functioning, appeared to be linked to the PFC or the amygdala to facilitate associative learning [8-10]. Anatomical and lesion studies have suggested that activation of the MD in the cortico-thalamo-cortical loop is required if attention is to be devoted to a particular task as well as for encoding new information into memory [1,2,11].

Therefore, the MD is thought to function as a bridge in the limbic circuits of the learning and memory processes. Nevertheless, the contribution of the MD to fear conditioning and extinction remains controversial.

In response to input signals, thalamocortical neurons demonstrate dual firing patterns determined by membrane status: a burst of high-frequency action potentials upon hyperpolarization, or tonic firing of singular action potentials when depolarization occurs [12,13]. Hyperpolarized membrane potentials lead to activation of T-type Ca^{2+} channels, yielding low voltage–activated T–type Ca^{2+} currents (LVCCs) which in turn trigger burst firing. Glutamatergic corticothalamic inputs activate metabotropic glutamate receptor type 1 (mGluR1), and thus induce membrane depolarization in thalamocortical neurons, leading to a shift in thalamic firing from the burst to the tonic mode [14]. In the corticothalamic postsynapses, mGluR1 is physiologically coupled to phospholipase C-β4 (PLCβ4), and both proteins are abundantly expressed in dorsal thalamic nuclei, including the MD. Inactivation of mGluR1-PLCβ4 in mice leads to enhanced burst firing of the ventrobasal thalamus and decreased pain responses, presumably because of failure in the relay of persistent pain signals to the cortex. In addition, inactivation of PLCβ4 in the ventrobasal thalamus causes development of spontaneous absence epilepsy, accompanied by increased thalamic burst firing. Changes in thalamic firing patterns have also been implicated in sleep and arousal, sensory signaling, and control of consciousness. However, little is known about the physiological functions of thalamic firing modes with respect to other aspects of cognitive or emotional processing.

In our research at KIST, we examined the possible role of the MD and its firing modes in the fear extinction process, employing mice in which the mGluR1-PLCβ4 signaling pathway was deleted. Using a combination of tools, including genetics, pharmacology, physiology, and microstimulation, we revealed that the MD, controlled by the mGluR1-PLCβ4 signaling pathway, can modulate fear extinction bidirectionally through its firing modes: tonic firing may facilitate fear extinction as in physiological conditions whereas burst firing may suppress the extinction as in a pathological condition.

Impaired fear extinction in *PLCβ4*$^{-/-}$ mice

Wild-type and *PLCβ4* knock-out (*PLCβ4*$^{-/-}$) mice were exposed to three trials of tone (CS), each of which was co-terminated with an electric foot shock (US). During conditioning, both groups of mice showed similar levels of freezing (Figure 1a). 24 or 48 h after conditioning, the freezing levels of the two groups remained similar (Figure 1b). Taken together, the results show that acquisition and expression of auditory-conditioned fear memory were similar in the two groups.

Next, newly fear-conditioned mice were exposed to repeated CS without US 24 h after conditioning (i.e., extinction learning). Wild-type mice showed progressively decreased levels of freezing (Figure 1c). In contrast, *PLCβ4*$^{-/-}$ animals maintained persistently high levels of freezing under the same conditions (Figure 1c). Next, 24 h after extinction learning was complete, mice were re-exposed to CS without US (i.e., extinction recall). Wild-type mice showed 54±7.9 % freezing. However, *PLCβ4*$^{-/-}$ animals showed no reduction in the freezing response compared with that seen during extinction learning (P = 0.32). The two groups also did not differ in responses to foot shocks of varying intensities (Figure 1d).

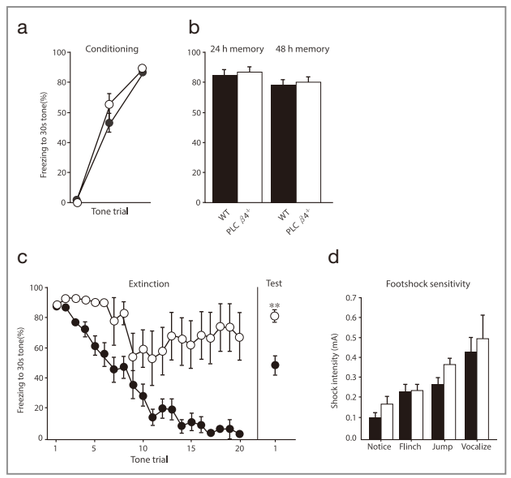

Figure 1. Defective extinction of auditory-conditioned fear memory in *PLCβ4*$^{-/-}$ mice.

Blocking the MD mGluR1-*PLCβ4* pathway inhibits extinction

PLC4 is abundantly expressed in the MD. To test whether the impaired extinction phenotype of *PLCβ4*$^{-/-}$ mice was attributable to a *PLCβ4* defect in the MD, either a lentivirus encoding a sequence active to knock down PLCβ4 (shPLCβ4), or a non-target lentivirus (control shRNA), was injected into the MD of wild-type mice (Figure 2a–l). Three weeks after injection, the two groups showed no difference in the level of freezing seen during conditioning.

However, during extinction learning, the shPLCβ4 group showed a significantly higher freezing level than did the control shRNA group (Figure 2m). Similar data were obtained when an extinction recall test was conducted (Figure 2m). These results indicate that the MD contributes to the impaired extinction phenotype of *PLCβ4*$^{-/-}$ mice. To quantify retrospectively the extent of gene silencing, we sacrificed the mice after completion of behavioral tests and used immunohistology to measure PLCβ4 expression in MD neurons. The proportion of PLCβ4-positive neurons in the MD was significantly reduced in shPLCβ4-injected animals compared to control mice, indicating that the lentivirus expressing shPLCβ4 significantly reduced PLCβ 4 expression in MD neurons.

In the thalamus, PLCβ4 forms a signaling complex with mGluR1, which is expressed mainly in corticothalamic postsynapses. If mGluR1 were coupled to PLC4 during the process of fear extinction, we hypothesized that inhibition of mGluR1 in the MD would affect fear extinction in a manner similar to that of the *PLCβ4*$^{-/-}$ mutation. To test this possibility, we injected CPCCOEt, a selective mGluR1 antagonist, into the MD of wild-type mice. Wild-type animals in which cannulae had been implanted into the MD were fear-conditioned, and 24 h later, were injected with CPCCOEt or vehicle. 30 min after injection, mice were assessed in terms of fear extinction learning. As shown in Figure 2n, CPCCOEt–injected animals were significantly impaired in terms of fear extinction, maintaining higher freezing levels across all CS trials compared to vehicle-injected mice. In extinction recall tests performed the next day, the CPCCOEt-injected group showed significantly higher freezing levels than did vehicle-treated animals. These data show that an active

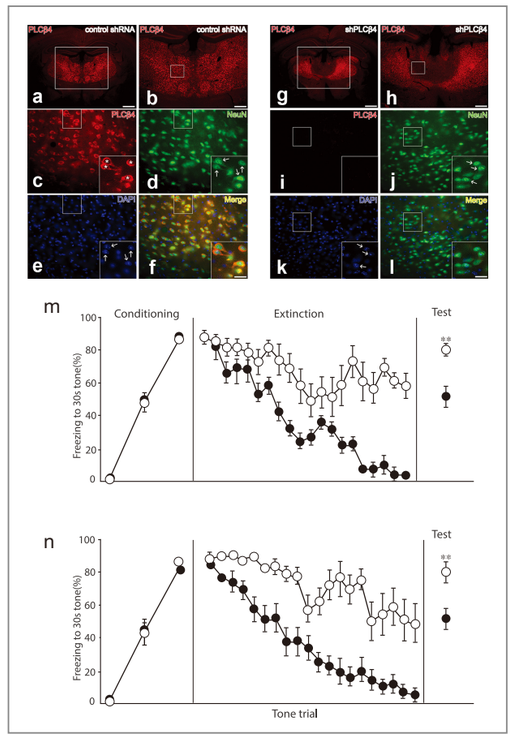

Figure 2. Blockade of the mediodorsal thalamic mGluR1-*PLCβ4* pathway inhibits fear extinction.

MD mGluR-PLCβ4 signaling pathway is required if fear extinction is to occur efficiently.

Stronger bursts with increased LVCCs in MD neurons

In an effort to discover the cellular mechanisms of impaired fear extinction in *PLCβ4*$^{-/-}$ mice, we examined the intrinsic firing properties of MD neurons in brain slices using patch-clamp recording techniques. The number of spikes in a burst was positively correlated in both wild-type and mutant animals, with the magnitude of voltage change created by the hyperpolarizing current (Figure 3a). Notably, however, *PLCβ4*$^{-/-}$ MD neurons showed a significantly increased number of spikes within a burst; the bursts were thus stronger than those in wild-type animals (Figure 3c). Unlike what was seen upon burst firing, no significant difference was observed in tonic firing patterns between the wild-type and *PLCβ4*$^{-/-}$ MD neurons (Figure 3b, d). Low-threshold burst spikes are mediated by T-type Ca^{2+} currents triggered by the hyperpolarization-activated cation currents, I_h. *PLCβ4*$^{-/-}$ MD neurons showed a significant increase in I_h currents. To understand further the ionic mechanism responsible for the altered firing patterns of *PLCβ4*$^{-/-}$ MD neurons, we measured LVCCs, and high voltage-activated Ca^{2+} currents (HVCCs), in MD neurons acutely dissociated from wild-type or *PLCβ4*$^{-/-}$ mice (Figure 3e). In terms of total calcium current density, *PLCβ4*$^{-/-}$ neurons showed a significantly increased LVCC but a normal HVCC compared with wild-type neurons (Figure 3f). Upon normalized stepwise current activation, *PLCβ4*$^{-/-}$ neurons also demonstrated a significant rise in LVCC (Figure 3g), but the HVCC did not differ from that of wild-type animals (Figure 3h). These results suggest that increases in Ih and LVCC likely explain the rise in T-type channel-mediated burst firing in *PLCβ4*$^{-/-}$ MD neurons.

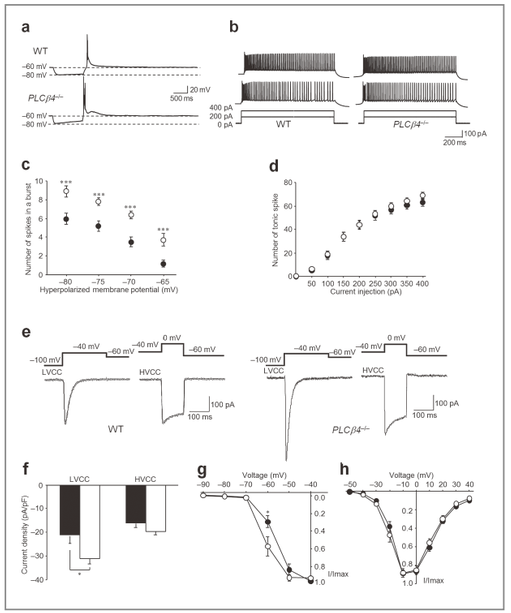

Figure 3. Stronger low-threshold burst firing and enhanced low-voltage-activated Ca^{2+} current in MD neurons of PLCβ4$^{-/-}$ MD mice.

Inhibitory role of T-type Ca^{2+} channels in extinction

The above observations on T-type Ca^{2+} channel-mediated cell properties caused us to hypothesize that a reduction of T-type current in the *PLCβ4*$^{-/-}$ MD might rescue the phenotype of impaired fear extinction. We tested this hypothesis by blocking T-type Ca^{2+} channel activities in the MD prior to evaluation of fear extinction. The MD of conditioned *PLCβ4*$^{-/-}$ mice was injected with a general T-type Ca^{2+} channel inhibitor, mibefradil, 1 h before fear extinction learning (Figure 4a). As CS was repeatedly delivered, mibefradil-injected *PLCβ4*$^{-/-}$ mice showed gradually reduced freezing levels, whereas vehicle-injected *PLCβ4*$^{-/-}$ mice continued to show higher freezing levels than did the mibefradil-treated group. The next day, when the extinction recall test was performed, the mibefradil-treated group showed significantly lower freezing levels than did the vehicle group, indicating that mibefradil rescued the impaired extinction phenotype of *PLCβ4*$^{-/-}$ mice. More importantly, a similar mibefradil treatment facilitated the extinction process in wild-type mice. As reflected in Figure 4b, mibefradil-injected wild-type mice showed a significantly faster reduction of freezing behavior upon extinction learning than did vehicle-injected wild-type animals. The following day when the extinction recall test was run, the mibefradil group still exhibited somewhat reduced freezing behavior compared to the vehicle group.

To rule out the possibility that the extinction-promoting effects of mibefradil were attributable to the blocking of L-type Ca^{2+} channels, conditioned wild-type mice were injected with nifedipine, a specific L-type Ca^{2+} channel inhibitor that does not affect T-type channels. MD injections were given 1 h before extinction learning commenced. Nifedipine treatment had no significant effect on fear extinction (Figure 4c).

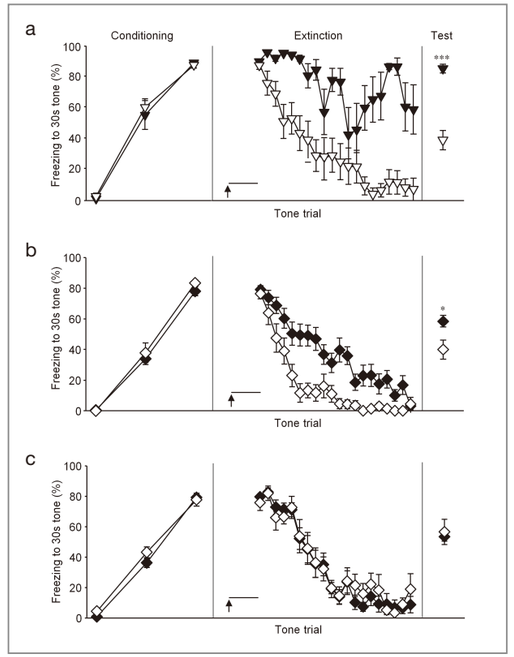

Figure 4. Accelerating effect of an intra-MD infusion of a T-type Ca^{2+} channel blocker on fear extinction learning, but not on consolidation of extinction.

Changes in thalamic firing patterns during extinction

To examine the firing properties of MD neurons during extinction learning, mice implanted with chronic unit-recoding electrodes in the MD were conditioned, and 24 h later, were assessed in extinction learning. 19 neurons from 15 wild-type mice and seven neurons from seven *PLCβ4*$^{-/-}$ mice were recorded in the MD (Figure 5a). Single unit activities were examined to distinguish tonic firing from low-threshold burst firing (Figure 5b).

The baseline frequency of tonic firing was similar in the wild-type and *PLCβ4*$^{-/-}$ MDs. However, when exposed to the extinction tone, a significant difference was noted between the two groups (Figure 5c). Whereas wild-type neurons showed a significant increase in tonic firing over the baseline, *PLCβ4*$^{-/-}$ neurons showed no change. When tonic firings from all neurons, including the mutant and wild-type, were analyzed against the degree of extinction learning, the amount of increase in tonic firing during the extinction learning was positively correlated with the extinction level measured in the extinction recall test done 24 hr later. The greater the increase in tonic firing during extinction learning, the more efficient was the extinction, as evidenced by less freezing in the extinction recall test.

During the baseline period before extinction tone, 14 out of 19 wild-type neurons showed burst firing, whereas all seven of the mutant-type neurons showed burst firing. Interestingly, the baseline frequencies of the spikes associated with burst events were significantly higher in *PLCβ4*$^{-/-}$ neurons than in wild-type neurons, a finding relevant to those in the slice experiments described above (Figure 3). In response to extinction tones (Figure 5e), a significant increase in burst firing over the baseline was evident in the mutant whereas no such increase was shown in the wild-type. As a result, the frequency of burst firing during the extinction was dramatically higher in *PLCβ4*$^{-/-}$ neurons than in wild-type neurons (Figure 5e). In other words, the mutant MD neurons showed enhanced burst firing both at the baseline and in extinction.

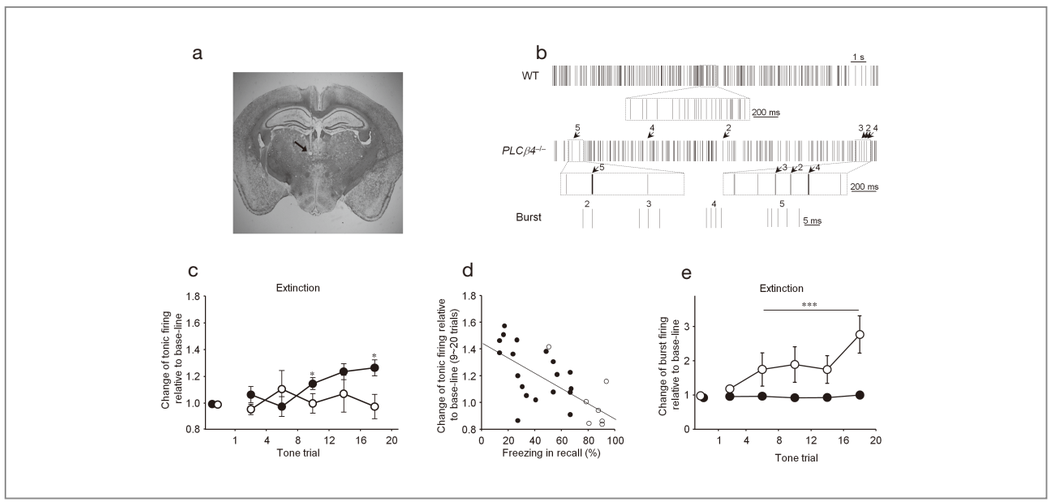

Figure 5. Changes in CS-evoked burst and tonic firing patterns of MD neurons in wild-type and PLCβ4$^{-/-}$ mice during extinction learning.

Opposite effects of the two firing modes on extinction

The positive correlation between increased tonic firing of MD neurons and fear extinction encouraged us to hypothesize that the positive change in tonic firing of the MD might be physiologically linked to the learning process of fear extinction. To explore such a possibility, the MDs of fear-conditioned wild-type and *PLCβ4*$^{-/-}$ mice were electrically stimulated to increase tonic firing during fear extinction learning. To this end, 100-ms trains of low-density (100 Hz) current mimicking tonic spikes were delivered within the MD at 1 sec or 3 sec intervals during the 30 seconds of continuous tone (paired-stimulated mice). We confirmed that, in brain slices, such train stimulation induced 100-Hz-tonic spikes in adjacent MD neurons (Figure 5a).

As shown in Figure 5b, paired-stimulated *PLCβ4*$^{-/-}$ mice showed a more rapid decrease in freezing level than did the two control *PLCβ4*$^{-/-}$ animals throughout the whole period of extinction challenge. Interestingly, a dose-dependent fall in freezing levels was observed in the paired-stimulated group, whereas unpaired-stimulated *PLCβ4*$^{-/-}$ mice did not show any difference in freezing level compared to non-stimulated *PLCβ4*$^{-/-}$ animals. In the extinction recall test performed on the following day, paired-stimulated *PLCβ4*$^{-/-}$ mice still showed significantly reduced freezing compared to that in the two control groups. In addition, we observed that tonic-evoking stimulation MD neurons facilitated extinction in wild-type animals (Figure 5c). These results suggest that an increase of tonic firing in the MD is necessary for acquisition of fear extinction.

To explore a possible causal relationship between an enhanced T-type-dependent burst firing and extinction failure in *PLCβ4*$^{-/-}$ mice, MDs of fear-conditioned wild-type mice were electrically stimulated with a protocol mimicking burst spikes during extinction learning (Figure 5a). As shown in Figure 5c, wild-type mice stimulated by burst-evoking trains paired with tones showed a significantly slower reduction of freezing levels compared to that of control groups in the extinction learning phase.

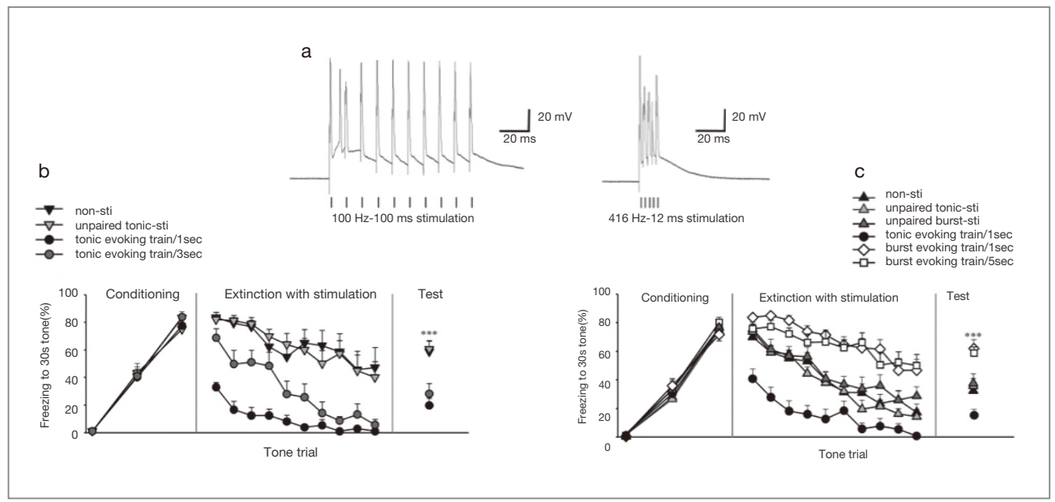

Figure 6. Opposite effects of MD-electric stimulation, mimicking dual firing, on fear extinction learning.

In addition, extinction recall tests showed a lower reduction in freezing level in the former group than in the other groups.

Conclusion

As described in this article, we have presented evidence that the MD is critically involved in the modulation of fear extinction. Our experiments involved the use of genetics (a null mutation as well as a localized gene knockdown), pharmacology, electrophysiological recording, and microstimulation. We found that the tonic firing in MD neurons critically contributes to extinction learning as shown in normal and pathological conditions, whereas increased burst firing has a suppressive effect on extinction as shown in the mutation.

Our data offer a new insight into the neural mechanism of fear extinction and may help development of improved treatments for anxiety disorders. In this respect, it is notable that some patients with post-traumatic stress disorder (PTSD), a generalized anxiety disorder, show abnormal changes in thalamic activities when the traumatic memory is recalled. Medications controlling the excitability of the MD might help in the treatment of such disorders.

Note

This article and images are cited from “Bidirectional modulation of fear extinction by mediodorsal thalamic firing in mice” in *Nature Neuroscience*, Vol. 15 (2), pp. 308-314.

References

[1] Ray JP, Price JL. *J Comp Neurol.* 1992; 323: 167- 97.

[2] Ray JP, Price JL. *J Comp Neurol.* 1993; 337: 1-31.

[3] Jones EG. *The Thalamus (Cambridge University Press, Cambridge; New York*, 2007).

[4] Fanselow MS, Poulos AM. *Annu Rev Psychol.* 2005; 56: 207-34.

[5] Pare D, Quirk GJ, Ledoux JE. *J Neurophysiol.* 2004; 92: 1-9.

[6] Van der Werf YD, Witter MP, Uylings HB, Jolles J. *Neuropsychologia* 2000; 38: 613-27.

[7] Zoppelt D, Koch B, Schwarz M, Daum I. *Neuropsychologia* 2003; 41: 1160-70.

[8] Mitchell AS, Dalrymple-Alford JC. *Eur J Neurosci.* 2005; 22: 973-85.

[9] Mitchell AS, Gaffan D. *J Neurosci.* 2008; 28: 258-63.

[10] Hunt PR, Aggleton JP. *J Neurosci.* 1998; 18: 10045-52.

[11] Winocur G. *Behav Brain Res.* 1990; 38: 145-54.

[12] Llinas R, Jahnsen H. *Nature* 1982; 297: 406-8.

[13] Sherman SM. *Trends Neurosci.* 2001; 24: 122-6.

[14] McCormick DA, von Krosigk M. *Proc Natl Acad Sci U S A.* 1992; 89: 2774-8.

[**Feature Articles**]

Using Polyplex Hydrogel as a siRNA Delivery System

Young-min Kim

Center for Bionics

g07505@kist.re.kr

Introduction

Chemical-based drugs have generally been used for the treatment of many diseases; however, these drugs can have adverse effects on patients due to their lack of selectivity and sometimes unexpected consequences in the body. In an effort to search for alternatives, gene therapy has emerged as a promising solution, particularly therapy involving small interference RNAs (siRNAs) which have no inheritance potential and can selectively inhibit target proteins [1].

Despite this enormous therapeutic potential, the lack of an efficient system that can deliver siRNAs over an extended period has restricted the effectiveness of siRNA therapy [2]. The development of a siRNA delivery system has focused on nano-sized carriers via systemic delivery. Polyplex, which is a nano-complex of polycations and genes, is a representative example. It can be easily prepared by the simple mixing of polycations and siRNAs, protecting the loaded genes from enzymes and proteins, and facilitating intracellular cellular uptake [3].

However, siRNAs have a very short retention time because of their easy dispersion properties, thereby resulting in low therapeutic efficacy in target tissues. Moreover, because they are mainly administered systemically, they can also induce non-specific transfection or systemic immune responses [4-5]. A local delivery carrier that can intensively transmit high concentrations of siRNA to a target site for a sufficient period can overcome these drawbacks. Among such carriers, injectable hydrogel with a stimuli-dependent sol-

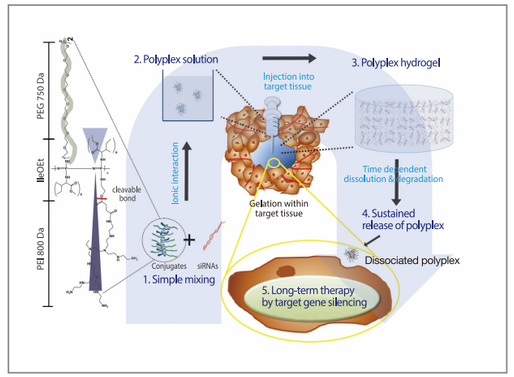

Scheme 1. A schematic concept of injectable polyplex hydrogel for localized and long-term delivery of siRNA. The polyplexes are induced by ionic interactions between L-PEI conjugates and siRNAs, and their aqueous solution transformed to gel by injection into target tissue. The polyplexes which have high gene silencing efficiency are released by time-dependent dissolution and degradation of polyplex hydrogel at the target tissue, thus enabling long-term therapy by siRNA based therapy, called RNA interference (RNAi).

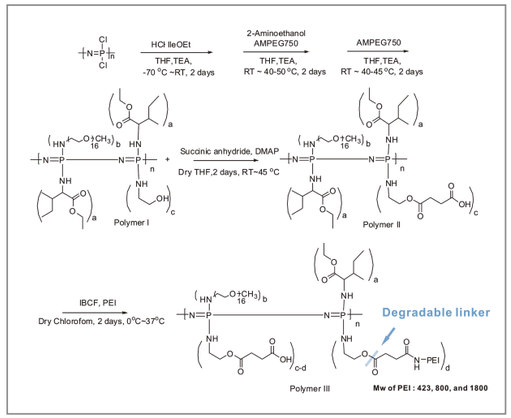

Scheme 2. The synthesis scheme of L-PEI-poly (organ-ophosphazene) conjugate.

gel transition has several advantages including minimal invasiveness, localization possibilities, and sustained release of the loaded drug [6].

To maintain these advantages while overcoming the drawbacks of polyplexes and injectable hydrogel, we have conducted research in injectable and localizable polyplex hydrogel. Polyplex hydrogel is a complex of siRNA and a cationic polymer exhibiting temperature-dependent sol-gel transitions *via* hydrophobic interaction, and it releases nano-sized polyplexes with high gene silencing efficiency for an extended period by introducing the moiety to hold and deliver the siRNAs due to complexation with siRNAs.

Synthesis of L-PEI-poly(organ-ophosphazene) conjugate

To conduct our studies, we first synthesized poly(organophosphazene), which was substituted with hydrophobic L-isoleucine ethyl ester (IleOEt) and hydrophilic α-amino-ω-metoxy-poly(ethylene glycol) (AMPEG), to enable thermosensitive gelation by hydrophobic interaction.

In brief, sol-gel phase-transition behavior may be explained by the phenomenon whereby hydrophilic parts show a lower critical solution temperature (LCST) of the polymer. Water molecules induce hydrogen-bonding in water at low temperatures, but as temperature increases, hydrogen bonding weakens and water molecules are released from the polymer by the increased hydrophobic interaction between molecules. Finally, hydrophobic chains associate with each other resulting in a network structure and the interaction is balanced with hydrophilic swelling/dissolution [7]. 2-Aminoethanol (AEtOH) was also substituted along with IleOEt and AMPEG to provide a hydroxyl group (polymer I). Then we esterified the hydroxyl group of AEtOH to provide a hydrolysable ester linkage and a terminal carboxylic acid group to conjugate the PEI. Finally, L-PEI was conjugated to the newly generated carboxylic acid group of poly(organophosphazene) (polymer II) through an amide bond (Scheme 2).

Preparation and characterization of polyplex between conjugate-4 and siRNA

We confirmed the complex formation ability of conjugate-4 with siRNAs. The polycation was expected to form an ionic complex with siRNA to protect siRNA and facilitate intracellular uptake. The formation of a polyplex using conjugate-4 and siRNA was confirmed with gel retardation assay; a complete polyplex without free siRNA was formed from N/P = 20. N/P value is the ratio of moles of the amine groups of cationic polymers / the phosphate groups of RNA (Figure 1a).

Particles with a size less than 200 nm and a slightly positive charge are favorable for effective cellular uptake [8]. We used a zetasizer with various N/P ratios to form polyplexes and then measured particle sizes and surface charges (Figures 1b and c).

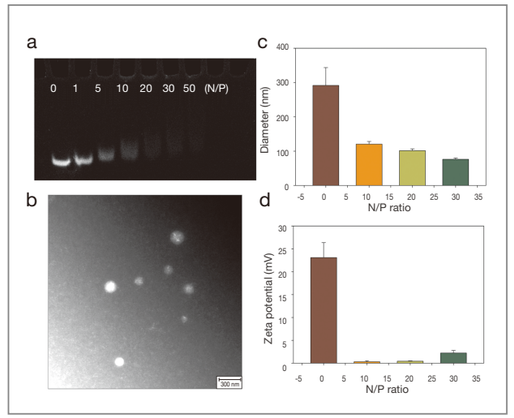

Figure 1. (a) Gel retardation assay of conjugate-4/GFP siRNA polyplexes as a function of N/P ratios. (b) TEM image of conjugate-4/VEGF siRNA polyplexes at N/P=30. (c,d) Sizes and ζ-potentials of conjugate-4/GFP siRNA polyplexes.

Gene silencing efficiency and stability test of polyplexes *in vitro*

The gene delivery efficiency of the polyplex we were testing was measured by down-regulating vascular endothelial growth factor (VEGF) using VEGF siRNA for quantification of gene silencing by an elisa kit.

The conjugate-4/VEGF siRNA polyplex exhibited a more significantly reduced VEGF level than the groups with cells only, VEGF siRNA only, or L-PEI only, except lipofectamine. The inhibition of VEGF expression was directly proportional to the amount of VEGF siRNA used in the polyplex group. When the amount of siRNA used was increased four times, the percentage of downregulated VEGF increased from 31% to 59% (Figure 2a).

We assumed that relatively high concentrations of polyplexes localized within a region could overcome the problem of low gene silencing efficiency and protection of the loaded siRNA from the extracellular environment before its uptake into the target cell would be provided by complexation. The conjugate-4/VEGF siRNA polyplexes showed enhanced siRNA stability in the presence of serum.

In contrast to naked siRNAs, which showed degradation after 1 hr, the polyplex-protected siRNA showed no severe degradation for 30 days (Figure 2b). These results indicate that the conjugate-4/siRNA polyplex can be used in gene therapy to improve siRNA stability and high gene silencing efficiency.

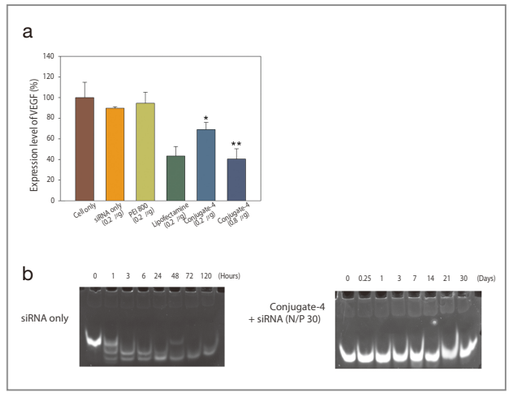

Figure 2. (a) *In vitro* VEGF gene silencing efficiency of conjugate-4/VEGF siRNA polyplex at N/P=30 in PC-3 cells. Numbers in brackets refer to the amounts of siRNA used. The asterisks indicate significant differences compared with the cell only group (Student's t-test). *P < 0.08 and **P < 0.001 *versus cell* only. (b) *In vitro* stability of conjugate-4/VEGF siRNA polyplex at N/P=30 after incubation in 20% fetal bovine serum for predetermined times.

Sustained polyplexes from polplex hydrogel and their gene silencing ability *in vitro*

The aqueous solution of conjugate-4 still showed a temperature-dependent sol-gel phase transition after being mixed with the siRNA and polyplex solution. While the polyplex solution (12.7 wt%) showed a flowing sol state inner circle at 20°C, it turned into a gel state at body temperature (Figure 3a).

In a release test however, polyplex hydrogel showed sustained release of siRNAs compared with the rapid elimination of siRNA by itself (Figure 3b). TEM images indicated that polyplexes released from hydrogel maintained the 50-100 nm sized diameter of spherical nanoparticles at day 21 after incubation (Figure 3c).

In addition, the polyplexes released from hydrogel at 21 days after incubation showed a reduced level of cyclin B1 compared to β-actin protein, as estimated by western blot analysis (Figure 3d). These data suggest that conjugate-4 can be used to prepare an injectable polyplex hydrogel with siRNA and can sustain the release of nano-sized polyplexes from hydrogel while demonstrating gene silencing efficiency at day 21.

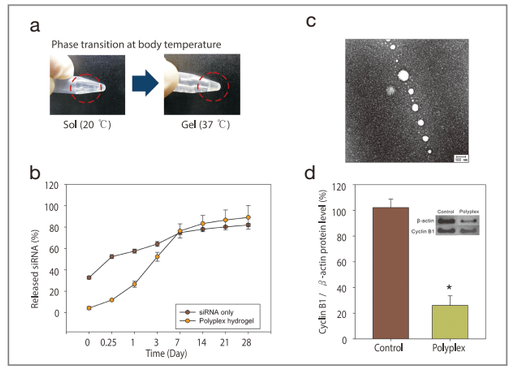

Figure 3. (a) Temperature-dependent sol-gel transition behavior of a polyplex solution composed of siRNA and conjugate-4 at 12.7 wt%. (b) Release of dissociated nano-sized polyplex from a polyplex hydrogel of 12.7 wt% with cy5.5-tagged siRNA. (c) TEM image of dissociated nano-sized polyplex from a polyplex hydrogel of 12.7 wt% after 21 days of incubation at 37°C. (d) Western blot analysis for checking cyclin B1 protein level in a PC-3 cell line reduced by polyplexes which were released from a polyplex hydrogel of 12.7 wt% after 21 days of incubation at 37°C. The expressed cyclin B1 and β-actin expressions were quantified by Image J *P <0.001 versus a control group.

Long-term gene silencing effect in an *in vivo* xenograft model

Prior to the siRNA-mediated anti-tumor activity test of the polyplex hydrogel to confirm its long-term gene silencing effect, we examined the intra-tumoral retention time of siRNA in polyplex hydrogel using cy5. 5-tagged siRNA in tumor-bearing mice and compared it to that of siRNA used alone.

In contrast to the siRNA-only group, the conjugate-4/siRNA group held fluorescence for 7 days and a fairly high intensity was maintained for 21 days at the tumor site (Figure 4a), suggesting that the polyplex protected siRNA from the *in vivo* environment for more than 3 weeks.

We next examined *in vivo* siRNA-mediated anti-tumor activity of the polyplex hydrogel for 30 days to confirm the effect of long-term siRNA retention. The polyplex hydrogels were prepared using cyclin B1 siRNA. Cyclin B1 is a critical mitotic regulator protein; therefore, inhibiting its expression induces cell cycle arrest at the G2 phase and apoptosis by programmed cell death [9].

All of the tumor-bearing mice were administered a single intra-tumoral injection; however, only the group treated with conjugate-4/cyclinB1 siRNA polyplex showed remarkably inhibited tumor growth.

The tumor sites of this group almost disappeared after 24 days (Figure 4b). The selective reduction of the cyclin B1 protein level in the tumor tissues after 30 days demonstrated that the anti-tumor activity was mediated by reduced cyclin B1 *via* RNAi (Figure 4c).

These results indicate that the conjugate-4/siRNA polyplex hydrogel successfully inhibited tumor growth by means of RNAi. It respresents a useful long-term formulation since, with a single injection, the release of the polyplex was sustained over an extended period while

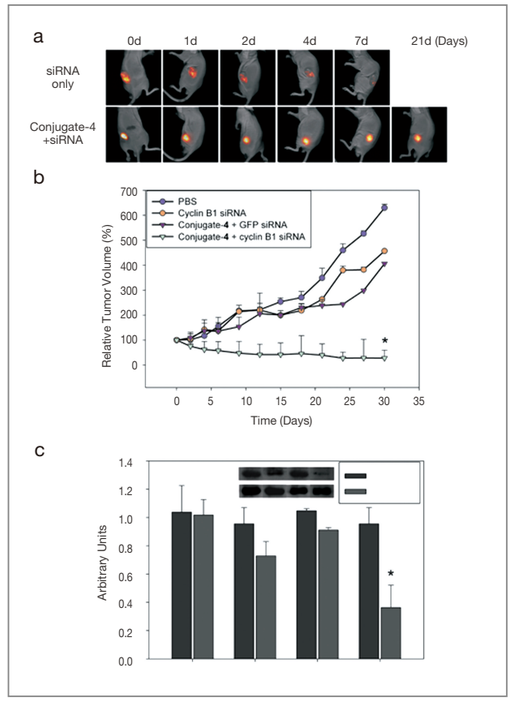

Figure 4. (a) *In vivo* siRNA retention of polyplex hydrogel of 12.7 wt% at N/P=30 using flourescent cy5.5-tagged cyclin B1 siRNA in PC-3 tumor xenografts. (b) Anti-tumor activity of conjugate-4/cyclin B1 siRNA polyplex hydrogel of 12.7 wt% at N/P=30 in PC-3 tumor xenografts. *P < 0.001 *versus* the group receiving PBS injection. (c) Western blot analysis for intra-tumoral cyclin B1 levels. The expressed cyclin B1 and β-actin expressions were quantified by Image J.*P < 0.001 *versus* cyclin B1 level of PBS injected group.

exhibiting a high gene silencing efficiency and low toxicity.

Conclusion

Using only one material, we developed an injectable, thermosensitive, and biodegradable polyplex hydrogel as a new concept for localized and long-term delivery of siRNAs. The administration of this polyplex hydrogel was simple and resulted in extremely low toxicity indicators. Furthermore, it achieved sustained release of the nano-sized polyplex within the target region while demonstrating high gene silencing efficiency over an extended period.

We expect that this new agent can serve as an alternative siRNA carrier for many diseases that require localized and long-term therapy, including tumors, bone fractures and even systemic diseases.

Note

This article and images are cited from: Kim, YM, Park, MR, Song, Sc. *ACS Nano* 2012; 6(7): 5757~5766.

References

[1] Bumcrot D, Manoharan M, Koteliansky V, Sah DWY. *Nat. Chem. Biol.* 2006; 2: 711-719.
[2] Liu Y, Huang L. *Mol. Ther.* 2010; 18: 669-670.
[3] Park MR, Kim HW, Hwang CS, Han KO, Choi YJ, Song SC, Cho MH, Cho, CS. *J. Gene Med.* 2008; 10: 198-207.
[4] Heyes J, Palmer L, Chan K, Giesbrecht C, Jeffs L, MacLachlan I. *Mol. Ther.* 2007; 15: 713-720.
[5] Sakurai H, Kawabata K, Sakurai F, Nakagawa S, Mizuguchi H. *Int. J. Pharmaceut.* 2008; 354: 9-15.
[6] Chun C, Lee SM, Kim SY, Yang HK, Song SC. *Biomaterials* 2009; 30: 2349-2360.
[7] Lee BH, Lee YM, Sohn YS, Song SC. *Macromolecules* 2002; 35: 3876-3879.
[8] Gratton SEA, Ropp PA, Pohlhaus PD, Luft JC, Madden VJ, Napier ME, DeSimone JMP. *Natl. Acad. Sci. USA.* 2008; 105: 11613-11618.
[9] Crombez L, Morris MC, Dufort S, Aldrian-Herrada G, Nguyen Q, McMaster G, Coll JL, Heitz F, Divita G. *Nucleic Acids Res.* 2009; 37: 4559-4569.

[Feature Articles]

Using a Fluorogenic Matrix Metalloproteinase 3–Specific Polymeric Probe for the Early Diagnosis of Arthritis in Mice with Collagen-Induced Arthritis

Inchan Youn
Center for Bionics
iyoun@kist.re.kr

Kwangmeyung Kim

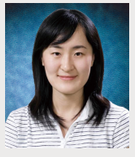

Juhee Ryu

Aeju Lee

Introduction

Rheumatoid arthritis (RA) is a systemic and chronic inflammatory disease that leads to the destruction, deformity, and functional loss of affected joints. Bone erosions develop in many patients with RA during the first two years of the disease; therefore, prompt treatment based on early diagnosis is desirable to halt progression of the disease and prevent irreversible disability. However, early diagnosis of RA can be difficult because there are often no typical radiographic changes or pathognomonic signs that can be observed during the initial stages of the disease. As a result, clinicians clearly need an accurate method for the early diagnosis of RA. The MMP-3 levels in serum and synovial fluid have been shown to correlate with RA disease activity and with markers of systemic inflammation such as the erythrocyte sedimentation rate (ESR) and the C-reactive protein (CRP) level. Therefore, elevated MMP-3 activity could potentially be used as a specific marker of joint inflammation and destruction in RA. In this study we used an NIRF optical imaging system to investigate whether an MMP-3–specific polymeric probe could also be used for early diagnosis in a mouse model of collagen-induced arthritis (CIA) and for visualization of arthritis progression.

Synthesis and characterization of the MMP-3 nanoprobe

The MMP-3–specific polymeric probe was developed by conjugating MMP-3–specific peptide probes, consisting of NIRF dye FPR-675, MMP substrate peptide, and dark quencher (BHQ-3), to self-assembled CNPs (Figure 1a). When the MMP-3–specific polymeric probe was treated with various concentrations of MMP-3 at 37°C for 60 minutes, the polymeric probe recovered fluorescence signals that increased in direct proportion to increasing MMP-3 concentrations (r^2=0.99) (Figure 1b). In particular, the polymeric probe recovered a substantial fluorescence signal with 1.9 nM MMP-3, indicating high sensitivity to active MMP-3. The enzyme selectivity of the polymeric probe was evaluated *in vitro* by incubating the polymeric probe with activated MMP-3 or MMP-7 at 37°C for 60 minutes. The MMP-3–specific polymeric probe recovered significantly different fluorescence signals for MMP-3 and MMP-7 (9.3-fold and 7.3-fold for MMP-3 and MMP-7, respectively) (Figure 1c). Meanwhile, the scrambled probe recovered little fluorescence intensity when treated with MMP-3 and MMP-7, indicating that the scrambled probe could be used as a control probe for detecting MMP-3 and MMP-7.

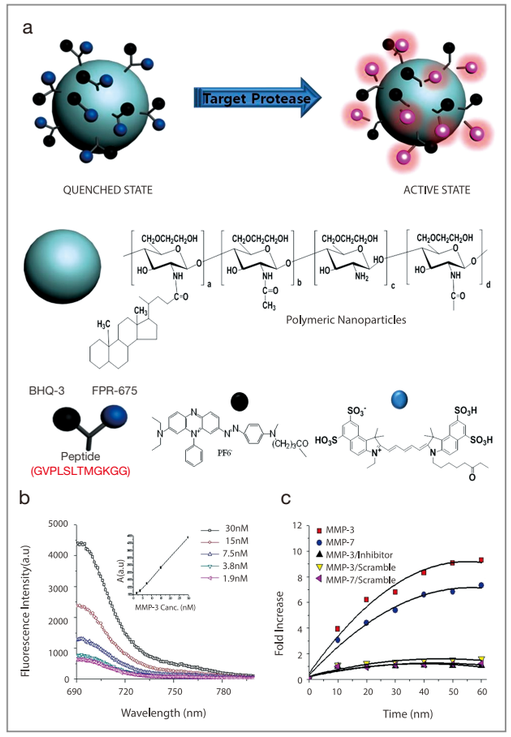

Figure 1. (a) Schematic diagram and chemical structures of the matrix metalloproteinase 3 (MMP-3)–specific polymeric probe. The MMP-3–specific polymeric probe was developed by conjugating MMP-3– specific peptide probes, consisting of near-infrared fluorescence (NIRF) dye (Flamma FPR-675), MMP substrate peptide, and dark quencher (Black Hole Quencher-3 [BHQ-3]) to self-assembled chitosan nanoparticles. When the MMP-3–specific polymeric probe contacts MMP-3, cleavage of the quenched probe due to specific substrate recognition by MMP causes significant recovery of NIRF signals. (b) Fluorescence intensity (FI) of the MMP-3–specific polymeric probe in the presence of various concentrations of MMP-3 following incubation for 60 minutes at 37°C. Inset., Standard curve of the MMP-3–specific polymeric probe. (c) Fluorescence intensity of MMP-3–specific polymeric probes and scrambled probes (20 nM) in the presence of various MMPs (MMP-3, MMP-7, and MMP-3 plus inhibitor) for 60 minutes at 37°C. incubation.

In Vivo monitoring of MMP-3 activity in CIA

To determine whether an MMP-3–specific polymeric probe could be used for the early diagnosis of RA and to monitor the progression of arthritis in mice with CIA, fluorescent images were observed at different stages of RA development, specifically 2, 3, 4, and 5 weeks after the first immunization. Optical images were obtained 1 hour after administering the probe intravenously to mice with CIA. Although a clearly detectable fluorescence signal was obtained from arthritic joints 15 minutes after the probe injection, the highest signal-to-background ratio was detected 1–2 hours after the probe injection, meaning that this was the best time for diagnosis (data not shown).

The NIRF signal from the arthritic joints increased over

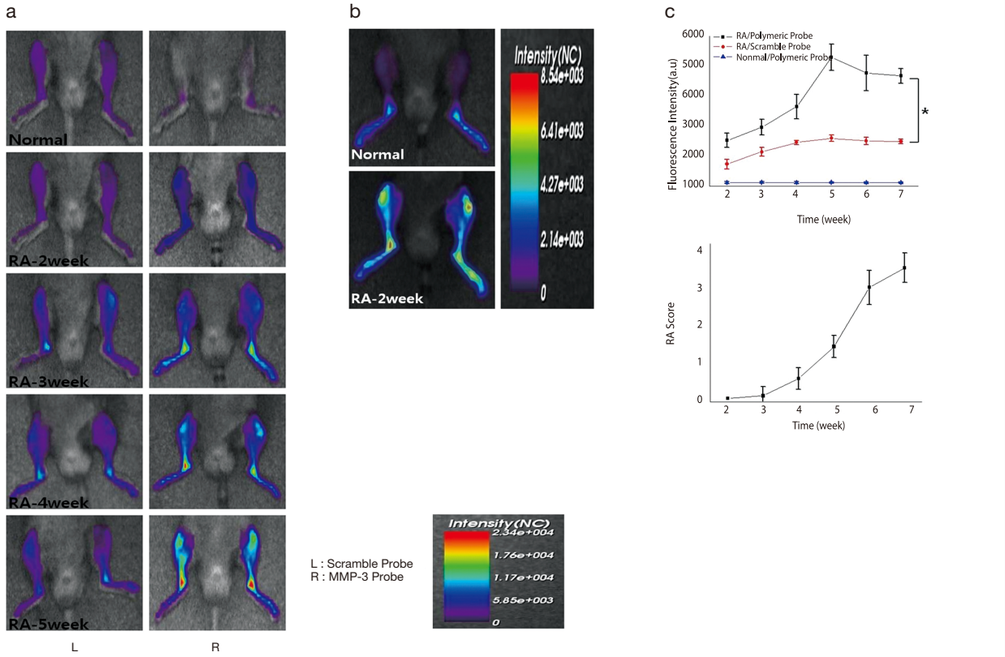

Figure 2. (a) *In vivo* NIRF tomographic images of normal mice and mice with collagen-induced arthritis (CIA) after intravenous injection of MMP-3–specific polymeric probe (n=20) and scrambled probe (n=20) at different stages of arthritis development (2, 3, 4, and 5 weeks after the first immunization).
(b) The recovered NIRF intensity in hind limbs over time after the first immunization. (c) NIRF reflectance imaging of a normal mouse and a mouse with CIA at 2 weeks after the first immunization.
(d) Association between the fold increase in recovered NIRF intensity in hind limbs and increasing arthritis severity scores, as evaluated following administration of an MMP-3–specific polymeric probe and a scrambled probe to the mice with CIA (n=40). Values are the meanSEM. *= P< 0.05 by one-way analysis of variance.

the course of arthritis development and was maximal at 5 weeks after the first immunization (Figures 2a and b). However, the NIRF signal from the arthritic joints was substantially reduced when the scrambled probe was intravenously injected into mice with CIA. A significantly higher NIRF signal was recovered from arthritic joints compared with normal joints at 14 days after the first immunization, before any erythema or swelling could be observed with the naked eye or any erosion was detected in the histologic analysis or micro-CT, thereby enabling a clear early diagnosis of RA (Figure 2c).

The imaging responses observed when the arthritis severity score increased were also evaluated when administering the MMP-3–specific polymeric probe or the scrambled probe to the mice with CIA. When using the MMP-3–specific polymeric probe, the signal intensity increased according to the arthritis severity score until a severity score of 2 was reached, whereas there was only a minimal increase in the fluorescence signal with the scrambled probe for any score (Figure 2d).

The difference in the signal intensities between the MMP-3–specific polymeric probe and the scrambled

probe was highest at a severity score of 2 (mean ± SD 5.2 ±0.70–fold and 2.4 ±0.20–fold increase for MMP-3–specific polymeric probe and scrambled probe, respectively; $P < 0.001$). Additionally, we observed that the arthritis scores of each group were not different, thereby confirming that the injection of the MMP-3 probe and scrambled probe did not alter the disease course in the CIA model (data not shown).

Histological analysis of cartilage destruction and protein assay for MMP-3

The arthritic joints were analyzed using immunohistochemistry and Western blotting to confirm whether the pattern of MMP-3 expression was correlated with the NIRF signal in the *in vivo* imaging. When using fluorescence microscopy, a strong FPR-675 fluorescence signal was observed from mice with CIA that were injected with the MMP-3–specific polymeric probe, whereas only a faint signal was observed from normal mice injected with the MMP-3–specific polymeric probe. As shown in Figure 3a, this is consistent with the *in vivo* imaging results in Figure 2a. Meanwhile, the Western blot using an MMP-3 antibody displayed 57-kd (pro form) MMP-3 and 28-kd (active form) MMP-3 (Figure 3b). The signal intensity of the Western blot for MMP-3 also slowly increased as arthritis developed and was strongest at 5 weeks after the first immunization. The staining signal recovered for the anti–MMP-3 antibody was similar to the pattern of the MMP-3 signal intensity as analyzed by Western blotting (Figure 3c). Similarly, histologic analysis of arthritic knee joints showed that synovial membrane

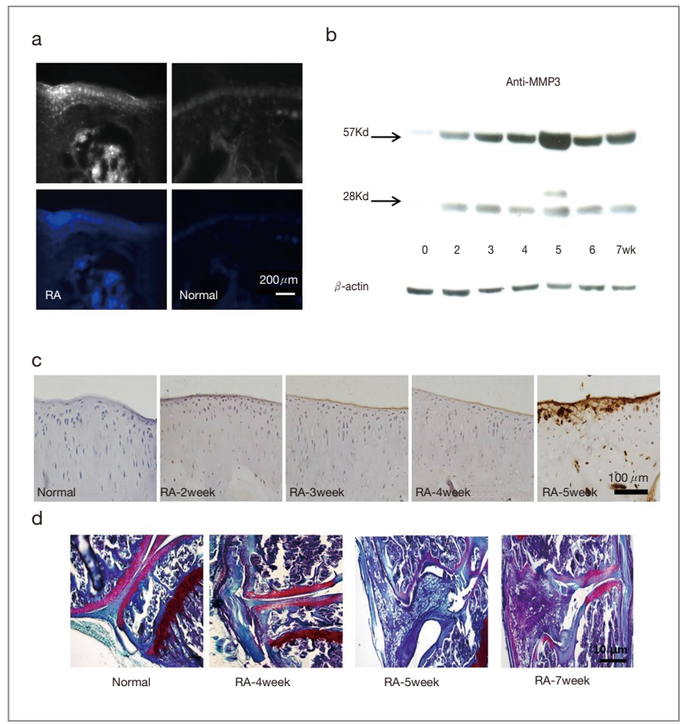

Figure 3. (a) Brightfield and NIRF microscopy of a mouse with collagen-induced arthritis, a model of RA, and a normal mouse, both of which were injected with MMP-3–specific polymeric probe (n=10). (b) Western blot showing expression of anti–MMP-3 at different stages of arthritis development following the first immunization. MMP activity at 57 kd and 28 kd is known to represent the pro form and the active form of MMP-3, respectively. β-actin was used as loading control. (c) Staining signal for anti–MMP-3 antibody in specimens from normal joints and arthritic joints at different stages of arthritis development following the first immunization (n= 10). (d) Safranin O staining of an arthritic knee joint at 0, 4, 5, and 7 weeks after the first immunization (n=3).

degradation sharply increased 4–5 weeks after the first immunization (Figure 3d). In normal knee joints, no inflammation or bone erosion was observed. However, synovial membrane inflammation slightly increased at 4 weeks after RA induction, with the increase sustained at 5–7 weeks after RA induction. Therefore, the results of immunohistochemical and Western blot analyses confirmed that the fluorescence recovered in *in vivo* imaging using the MMP-3–specific polymeric probe was strongly related to up-regulated MMP-3 activity in joint tissues.

Bone structure analysis using micro-CT

Histologic analysis and micro-CT were also performed to assess arthritis progression in mice with CIA. The histologic examination revealed a slow progression of cartilage destruction after the second immunization (Figure 4a). The knee joint section from a normal mouse showed regular cartilage surfaces with a clear demarcation at the cartilage–bone interface. In the knee joint section from a mouse with CIA 3 weeks after the first immunization, the structure of the cartilage layer was maintained, with only a slight reduction in Safranin O staining. However, a loss of Safranin O staining was observed at 5 weeks after the first immunization, indicating erosion of the cartilage. In the reconstructed 3-dimensional micro-CT images of the joint tissues and the hind limbs of a mouse with CIA, loss of bone integrity and damage were clearly visible at 4 and 5 weeks after the first immunization (Figure 4b). However, the knee joints and the paws of a mouse with CIA showed no evidence of bone erosion at 2 weeks after the first immunization and appeared similar to those of a normal mouse.

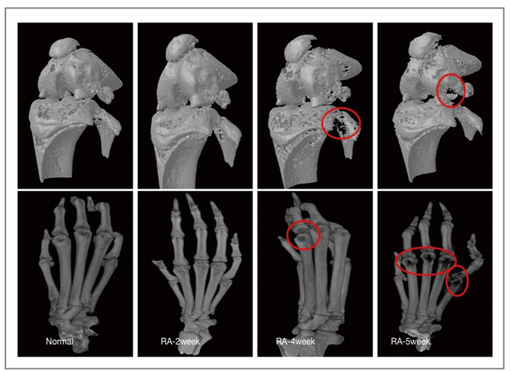

Figure 4. Joint damage as visualized using micro–computed tomography (micro-CT). Three-dimensional reconstructions of micro-CT images of the knee joints and the paws of normal mice and mice with collagen-induced arthritis at 2, 4, and 5 weeks after the first immunization are shown. Circled areas show bone erosion (n= 5).

Conclusion

A noninvasive method for the early diagnosis of RA clearly would be valuable in terms of therapy and prognosis. Therefore, this study used an NIRF optical imaging system to investigate whether an MMP-3–specific polymeric probe could be used for the early diagnosis of RA in a mouse model of CIA and for visualization of arthritis progression [1]. The MMP-3–specific polymeric probe clearly recovered significant fluorescence signals for MMP-3 *in vitro*.

Moreover, the use of an MMP-3–specific polymeric probe allowed clear early diagnosis of RA at 14 days after the first immunization, before any signs of structural or anatomic changes could be detected by the naked eye or histologic and micro-CT analyses.

In this study, MMP-3 was used as a biologic marker for RA because of the increasing evidence that elevated MMP activity, most notably MMP-3 activity, is involved in the development of RA [2]. Although an increase in the serum level of MMP-3 does not occur only in RA, up-regulated MMP-3 activity can be a specific marker of joint inflammation and destruction in RA, because MMP-3 is known to be exclusively generated from inflamed synovial tissue, and the serum level of MMP-3 has also been correlated with markers of inflammation (the ESR and the CRP level) [3,4].

Nevertheless, for the early diagnosis of RA, additional biomarkers besides MMP-3 could also be monitored simultaneously using different biomarker-conjugated fluorophores or fluorescent proteins emitting in different spectral bands. Therefore, there is a need to develop different RA-specific biomarkers that are preferentially increased during the early stages of RA rather than in late stages. In summary, use of an MMP-3–specific polymeric probe facilitated a clear early diagnosis of RA at 14 days after the first immunization and before any signs of structural or anatomic changes could be detected by the naked eye or by histologic analysis and micro-CT.

In addition, an MMP-3–specific polymeric probe provided visualization of arthritis progression by using an NIRF optical imaging system. Therefore, this approach has significant potential with respect to early diagnosis and for monitoring drug and surgical therapies in individual cases. Moreover, it can be used to investigate specific biologic changes involved in the progression of RA.

Note

This article and images are cited from “Early Diagnosis of Arthritis in Mice With Collagen-Induced Arthritis, Using a Fluorogenic Matrix Metalloproteinase 3–Specific Polymeric Probe” in *Arthritis and Rheumatism*, Vol. 63 (12), pp. 3824~3832.

References

[1] Hansch A, Frey O, Sauner D, Hilger I, Haas M, Malich A, et al. *Arthritis Rheum* 2004; 50: 961–7.

[2] Tchetverikov I, Lard LR, DeGroot J, Verzijl N, TeKoppele JM, Breedveld FC, et al. *Ann Rheum Dis* 2003; 62: 1094–9.

[3] Posthumus MD, Limburg PC, Westra J, Cats HA, Stewart RE, van Leeuwen MA, et al. *Rheumatology (Oxford)* 1999; 38: 1081–7.

[4] Young-Min S, Cawston T, Marshall N, Coady D, Christgau S, Saxne T, et al. *Arthritis Rheum* 2007; 56: 3236–47.

[5] Lee S, Ryu JH, Park K, Lee A, Lee SY, Youn IC, et al. *Nano Lett* 2009; 9: 4412–6. 20.

[6] Ryu JH, Lee A, Na JH, Lee S, Ahn HJ, Park JW, et al. *Amino Acids* 2011; 41; 1113-22

[**Technical Review**]

Eco-Friendly Emissive ZnO-Graphene Quantum Dots for Light-Emitting Diodes

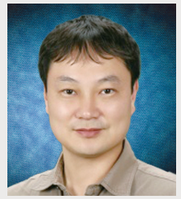

Dong-Ick Son
Interface Control Research Center
eastwing33@hanmail.net

Won-Kook Choi
wkchoi@kist.re.kr

The term “quantum dot” was first coined by Yale physicist Mark Reed in the late 1980’s to describe the strange way in which extremely small semiconductor crystals (typically measuring between 2 and 10 nm, or about 50 atoms in size) seem to take on the characteristic properties of both bulk materials and discrete atoms. First discovered by Louis E. Brus at Bell Labs a few years previously, quantum dots can be made to absorb light efficiently and respond by emitting very specific wavelengths.

This scaling effect allows for tuning a quantum dot’s optical properties to suit a set of specific needs. Quantum dots can also be suspended in a solution. They can be injected, painted or stamped like a photonic ink using low-cost printing or coating techniques. In light of these properties, quantum dots have huge potential in a wide range of applications, ranging from biomedical imaging, lighting, memory, and display technologies to low-cost solar cells and security tagging.

The unusual behaviour of quantum dots results from a phenomenon called quantum confinement. This occurs when semiconductor crystals are grown to be so small that their size falls within the dimensions of a critical quantum limit known as the exciton Bohr radius. Quantum structures containing nanoparticles have attracted much attention because of their potential applications in optoelectronic devices operating at lower currents and higher temperatures [1-3].

Quantum dots owe their unique light emission and absorption properties to their small size and resulting quantum confinement [4]. Simply by changing the particle size, it is possible to tune their bandgap, emission color and absorption spectrum throughout visible and infrared wavelengths (Figure 1).

Figure 1. Colloidal quantum dots (CdSe/ZnS core shell type).

Furthermore, their tiny size enables them to be manipulated in a solution, so quantum dots can be processed using a range of liquid-based methods such as inkjet printing and spin coating. In general, these processing techniques are lower in cost, and amenable to large-area processing in ways that vacuum-based processes associated with normal semiconductor devices are not. Thus, quantum dots are an inorganic semiconductor technology that can be extended to large-area manufacturing such as required by the display industry, and that can be directly integrated onto existing backplane technology. Conventional semiconductor devices must be grown in a vacuum using expensive epitaxial growth techniques that cannot be performed over large areas; in contrast, colloidal quantum dots can simply be poured over a suitable substrate. Colloidal quantum dot technology can support the continual adoption of displays, detectors and other optoelectronic devices into new products.

Of particular importance in the field is quantum-dot LED (QD-LED) technology which is progressing at a rapid pace and continues to close the performance gap with organic LEDs (OLEDs) and liquid crystal displays (LCDs). Figure 2 shows the evolution of quantum dot LED peak efficiency over time, from the early demonstration of 0.001% efficient electroluminescence in 1994 [5] to QD Vision’s recent report of devices with 7% external quantum efficiency (and as high as 14 lm W^{-1}) [6]. Clearly the technology is rapidly approaching the efficiency of OLEDs, and a device stability chart would show a similar trend.

Dabbousi et al. investigated the LED properties of CdSe nanocrystallites (quantum dots) that were

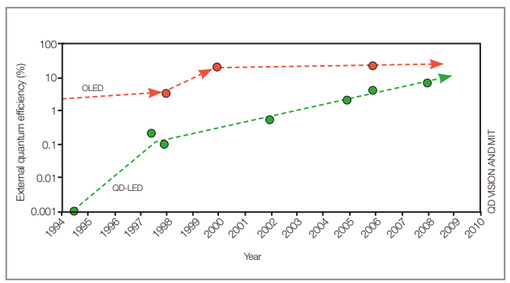

Figure 2. Evolution of the efficiency of QD-LEDs (green circles) over their history, and comparison with OLEDs (orange circles).

incorporated into thin films of polyvinylcarbazole and an oxadiazole derivative and sandwiched between ITO and Al electrodes. It was found that the wavelength of light emitted therefrom could be regulated depending on the size and power conversion efficiency of quantum dots, and that it increased in proportion to low temperatures [7].

In the case of red and green quantum dots, light-emitting efficiency is good, but in order to fabricate a white LED using quantum dots, there is a need to develop a fabrication method for improving blue light emitting efficiency. Previously, CdSe/ZnS core-shell [8] and ZnCdS alloy [9] have been studied as materials for fabricating blue quantum dots, but these materials include Cd. As a prior art relating to quantum dots, QD LEDs used almost CdSe materials for color reproduction such as blue, green and red from the light source until current. However, since Cd is one of six substances banned by the Restriction on Hazardous Substances (RoHS) directive and classified as a hazardous substance, the use of CdSe has been deemed not suitable for the fabrication of photoelectronic devices. KIST researchers have been working on new eco-friendly approaches for fabricating blue quantum dots, and this article summarizes their findings to date.

Metal oxide semiconductor-graphene core-shell quantum dots with Cd-free materials (eco-friendly) are being developed to have a structure in which the surface of a metal oxide semiconductor is covered with graphene through chemical binding between a metal oxide semiconductor material and graphene so that high electroconductivity is formed [10]. These quantum dots convert into zero-dimensional quantum dots, and it is possible to obtain blue light-emitting quantum dots through band gap regulation. These types of hybrid nanostructures that combine inorganic materials and graphene are being developed for applications in fuel cells, batteries, photovoltaics and sensors. However, there have never been demonstrations of light emission from such hybrids with curved single-layer graphene.

In the study summarized below, we present a unique method for synthesizing quasi-ZnO-graphene core-shell structure QDs with Cd-free materials, and we also describe our investigations into the optical and structural properties of QDs produced by various techniques. The chemical synthesis process of ZnO-graphene quasi core-shell structure QDs is graphically summarized in Figure 3.

From a high resolution TEM (HRTEM) image (Figure 4a), it can be clearly seen that the outer shell of ZnO core QD looks like a single graphene layer in the ZnO-graphene quasi core-shell QDs. An enlarged view of the HRTEM image reveals that the interplanar spacing in the crystalline petal is 0.26 nm, which corresponds to the distance between two (002) planes of the hexagonal ZnO phase.

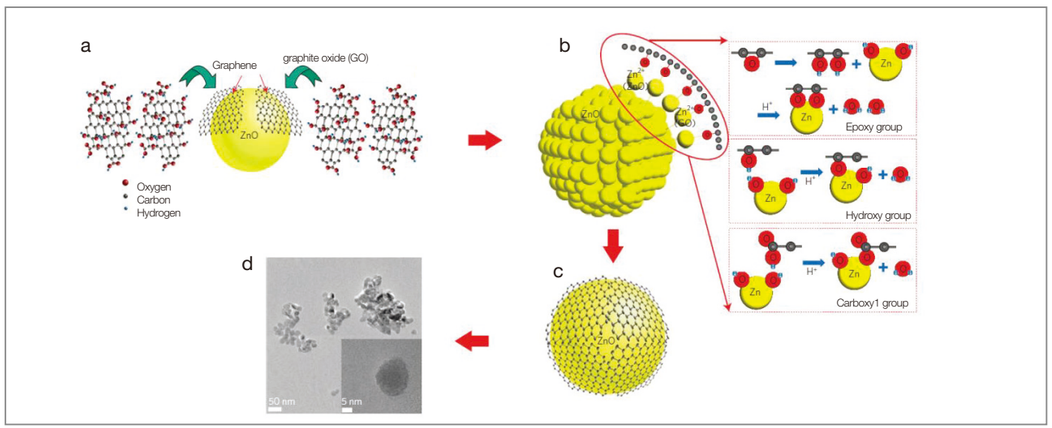

Figure 3. (a) Schematic of chemical exfoliation of graphene sheets from GO. (b) Synthesis of ZnO–graphene quantum dots from GO and zinc acetate dihydrate. The quantum dots were synthesized via chemical reaction between three kinds of functional groups (carboxyl (–COOH), hydroxy (–OH) and epoxy) of GO and Zn^{2+}. The magnified image shows chemical bonding between the functional groups and Zn^{2+}. (c) Schematic of graphene-covered ZnO quantum dots. (d) TEM image. (Inset to d) Enlarged HRTEM image of the ZnO–graphene quantum dots.

As seen from the XRD patterns of ZnO-graphene quasi core-shell QDs (Figure 4b), simultaneous observation of Bragg peaks corresponding to ZnO and graphene indicates that the consolidated ZnO-graphene quasi core-shell QDs were successfully synthesized from graphite oxide (GO)-Zn acetate dihydrate powder.

We measured the Raman spectra of ZnO-graphene quasi core-shell QDs. Note that the doubly degenerate G peak split into two sub-bands, namely, G^+ (1592.7 cm^{-1}) and G^- (1566.6 cm^{-1})[10], while this did not happen for the 2D peak. The G band splitting into two distinct sub-bands (G^+, G^-) resulted from strain-induced symmetry breaking with polarization along the strain and perpendicular to it, and the splitting increased with the increasing strain. This splitting of the G peak can be well explained in terms of the induced strain due to the bending of graphene surrounding the ZnO QDs. According to the band-gap calculation of G band splitting, the magnitude of the band-gap opening (ΔE) of graphene linearly depends on the strength of the applied uniaxial strain and the induced strain of ε=0.8% is approximately equivalent to a band-gap opening of about ΔE=250 meV. This result can be interpreted to mean that graphene attached onto ZnO was changed from a metal into a semiconductor.

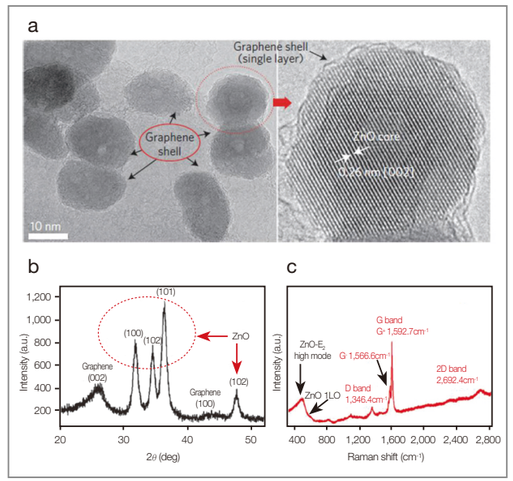

Figure 4. (a) HRTEM image of ZnO quantum dots covered by graphene. (b) X-ray diffraction pattern of ZnO–graphene quasi-core–shell quantum dots. (c) Raman spectra of ZnO–graphene quasi-core–shell quantum dots.

Figure 5a presents photoluminescence spectra at room temperature for the ZnO–graphene quantum dots. For the ZnO–graphene quantum dots, two extra emissions peaks at 406 nm (3.05 eV) and 432 nm (2.86 eV) can be seen, with the peak positions differing from those of the pure ZnO quantum dots by as much as 190 meV. To understand the new peaks in the photoluminescence spectra we carried out density of states (DOS) and projected DOS calculations using a simple model with density functional theory (DFT), as implemented in the Gaussian package 24 (Figure 5b). We modelled local structures of graphene (G) with oxygen (O) attachment, with 19 aromatic rings with hydrogen termination at the edge and one oxygen atom bridging the carbon atom(s) in several geometries. Density functional theory calculations reveal that these additional peaks result from a splitting of the lowest unoccupied orbitals of the graphene into three orbitals with distinct energy levels. Considering the broadening of the photo-luminescence peak and inherent properties of DFT, which underestimate the energy gap, this discrepancy would be a systematic error because of its limits in describing the electron–electron interaction, and therefore it does not critically interfere with interpreting the underlying physics. Consequently, the new photoluminescence features in the ZnO–graphene quantum dot can be ascribed to the electronic transitions involving the two unoccupied levels of G–O_{epoxy} (Figure 5c).

In order to investigate the electrical properties of ZnO-graphene QD, an LED with the structure of Al/Cs_2CO_3/ZnO-graphene QD/poly-TPD/PEDOT:PSS/ITO/Glass was fabricated. Figure 6a shows electrical properties of the light-emitting diode. The voltage for

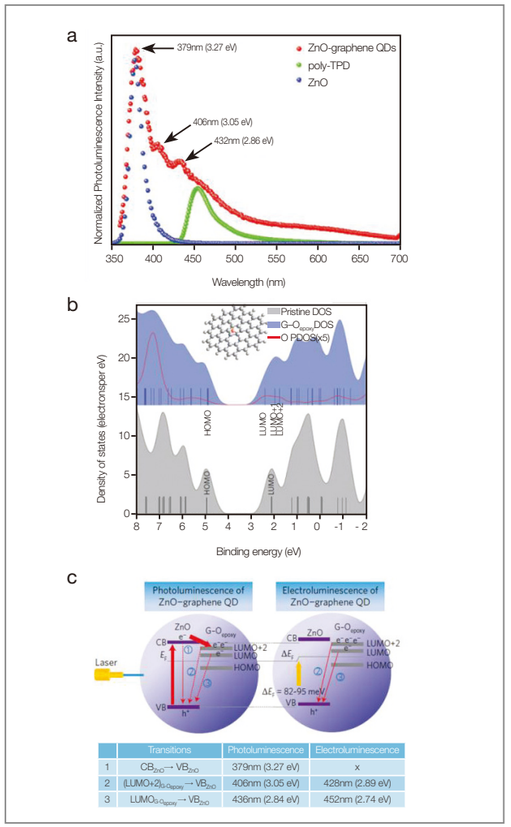

Figure 5. (a) Photoluminescence spectra with normalized intensity for ZnO quantum dots, poly-TPD and ZnO–graphene quantum dots. (b) DOS of graphene and the graphene (G)–oxygen (O) model. DOS of pristine (grey shaded) and G–Oepoxy (blue shaded) graphene models are shown. (c) PL and EL transition scheme for ZnO–graphene QDs. Transitions 1, 2 and 3 correspond to electron transitions from the conduction band (CB) of ZnO, LUMO+2 and LUMO levels induced by G–O_{epoxy} to the valence band (VB) of ZnO, respectively

light emitting was approximately 10 V, and when 15 V was applied, 200 mA/cm^2 of current density was observed. ITO was an anode electrode in which the first conductive polymer layer (PEDOT:PSS) was used as a hole injection layer promoting the introduction of holes into the organic layer. In order to examine photoluminescence properties of the light-emitting diode, electroluminescence (EL) was measured, as shown in Figure 6b. The light-emitting energy of electron transition from the LUMO (lowest unoccupied molecular orbital) and HOMO (highly occupied molecular orbital) of the graphene to the increased valence band (VB) of ZnO decreased as much as the increased Fermi energy, and therefore, in the PL spectrum, the electroluminescence at 406 nm and 432 nm was subjected to a red shift to 428 nm and 450 nm, respectively. Electroluminescence lights at 428 nm and 450 nm were absorbed to poly-TPD and PSS:PEDOT, respectively, and filed emission corresponding to the energy between LUMO and HOMO occurred. Electroluminescence peaks at 490 nm and 606 nm were due to such field emission. Figure 6c is a schematic energy band diagram of the light-emitting diode. In the above light-emitting diode, the second conductive polymer (Poly-TPD) layer was used as a hole transport layer, and the zinc oxide-graphene nanoparticle received electrons introduced from Al (cathode) and holes transported from the second conductive polymer (Poly-TPD) layer via a hopping mechanism. As a result, the diode showed light-emitting properties by re-combining the electrons and holes in the zinc oxide-graphene quantum dots. Figure 6d is an electroluminescence graph of the polymer hybrid light-emitting diode comprising the zinc oxide-graphene quantum dots when +15 V of voltage was applied. Meanwhile, color indices of emission (CIE) were (0.23, 0.20), (0.28, 0.24) and (0.31, 0.26) in forward orientation upon applying 13, 15 and 17 V of voltage, respectively. Brightness was about 800 cd/m2 (at 15V), and almost white light was observed with the naked eye.

On the basis of these investigations, it was found that when voltage was applied, the light-emitting diode using the metal oxide semiconductor-graphene core-shell quantum dots could induce filed emission to the difference in energy level between the LUMO and HOMO of graphene and the valence band (VB) of the metal oxide semiconductor linked thereto. Based on this principle, red, green and blue electroluminescences, useful for the fabrication of a white light-emitting diode,

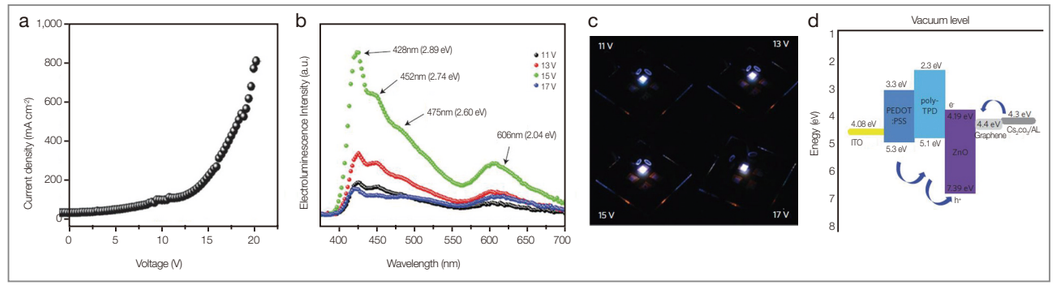

Figure 6. (a) Current density–voltage (J–V) characteristics for the fabricated LED device. (b) Electroluminescence spectra of the fabricated ZnO–graphene quasi-quantum dot LED device with applied voltages from 11 to 17 V. (c) Band diagram of the fabricated LED device. The HOMO and LUMO levels of PEDOT:PSS, poly-TPD, graphene and ZnO are taken from ref. 10. The pathways of holes and electrons are indicated by arrows. (d) Photograph of light emission at 11, 13, 15 and 17 V applied bias.

occurred in the ranges shown in Figure 7. This figure illustrates the relationship of a light-emitting energy level to multi-component oxide semiconductor materials in which valence band energy levels of semiconductor nanoparticles, that are chemically linked to the graphene used in implementing red (610-630 nm (1.96-2.03 eV)), green (520-540 nm (2.29-2.38 eV)) and blue (440-460 nm (2.69-2.81 eV)) among electroluminescence, are in the range of 6.30-6.45 eV (red), 6.65-6.80 eV (green), and 7.00 7.25 eV (blue), respectively.

As is evident from these results, our research at KIST has been successful in using a Cd-free intermediate consolidated quasi-metal oxide-graphene core-shell QD as a newly developed material appropriate for a functional electron transport layer with high potential in fields associated with DSSCs, photovoltaic devices, sensors, and light-emitting diodes.

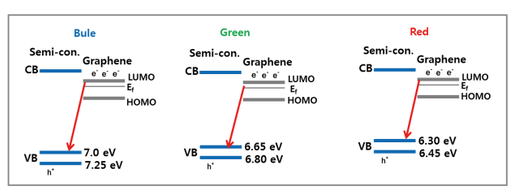

Figure 7. Schematic diagram of a light-emitting diode with various multi-component Cd-free metal oxide semiconductors.

Acknowledgement

This work is financially supported by the KIST Future Resource Program (2E22735).

Note

This article and images are cited from “Emissive ZnO–graphene quantum dots for white-light-emitting diodes” in *Nature Nanotechnology*, Vol. 7, pp. 465-471.

References

[1] Achermann M, Petruska MA, Kos S, Smith DL, Koleske DD, and Klimov VI. *Nature* 2004; 429: 642.
[2] Warburton RJ, Schaflein C, Haft D, Bickel F, Lorke A, Karrai K, Garcia JM, Schoenfeld W, *Petroff PM. Nature* 2000; 405: 926.
[3] Craig NJ, Taylor JM, Lester EA, Marcus CM, Hanson MP, Gossard AC. *Science* 2004; 304: 565.
[4] Brus LE. *J. Chem. Phys.* 1984; 80: 4403.
[5] Colvin VL, Schlamp MC, Alivisatos AP. *Nature* 1994; 370: 354.
[6] http://www.qdvision.com/news_090206.html
[7] Dabbousi BO et al., *Appl. Phys. Lett.* 1995; 66: 1316.
[8] Li Y, Rizzo A, Cingolani R, Gigli G. *Adv. Mater.* 2006; 18: 2545.
[9] Beard MC, Knutsen KP, Yu P, Luther JM, Song Q, Metzger WK, Ellingson RJ, Nozik A. *J. Nano Lett.* 2007; 7: 2506.
[10] Son DI, Kwon BW, Park DH, Seo W, Yi Y, Angardi B, Lee C, Choi WK. *Nat. Nanotechnol.* 2012; 7: 465.

[Feature Articles]

In Situ Synthesis of Thermochemically-Reduced Graphene Oxide Conducting Nanocomposites

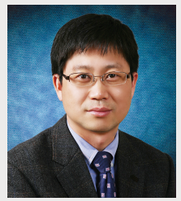

Bon-Cheol Ku
Institute of Advanced Composite Materials
cnt@kist.re.kr

Introduction

The need for an organized synthesis of robust graphene-based electrically-conductive polymer composites has sparked the recent fascination with conductive reduced graphene oxide (R-GO) composites. A wide range of applications has been successfully realized and include flexible nanoelectronics [1], sensing [2], supercapacitors [3] and multifunctional membranes [4]. While it is well-known that graphene has outstanding electrical and thermal properties as well as an extremely high surface area, it is also easily and irreversibly coagulated in aqueous media and polar solvents. At the same time, GO can be individually dispersed as a single layer in polar solvents and polymer matrix. The degree of dispersion of graphene and GO in the polymer matrix is one of the critical factors in enhancing the physical properties of composites. However, R-GO is significantly agglomerated when the chemical reduction step precedes the introduction of the polymer. *In-situ* polymerization gives rise not only to a high degree of dispersion of GO in monomer solution, but also to thermal reduction of GO at high temperatures.

The electrical conductivity of GO-based polymer composites can also be improved by the thermochemical reduction (~ 300°C) of GO in high performance polymers, which is critically important to almost all potential applications. High performance polymers, polyimides (PI), are synthesized at high temperatures (> 300°C) and have wide applications ranging from microelectronics to aerospace due to excellent thermal stability, excellent mechanical properties, and good chemical resistance [5, 6].

This article reports on a well-organized process, the *in situ* synthesis of thermochemically-reduced GO, to fabricate highly electrically-conductive polymer nanocomposites. To enhance the electrical conductivity of GO/PI composites, the surface functionalization of GO was further carried out with aryl diazonium salt [7] including 4-iodoaniline to form aryl-functionalized graphene oxide (I-Ph-GO). We also fabricated thermochemically-converted GO (R-I-Ph-GO)/PI composites having high electrical conductivity.

Experimental results

A thermochemically-reduced GO was synthesized by a simply developed chemical process as depicted in Figure 1. The functionalized GO (I-Ph-GO) from graphite oxide was prepared using aryl diazonium salt followed by thermal treatment at 300°C. As a control group, Ph-GO without an iodo group was synthesized to investigate the effect of iodo group on the reduction of GO. The representative Raman spectra from graphitic nanostructures including functionalized and reduced GO gave us two strong major bands to determine the structural confinement: a G-band at around 1580 cm^{-1} and D-band at around 1350 cm^{-1}. The D-band is a longitudinal optical phonon and is known as the defect mode. The tangential mode in graphitic structure is closely linked to the G-band and involves the stretching of the sp^2 bonds. The D-band and G-band intensity ratio (A_D/A_G) indicates the degree of disorder from graphitic structure. Figure 2a represents the intensity ratio of the D and G bands for GO and I-Ph-GO as a function of thermal treatment time. It was found that the A_D/A_G ratio of a functionalized GO decreased as thermal treatment time increased, confirming that the iodo-functionalized GO (I-Ph-GO) showed a better sp^2 crystallinity compared to GO. The better sp^2 crystallinity provided a higher intensity of the G-band, resulting in a decreasing A_D/A_G ratio.

Figure 2b shows the XRD patterns of functionalized and reduced GO. GO demonstrated a broad peak near a 2θ value of 11.9° (d-spacing value: 7.63Å). This figure also illustrates that Ph-GO and I-Ph-GO showed a significant shift to higher 2θ angles.

The GO is readily reduced by aniline in an aqueous acid medium, with the aniline simultaneously undergoing

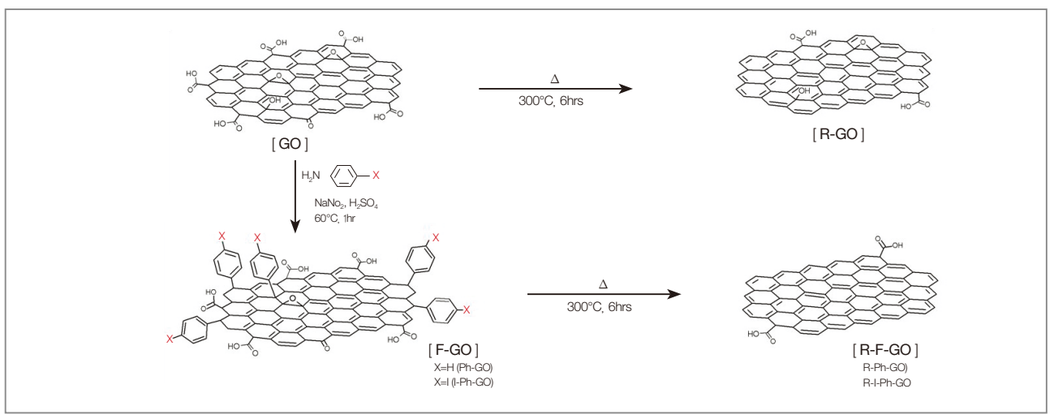

Figure 1. Schematic of functionalized graphene oxide (F-GO) and reduced graphene oxide (R-F-GO). Phenyl functionalized GO (Ph-GO) and GO can be thermally reduced. 4-iodophenyl functionalized GO (I-Ph-GO) can be thermochemically reduced at 300°C.

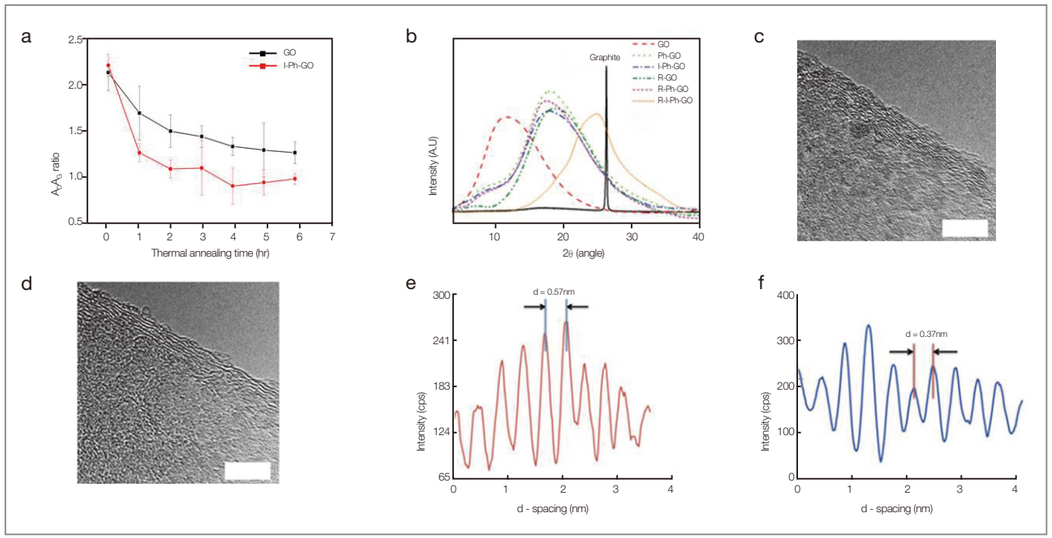

Figure 2. (a) Raman A_D/A_G ratio of GO and I-Ph-GO with thermal treatment time. (b) XRD patterns of functionalized graphene oxide and reduced functionalized GO. (c) and (d) HR-TEM images of R-GO and R-I-Ph-GO, respectively. The scale bars are 4nm. (e) and (f) Cross-section of R-GO and R-I-Ph-GO, respectively.

oxidative polymerization to produce the reduced GO-polyaniline composites [8]. During functionalization of GO with aniline derivatives such as 4-iodoaniline for I-Ph-GO and aniline for Ph-GO, the GO is considered to have undergone electrochemical reduction.

Again as depicted in Figure 2b, it is clearly seen that functional groups such as the oxygen of I-Ph-GO were removed much faster than GO. After thermal treatment, the d-spacing decreased due to the removal of functional groups from the surface or interlayers of GO.

The d-spacing difference of R-Ph-GO with Ph-GO was negligible. R-I-Ph-GO, however, had even smaller d-spacing than the RGO. It has been demonstrated that the iodo groups on the interlayer of GO enhance the sp^2 crystallinity and ordering of graphene sheets [9]. Furthermore, the low d-spacing between the graphene sheets can lead to an increase in electrical conductivity due to a decrease in the contact resistance between individual graphene sheets [8,10]. Figure 2c,d shows high-resolution transmission electron microscopy (HR-TEM) images of a few layered graphene structures of R-GO and R-I-Ph-GO. The well-defined diffraction patterns indicate the crystalline structure of the reduced GO [11]. The interlayer distance between the graphene layers corresponded with the XRD of R-GO and R-I-Ph-GO as shown in Figure 2b.

Figure 3a,b represents TGA thermograms of functionalized GO and reduced GO. The functionalized GO exhibited a two step weight loss. The first weight loss occurred around 100°C ~ 300°C by the loss of functional groups such as carboxylic acid and hydroxyl groups on the surface of functionalized GO [12]. The second weight loss started from around 600°C and continued up to 800°C. GO had more rapid weight loss than Ph-GO and I-Ph-GO. The char yields were also lower than those of Ph-GO and I-Ph-GO. The reduction of GO by aniline derivatives gives rise to the high char yield of functionalized graphene oxide due to an electrochemical reduction by oxidized aniline in acidic media [8].

The thermal stability of reduced GO is depicted in

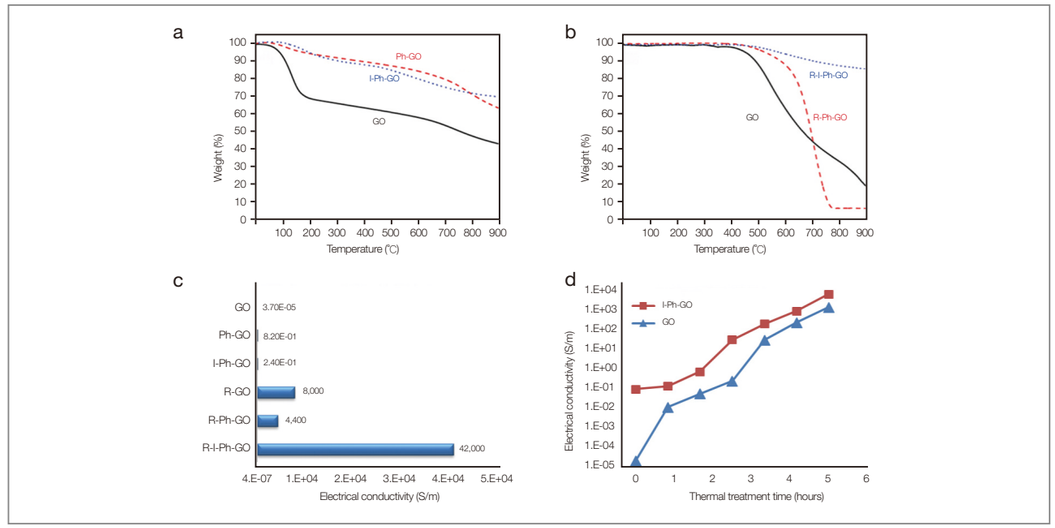

Figure 3. TGA thermograms for: (a) functionalized GO and (b) reduced GO (Heating rate: 5℃/min and nitrogen gas condition). (c) Electrical conductivities of functionalized and reduced GO. (d) Electrical conductivities of GO and I-Ph-GO with thermal treatment time (Thermal treatment temperature: 300℃).

Figure 3b. The thermally-reduced graphene oxide (R-GO and R-Ph-GO) showed a rapid weight loss with a decomposition temperature at 500°C. However, the thermochemically-reduced GO, R-I-Ph-GO, showed higher thermal stability compared to the others. The enhanced thermal stability of R-I-Ph-GO may be explained by the better deoxygenation after thermal treatment, which may increase the conductivity of GO due to restoration of the sp^2-bonded carbon structure [13,14]. The I-Ph-GO can be thermochemically reduced by following the steps presented in Figure 4. A possible reaction mechanism is as follows: 1) the dehalogenation step from I-Ph-GO to form HI in air; 2) the ring-opening reaction of epoxy groups or substitution reaction of a hydroxyl group by the HI released from I-Ph-GO; 3) the elimination reaction of halogen atoms to produce deoxygenated phenyl substituted GO (Ph-GO); and 4) elimination of phenyl groups to restore graphene structure. Previous studies have also shown that phenyl groups on single walled carbon nanotubes (SWCNTs) can be eliminated and pristine SWCNTs can be restored [15].

Figure 3c shows the electrical conductivities of functionalized GO and reduced GO. The electrical conductivities of thermally-and thermochemically-reduced GO powder were measured after drying in a vacuum oven at 90°C overnight to eliminate the contribution of iodine chemical doping into the R-GO and R-I-Ph-GO. The electrical conductivities of Ph-GO and I-Ph-GO improved over 10^4 times that of GO alone due to partial reduction by aniline derivatives [8]. By contrast, the electrical conductivities of thermally-reduced GO (R-GO) and thermochemically-reduced GO (R-I-Ph-GO) were 80 S/cm and 420 S/cm, respectively. On the other hand, the electrical conductivity of thermally-reduced GO (R-Ph-GO) was similar to that of R-GO.

This is clearly explained by the fact that the phenyl groups on the surface of graphene did not affect the restoration of graphene structure during the thermal treatment process. The iodo groups acted as the catalyst for enhancing the electrical conductivity of reduced

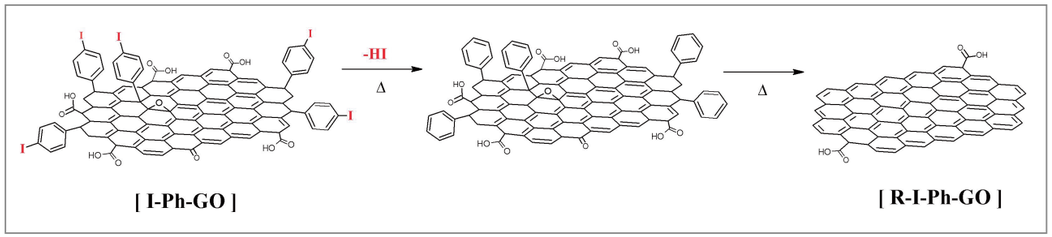

Figure 4. Schematic of proposed thermochemical reduction mechanism of I-Ph-GO.

GO. The enhanced conductivity of R-I-Ph-GO can be attributed to the reduction of GO by the thermal release of HI from I-Ph-GO. It should be emphasized that the iodo content of thermochemically-reduced GO was found to be 0.06% after thermal treatment, which excluded the contribution of iodine chemical doping into the R-I-Ph-GO films. The electrical conductivities of functionalized GO increased as thermal treatment time increased (Figure 3d).

Functionalized GO (I-Ph-GO) was used to prepare graphene-based polymer composites. Polyimides (PI) are well-known high performance materials with excellent thermal stability, mechanical properties, and good chemical resistance [5,6].

I-Ph-GO showed dispersibility as good as GO in the NMP solution (Figure 5), which is very important for the preparation of graphene-based polymer composites. The I-Ph-GO/PAA composite was prepared by solution mixing and was then thermally treated. The I-Ph-GO dispersed in the PI precursor, polyamic acid (PAA) matrix, was considered to be thermochemically reduced at high temperature during the imidization process. The

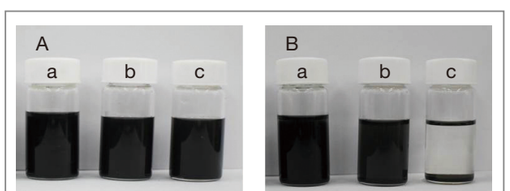

Figure 5. Photographs of: (a) GO (b) I-Ph-GO (c) Ph-GO dispersed in NMP (1 mg/mL). The photographs were taken (A) 1 h after and (B) 1 day after preparing GO dispersion.

electrical conductivities of R-I-Ph-GO/PI and R-GO/PI composite films with 10 wt% (5.9 vol%) reduced GO in a polymer matrix were 8.7×10^{-1} S/m and 1.2×10^{-5} S/m, respectively. The electrical conductivity (~1 S/m) of the R-I-Ph-GO/PI composite, which is sufficient for many electrical applications [16], improved over 10^4 times that of R-GO/PI composites. The graphitization resulting from deoxygenation of graphene oxide is considered to enhance the electrical conductivity of the composites. The R-I-Ph-GO/PI composites led to more than 10^{14} enhancement in electrical conductivity compared to commercially available pure PI, Kapton® (10^{-15} S/m). An increase in thermochemically-reduced GO in PI composites also yielded a gradual increase in electrical conductivity with values of 10^{-5} S/m at 2 wt% (1.2 vol%) and ~10^{-2} S/m at 5 wt% (3.1 vol%).

Summary

The experimental characterization we conducted clearly shows that thermochemically-reduced GO precursor (I-Ph-GO) has high electrical conductivity (42,000 S/m) and good dispersion in polar solvent (NMP). Blended I-Ph-GO and PAA composites were thermally treated for post-graphitization to form thermochemically-reduced GO (R-I-Ph-GO)/PI composites. R-I-Ph-GO/polyimide (PI) composites fabricated by imidization of polyamicacid (PAA)/I-Ph-GO had 10^4 times higher conductivity (~1 S/m) than RGO/PI composites.

Note

This article and images are cited from "In situ Synthesis of Thermochemically-Reduced Graphene Oxide Conducting Nanocomposites" in *Nano Letters* 2012; 12: 1789.

References

[1] Wang S, Ang PK, Wang Z, Tang ALL, Thong JTL, Loh KP. *Nano Lett.* 2010; 10: 92-98.
[2] Flowler JD, Allen MJ, Tung VC, Yang Y, Kaner RB, Aeiller BH. *ACS Nano* 2009; 3: 301-306.
[3] Gao W, Singh N, Song L, Liu Z, Reddy ALM, Ci L, Vajtai R, Zhang Q, Wei B, Ajayan PM. *Nat. Nonotech* 2011; 6: 496-500.
[4] Garaj S, Hubbard W, Reina A, Kong J, Branton D, Golovchenko JA. *Nature* 2010; 467:190-193.
[5] Ghosh MK, Mittal KL. *Polyimides: Fundamentals and Applications, CRS Press*, 1996. 36.
[6] Hasegawa T, Horie KJ. *Prog. Polym. Sci.* 2001; 26: 256-355.
[7] Bekyarova E, Itkis ME, Ramesh P, Berger C, Sprinkle M, de Heer WA, Haddon RC. *J. Am. Chem. Soc.* 2009; 131: 1336–1337.
[8] Xu LQ, Liu YL, Neoh K-G, Kang E-T, Fu GD. *Macromol. Rapid. Commun.* 2011; 32: 684-688.
[9] Moon IK, Lee JH, Rouff RS, Lee HY. *Nature Commun.* 2010; 1: 73.
[10] Russo S, Craciun MF, Yamamoto M, Morpurgo AF, Tarucha S. *Phys. E.* 2010; 42: 667-679.
[11] Hernandez Y, Nicolosi V, Lotya M, Blighe FM, Sun A, De S, McGovern IT, Holland B, Byrne M, GunKo YK, Boland JJ, Niraj P, Duesberg G, Krishnamurthy S, Goodhue R, Hutchison J, Scardaci V, Ferrari AC, Coleman JN. *Nat. Nonotech* 2008; 3: 563-568.
[12] Dikin DA, Stankovich SE, Zimney RJ, Piner RD, Dommett GHB, Evmenenko G, Nguyen ST, Ruoff RS. *Nature* 2007; 448: 457-460.
[13] Si Y, Samulski T. *Nano Lett.* 2008; 8: 1679-1682.
[14] Bai H, Li C, Shi GQ. *Adv. Mater.* 2011; 23: 1089-1115.
[15] Dyke AC, Tour JM. *J. Am. Chem. Soc.* 2003; 126: 1156-1157.
[16] Chung DDL. *J. Mater. Sci.* 2004; 39: 2645-2661.

[Feature Articles]

Ultrathin Diamond Synthesis on SiO_2

Wook-Seong Lee
Electronic Materials Center
wsleemk@gmail.com

Hak-Joo Lee

Introduction

Diamond thin films have opened innovative approaches for a wide variety of applications [1,2]. Particularly important applications include applying an ultrathin (less than 100 nm in thickness) diamond coating on a SiO_2-coated Si wafer for nano-electro-mechanical system (NEMS) applications [3], applying a hermetic coating over a delicate 3-dimentional geometry of microelectrode arrays for implanted retinal prosthesis [4], and fabricating localized surface plasmon resonance (LSPR) sensors using a thin diamond layer as the dielectric layer [5]. Unfortunately, it is not easy to synthesize an ultrathin void-free diamond layer on a SiO_2 surface due to its low nucleation density (see Figure 1) and long incubation time compared to that of pristine Si substrate [6].

Ultrasonic treatment of a substrate immersed in a diamond powder suspension has been widely adopted for nucleation enhancement [7]. Using this technique, various efforts have been made to enhance the dispersion of transferred particles on the substrate, including functionalization of the seed diamond particle surface as well as addition of surfactant to, or controlling the pH of, the suspension. Ball-milling of the diamond powder using ceramic bead or annealing in contact with hydrogen has also been adopted to remove/break the strong sp^2 carbon bond between individual nano diamond particles for mono dispersion of the seeds. However, such efforts have been

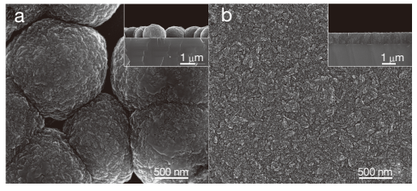

Figure 1. SEM images of UNCD films synthesized for 4 hours by DC-PACVD on: (a) SiO_2/Si substrate; and (b) pristine Si substrate.

directed exclusively to the seed diamond particles in the suspension, not to the substrate onto which the seed is transferred.

In the study described in this article, we investigated the effect of surface modification of SiO_2-coated Si substrate on dispersed nano diamond seed density prior to ultrananocrystalline diamond (UNCD) deposition by exposing the substrate to hydrogen as well as hydrocarbon. We were able to demonstrate for the first time a successful synthesis of a void-free, ultrathin (30 nm in thickness) UNCD film on a SiO_2-coated Si substrate by direct-current plasma assisted chemical vapor deposition (DC-PACVD).

Variable densities of seed and nucleation by substrate surface treatments

Figure 2 shows the HR-SEM images of dispersed nano diamond particles on SiO_2-coated Si substrates before and after the following pretreatments: (a) untreated (denoted as SiO_2/Si); (b) treated by hydrogen plasma (denoted as *SiO_2/Si); (c) treated by hydrocarbon plasma (denoted as $^{\dagger}SiO_2$/Si); and (d) thermally treated in a hydrocarbon atmosphere (denoted as $^{\ddagger}SiO_2$/Si). The insets show a magnified view of the respective samples. It was remarkable that the dispersed seed densities varied drastically according to the respective surface pretreatments. The dispersed seed densities obtained from the images were (a) 7.8 x 10^{10}, (b) 4.8 x 10^{11}, (c) 3.2 x 10^{7} and (d) 7.6 x 10^{8} nuclei/cm^2, respectively. The best result was obtained for the *SiO_2/Si substrate (hydrogen plasma treatment), as shown in Figure 2b. The dispersed seed density on the *SiO^2/Si substrate (Figure 2b) increased by a factor of 6 relative to that on the SiO^2/Si substrate (Figure 2a). By contrast, seed densities on the substrate exposed to other pretreatments (Figures 2c and 2d) were drastically reduced compared to that on the untreated substrate (Figure 2a). It was remarkable that not only the seed densities but also the seed dispersion (consequently the agglomeration), was sensitive to the substrate treatments.

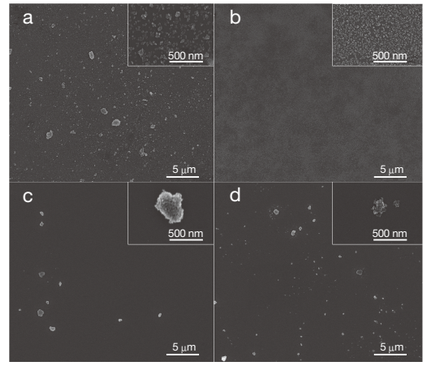

Figure 2. Dispersion of nano diamond seed particles by ultrasonic treatment on the following substrates: (a) pristine SiO_2/Si; (b) hydrogen-plasma-treated SiO_2/Si (*SiO_2/Si); (c) hydrocarbon-plasma-treated SiO_2/Si ($^{\dagger}SiO_2$/Si); and (d) hydrocarbon-thermal-treated SiO_2/Si ($^{\ddagger}SiO_2$/Si).

Figure 3 compares HR-SEM images of the seeded SiO_2/Si (Figure 2a) and *SiO_2/Si (Figure 2b), after UNCD coating for 30 min by DC-PACVD. Note the pronounced

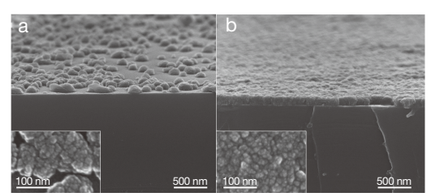

Figure 3. SEM images of UNCD films synthesized for 30 min by DC-PACVD on the respective seeded substrates shown in Fig 2: (a) pristine SiO_2/Si; and (b) hydrogen-plasma-treated SiO_2/Si (*SiO_2/Si).

effect of the hydrogen plasma treatment on the UNCD layer development, which might again be attributed to the seed dispersion densities on the respective substrates.

Figure 4a shows the plan-view HR-TEM image of the UNCD film shown in Figure 3b. The majority of the grains were less than 10 nm in diameter. The inter-planar spacing shown in the inset was 2.06 Å, which corresponded to that of the diamond (111) planes. Figure 4b shows the near edge x-ray absorption fine structure (NEXAFS) C-K edge spectra taken from the same sample. The spectra taken from the HOPG (highly oriented pyrolytic graphite) are also shown for comparison. A sharp peak at 289.3 eV (C 1s→σ* transition) and the large dip at 302.2 eV (second absolute band gap) are the well-known fingerprints of diamond. A sharp peak at 285.5 eV (C 1s→π* transition) was observed for HOPG, whereas it was absent in the spectra taken from the UNCD sample.

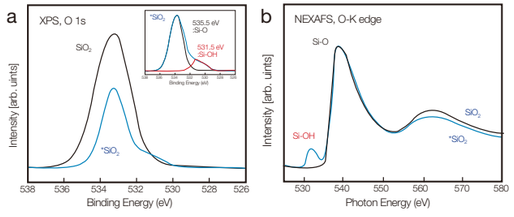

Figure 4. (a) XPS O 1s spectra. (b) NEXAFS O-K edge spectra of pristine SiO_2/Si and hydrogen-plasma-treated SiO_2/Si ($^*SiO_2$/Si) substrates.

Effects of electrostatic interactions between diamond seed and substrates

The drastic enhancement of the dispersed seed density should be attributed to some modification of the molecular structure of the respective substrate surfaces as described below. Figure 5a shows the XPS O 1s spectra taken on the surfaces of the pristine SiO_2/Si and $^*SiO_2$/Si substrates prior to the seeding/UNCD deposition. Note that the peak in the spectrum of the

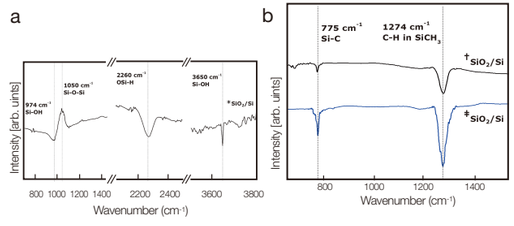

Figure 5. FTIR spectra of: (a) hydrogen-plasma-treated SiO_2/Si ($^*SiO_2$/Si) substrate; and (b) hydrocarbon-plasma-treated SiO_2/Si (†SiO22/Si) and hydrocarbon-thermal-treated SiO_2/Si ($^\ddagger SiO_2$/Si) (signals from pristine SiO_2/Si substrate were subtracted as background).

non-treated SiO_2/Si substrate was symmetrical at about 533.5 eV, a finding typical of Si-O bonding. By contrast, the peak from the $^*SiO_2$/Si substrate was asymmetrical, with contributions from an additional band, as shown in the inset. The new band around 531.5 eV was attributed to the Si-OH group (also known as the silanol group). This was further supported by findings illustrated in Figure 5b which shows the NEXAFS O Kedge spectra taken from the same substrates. The small peak around 532 eV in the spectrum of $^*SiO_2$/Si was also attributed to the silanol group.

It was still further confirmed by the FTIR absorption spectra taken from the $^*SiO_2$/Si substrate, as shown in Figure 6a. The spectrum from the pristine SiO_2/Si was subtracted from it as the background. The three dips at 974 cm^{-1} (Si-OH), 2260 cm^{-1} (SiO_3-H) and 3650 cm^{-1} (Si-OH) were attributed to the newly-formed bonds on the $^*SiO_2$/Si substrate relative to the pristine SiO_2/Si substrate, while the peak at 1050 cm^{-1} (Si-O-Si) was attributed to the dip present in the spectrum of the pristine SiO^2/Si substrate, which was subtracted as background.

By contrast, the FTIR absorption spectra taken from the $^\dagger SiO_2$/Si and $^\ddagger SiO_2$/Si substrate (see Figure 6b), where the spectrum from the pristine SiO_2/Si was also subtracted from it as the background, greatly differed from that shown in Figure 6a. The dips were observed at 775 cm^{-1} and 1274 cm^{-1}, which were attributed to the Si-C, and the C-H bond in Si-CH_3, respectively. This indicated the carburization as well as the Si-CH_3 termination on

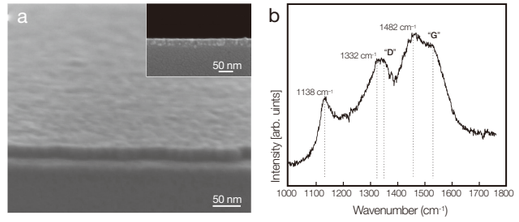

Figure 6. (a) HR-SEM images and (b) Raman spectra of an ultrathin (about 30 nm in thickness) UNCD film on a quartz substrate pretreated by hydrogen plasma using DC-PACVD prior to ultrasonic treatment and subsequent UNCD deposition for 10 min by DC-PACVD.

the surface of the substrates treated by the hydrocarbon plasma as well as that treated by the hydrocarbon thermal atmosphere.

Based on these findings, it is evident that the hydrogen plasma treatment resulted in Si-OH termination, while the hydrocarbon plasma/thermal treatment resulted in Si-CH_3 termination on the SiO_2 surfaces. One could easily expect that such new surface terminations would result in some modifications in the electrostatic nature of the surface due to some difference in the polarities of the respective surface terminating groups. To confirm this, we analyzed the zeta potentials of such substrates in two different ways. Table 1 shows the zeta potentials of the substrate surface (ζ_s), obtained by using the standard monitor solution, as well as that measured by using the actual seeding suspension. The former changed little while the latter changed drastically, according to the respective surface pretreatments of the substrates. The former stayed within a relatively narrow range between -21.63 mV and -31.03 mV while the latter varied widely from -63.84 mV to +14.85 mV.

It was also remarkable that the zeta potentials of the nano diamond particles (ζ_p), measured by using the actual seeding suspension in contact with the respective substrates, were also strongly dependent on the respective substrate surface pretreatments; they varied widely from +1.82 mV to +37.51 mV. This indicated that the diamond particle and substrate surface, both in contact with the liquid media of methanol, were mutually interacting electrostatically during the measurements, as well as in the actual ultrasonic seeding process. Also note that the polarity of the zeta potential of the nano diamond particle in the seeding suspension was positive, while those of the substrates in contact with the suspension were mostly negative, except for the $^\ddagger SiO_2$/Si. The origin of such opposing polarity of the nano diamond particle, with respect to that of the substrate, might be attributed to some surface state of, or some functional group present on, the particle surface, which is presently unknown.

Note that the zeta potential differences between the two ($\zeta_p - \zeta_s$), for the respective surface pretreatments, were the greatest for the hydrogen-plasma-treated substrate (+101.35 mV), sequentially followed by the pristine substrate (+58.61 mV), and the substrates pretreated by the hydrocarbon (+2.95 mV and -4.48 mV). Such tendencies coincided exactly with the order of the actual dispersed seed densities on the respective substrates, as described in relation to Figure 2 in the preceding paragraphs. This finding indicated that the dispersed seed density was dominated by the electrostatic interactions, as manifested in the zeta potential differences ($\zeta_p - \zeta_s$). The results agreed well with a previous report by Hees et al. [8] who also showed a strong correlation between nucleation density and zeta potentials.

Note the drastically increased strength of the negative zeta potential of the $^*SiO_2$/Si substrate, relative to that of the SiO_2/Si substrate. This is clearly attributed to the polarity of the Si-OH termination on the $^*SiO_2$ surface. It has been reported that surface silanol groups on a fused silica surface undergo protolysis so that the OH^- ions adsorb on the surface. Schwer et al. [9] reported that the zeta potential of the fused silica substrate was negative in an aqueous as well as methanol-water solution for a wide-ranging pH of 3 – 11; for a 50 % methanol-water solution, the zeta potential of the fused silica was around -60 mV at a pH of 8 (see Figure 10 of the reference).

By contrast, note the drastically decreased strengths of the negative zeta potential of $^\dagger SiO_2$/Si. Furthermore, the polarity of the zeta potential of $^\ddagger SiO_2$/Si was even

Substrate	Zeta potentials [mV] measured using Monitor solution (Latex particle + 10 mM NaCl aqueous solution)			Zeta potentials [mV] measured using Seeding suspension (Nano diamond particle + Methanol)		
	Particle (ζ_P)	Substrate (ζ_S)	$\zeta_P - \zeta_S$	Particle (ζ_P)	Substrate (ζ_S)	$\zeta_P - \zeta_S$
SiO_2/Si	-1.50	-28.30	+26.80	+30.01	-28.60	+58.61
*SiO_2/Si	-5.23	-31.03	+25.80	+37.51	-63.84	+101.35
†SiO_2/Si	+1.02	-22.71	+23.73	+1.82	-1.13	+2.95
‡SiO_2/Si	+4.26	-21.63	+25.89	+10.37	+14.85	-4.48

Table. The zeta potentials measured for flat substrates before and after treatment, and for the nano diamond colloid particles in mutual contact. (Pristine SiO_2/Si, hydrogen-plasma-treated SiO_2/Si (*SiO_2/Si), hydrocarbon-plasma-treated SiO_2/Si (†SiO_2/Si) and hydrocarbon-thermal-treated SiO_2/Si (‡SiO_2/Si))

reversed (see Table 1). This strongly suggested that the polarity of the Si-CH_3 termination, induced by exposure to the hydrocarbon plasma or by the hydrocarbon thermal atmosphere (aforementioned in relation to Figure 6b), was opposite to that of the Si-OH termination. Indeed, Hozumi et al. [10] reported that the Si-CH_3 termination on the SiO_2-coated Si substrate surface shifted its negative zeta potential toward the positive direction by no less than around +20 mV (see Figure 2 of the reference) for a wide-ranging pH of 3 – 11 (Recall that the pH of the seeding solution in the present study was 7.5 – 8).

The polarity of the Si-CH_3 termination in our study was positive. It thus follows that the decreasing strength of the negative zeta potential of †SiO_2/Si, or even the reversed polarity of the zeta potential of ‡SiO_2/Si in our investigations, should be attributed to such positive polarity of the Si-CH_3 termination, as opposed to that of the Si-OH termination.

The magnitude of the positive zeta potentials of the nano diamond particle in the seeding suspension significantly increased for SiO_2/Si and *SiO_2/Si, relative to those for †SiO_2/Si or ‡SiO_2/Si (see Table 1). The origin of such behavior is not yet clear, although it must obviously relate to some electrostatic interaction between the two.

Nevertheless, this result is in good agreement with the enhanced dispersion of the seeds on the SiO_2/Si and *SiO_2/Si, apart from their enhanced seed dispersion density, as described in the preceding paragraphs in relation to the microstructures shown in the insets of Figure 2. Our findings are not surprising since electrostatic repulsion between individual colloid particles, and hence their dispersion, would increase with the zeta potential.

Ultrathin (< 30 nm) diamond film synthesis on SiO_2 substrates

Figure 7 shows the ultrathin UNCD film synthesized on a quartz substrate pretreated by hydrogen plasma prior to the seeding. The film was synthesized under the same deposition conditions shown in Table 1, with a deposition time as short as 10 min. The film was smooth, void-free, and well adherent. The thickness of the film was less than 30 nm, as illustrated in Figure 7a, the thinnest among the void-free UNCD films coated on SiO_2 substrate reported to date. Figure 7b shows the Raman spectra (λ = 514.5 nm) taken from the sample. Apart from the usual D and G band, extra peaks at 1138 cm^{-1}, 1332 cm^{-1} and 1482 cm^{-1}, were observed, which is typical of UNCD with a grain size below 10 nm.

Conclusions

The exposure of a SiO_2-coated Si wafer to hydrogen plasma, prior to ultrasonic seeding, drastically enhanced the density of the dispersed nano diamond seeds on its surface. Such drastic enhancement in the seeding density was attributed to the modification of the zeta potentials of the substrate surfaces due to the formation of the silanol group on the SiO_2 surface.

This not only increased the strength of the negative zeta potential of the substrate, but also favorably altered that of the nano diamond particles in the suspension, in contact with substrate. This consequently enhanced the electrostatic attraction of the nano diamond particles to the substrate, as well as their electrostatic dispersion on the surface. It eventually enabled a void-free ultrathin UNCD coating as thin as 30 nm on a SiO_2-coated Si wafer by DC-PACVD using hydrogen-rich gas chemistry.

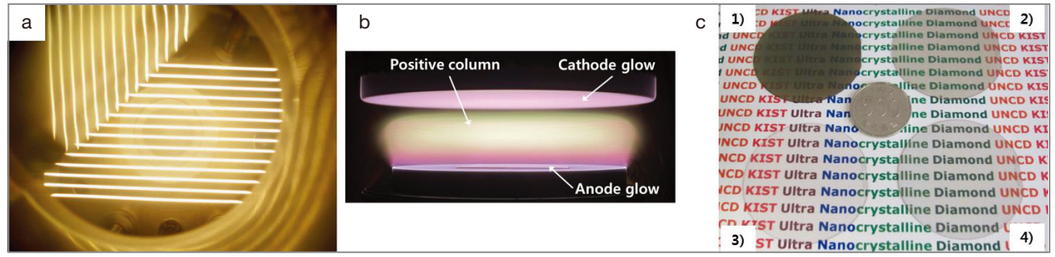

Figure 7. Photographs of (a) Hot-filament CVD, (b) Direct-current discharge, and (c) (U)NCD films on the SiO_2 coated sapphire wafer [1) 1 μm thick UNCD, 2) 100 nm thick UNCD, 3) 100 nm thick NCD, and 4) 1 μm thick NCD].

Note

This article and images are cited from “Synergistic Interaction between Substrate and Seed Particles in Ultrathin Ultrananocrystalline Diamond Film Nucleation on SiO_2 with Controlled Surface Termination” in *J Phys Chem* C. 2012; 116: 9180–9188.

References

[1] Gruen DM. *Annu Rev Mater Sci.* 1999; 29: 211-259.
[2] Auciello O, Sumant AV. *Diam Relat Mater.* 2010; 19: 699-718.
[3] Sekaric L, Parpia JM, Craighead HG, Feygelson T, Houston BH, Butler JE. *Appl Phys Lett.* 2002; 81: 4455-4457.
[4] Bergonzo P, Bongrain A, Scorsone E, Bendali A, Rousseau L, Lissorgues G. *Irbm.* 2011; 32: 91-94.
[5] Szunerits S, Ghodbane S, Niedziolka-Jonsson J, Galopin E, Klauser F. *J Phys Chem C.* 2010; 114: 3346-3353.
[6] Lee JS, Liu KS, Lin IN. *J Appl Phys.* 1997; 81: 486-491.
[7] Williams OA, Douheret O, Daenen M, Haenen K, Osawa E, Takahashi M. *Chem Phys Lett.* 2007; 445: 255-258.
[8] Hees J, Kriele A, Williams OA. *Chem Phys Lett.* 2011; 509: 12-15.
[9] Schwer C, Kenndler E. *Anal Chem.* 1991; 63: 1801-1807.
[10] Hozumi A, Sugimura H, Yokogawa Y, Kameyama T, Takai O. *Colloids Surf* A. 2001; 182: 257-261.

[Feature Articles]

Effect of Rare-Earth (RE) Element Doping in $Ce_{0.65}Zr_{0.25}RE_{0.1}O_2$ Nano-Crystalline Oxides Synthesized by a Glycine-Nitrate-Process: Structural Characterization and Catalytic Activity

D. Hari Prasad
High-Temperature Energy Materials Research Center
hari@kist.re.kr

Jong-Ho Lee
jongho@kist.re.kr

Introduction

Ceria-based materials displaying high oxygen mobility and oxygen storage capacity (OSC) have been extensively investigated due to their wide application in the field of catalysis and solid oxide fuel cells. The incorporation of zirconia in ceria forms ceria-zirconia (CZ) solid solutions which enhance thermal stability and maintain a high OSC even at high temperatures. These CZ solid solutions replace pure ceria, whose characteristics result in an inability to sustain the high degree of conversion and thermal resistance required for catalytic converters. The main features that contribute to the success of ceria-zirconia systems are high thermal resistance, higher reduction efficiency of the redox couple Ce^{4+}/Ce^{3+} and an excellent OSC as compared to pure ceria.

Rare earth (RE)-doped CZ oxides have been shown to improve OSC, redox properties and thermal resistance compared to CZ alone. Generally, for every two RE^{+3} ions that replace Ce^{+4}, one oxygen vacancy is needed to balance the charge. These oxygen vacancies increase the diffusion rate of oxygen, thereby improving the OSC. Furthermore, all RE elements have larger ionic radii than Zr^{+4} (0.87Å), thus providing more effective stabilization of a fluorite type structure compared to under-sized ones. In the present study, a glycine-nitrate-process (GNP) was employed to synthesize the $Ce_{0.65}Zr_{0.25}RE_{0.1}O_2$(RE= Pr, Tb, Sm, Gd, La, Nd and Eu) oxides since this is considered the most suitable method for producing fairly fine, homogenous and complex compositional metal oxide powders. GNP has many other advantages as well, such as relatively low cost, high energy efficiency, fast heating rates, short reaction times and high compositional homogeneity.

The aim of our work was to investigate the influence of RE dopants on the redox properties that affect the catalytic properties of a CZ system. The reducibility of the support material plays an important role in the suppression of carbon formation during reforming reactions. In order to screen the support materials that can be used for internal reforming in solid oxide fuel cell (SOFC) applications, we focused on the CO oxidation reaction as this reaction is mostly affected by the enhanced reducibility of the oxide solid solutions. The $Ce_{0.65}Zr_{0.25}RE_{0.1}O_2$ (RE= Pr, Tb, Sm, Gd, La, Nd and Eu) powders were successfully prepared by GNP.

From Figure 1a it can be observed that all the RE-doped samples showed a slight shift of the diffraction peaks toward a lower degree with respect to an un-doped sample. This phenomenon could be associated with the expansion of the crystal lattice, which is induced by the larger cation radius of the dopants relative to the Zr^{4+} (0.87Å) ions. According to Vegard's rule, a linear increase of the lattice constant can be expected due to the linear increase of the cation radius of the dopants (from Tb (1.04 Å) to La (1.16 Å)). As shown in Figure 1b, the increase of the lattice constant is not as linear as the increase of the cation radius of dopants. This may be due to factors like the existence of Pr and Tb in the mixed valance states and changes in Ce^{3+} concentration when doping with some RE elements.

As shown in Figure 2a, a slight shift in the Raman frequency and absence of peaks related to RE oxides is evidence of the formation of $Ce_{0.65}Zr_{0.25}RE_{0.1}O_2$ solid solutions, and thus corroborates the XRD results. Furthermore, the Raman spectra of the samples are very similar, with a predominant strong band at ~470cm^{-1} and a less prominent broad band at ~600cm^{-1}. The broad band at ~600cm^{-1} corresponds to the Longitudinal Optical (LO) mode of ceria, arising due to the relaxation of symmetry rules which can be linked to the oxygen vacancies in the ceria lattice. These vacancies can be ascribed to a localized substitution defect vibration. The broad band at ~600cm^{-1} can be de-convoluted into two peaks with a lower peak around ~560cm^{-1}. The band at 470cm^{-1} can be attributed to the F_{2g} Raman active mode of the fluorite-type lattice. It can further be observed in Figure 2 that with the increase of the ionic radius of RE elements in the $Ce_{0.65}Zr_{0.25}RE_{0.1}O_2$ solid solution, the F_{2g} band shifted slightly to lower values. The shift in the F_{2g} mode is attributed to a change in M-O vibration frequency after incorporation with the dopants, which account for the difference in the ionic radius.

Figure 2b shows the Raman spectra of $Ce_{0.65}Zr_{0.25}RE_{0.1}O_2$ (RE=Tb, Pr) samples. As compared to Figure 2a, the band at~465cm^{-1} is weaker and a broad stronger band

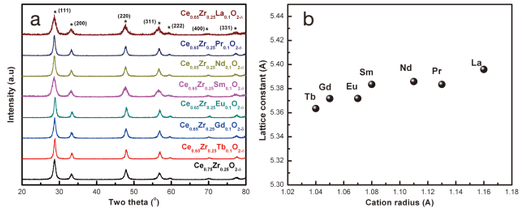

Figure 1. (a) XRD patterns of $Ce_{0.65}Zr_{0.25}RE_{0.1}O_{2-\delta}$ samples calcined at 600°C for 2h. (b) Lattice constant of the samples as a function of ionic radius of RE element.

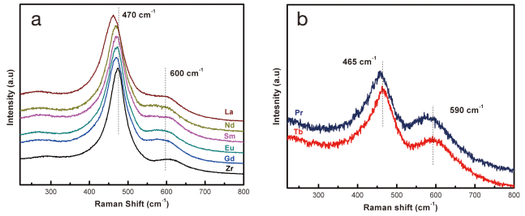

Figure 2. Raman spectra of $Ce_{0.65}Zr_{0.25}RE_{0.1}O_{2-\delta}$ samples calcined at 600°C for 2h: (a) RE= La, Nd, Sm, Eu, and Gd; (b) RE= Pr, Tb.

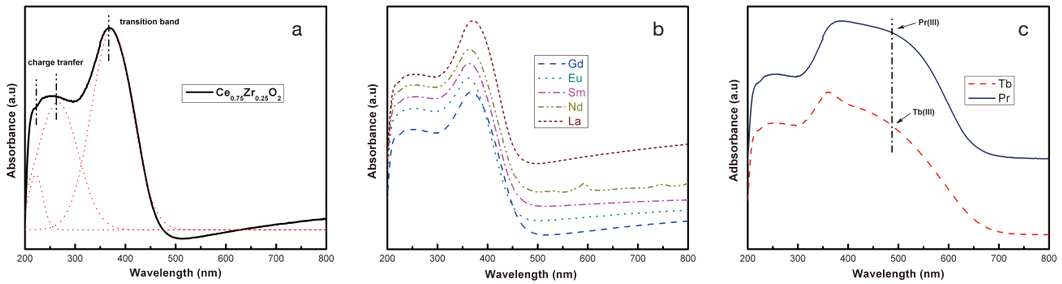

Figure 3. UV-vis DR spectra of (a) $Ce_{0.75}Zr_{0.25}O_{2-\delta}$ (b) $Ce_{0.65}Zr_{0.25}RE_{0.1}O_{2-\delta}$ samples (RE= La, Nd, Sm, Eu, and Gd) (c) $Ce_{0.65}Zr_{0.25}RE_{0.1}O_{2-\delta}$ (RE= Pr, Tb) samples calcined at 600°C.

at 590cm^{-1} is observable. Since Pr- and Tb-doped solid-solutions show quite intense absorption in the visible region, the laser line (in the present study, 514.23nm) cannot penetrate into the deep layers of the sample. This makes the band at 465cm^{-1} weaker and the band at 590cm^{-1} stronger. The band at 590cm^{-1} is the combination of both types of oxygen vacancies. It is well known that the RE ions, including Ce, easily form a series of non-stoichiometric oxides of the type REO_x (1.5=x=2). However, neither Pr nor Tb tends to crystallize in the dioxide or sesquioxide phases, preferring instead to form compounds with Pr_6O_{11} and Tb_4O_7. Thus, it can be expected that Pr- or Tb-doped samples should increase the oxygen vacancy concentration, a result which was observed in the present study.

Figure 3a shows the DRS spectrum of a $Ce_{0.75}Zr_{0.25}O_2$ sample in which the bands corresponding to charge transfer transitions are shifted to a lower wavelength and the interband transition to a higher wavelength. This shift in the interband transition could be due to the presence of Zr^{4+} ions in the system provoking a significant increase in the Ce^{3+} fraction on the surface, thereby increasing the charge-transfer gap between the O 2p and Ce 4f orbital. The DRS spectra of the $Ce_{0.65}Zr_{0.25}RE_{0.1}O_2$ (RE = La, Sm, Eu and Gd) samples are depicted in Figure 3b. It can also be seen that these samples showed a similar trend to the $Ce_{0.75}Zr_{0.25}O_2$ sample. Two other peaks at 590 and 745nm appeared in the $Ce_{0.65}Zr_{0.25}Nd_{0.1}O_2$ sample due to the presence of Nd in the sample. In addition to the three bands that were present in the rest of the samples, one more intense absorption band in the visible region (400-650nm) was observed in $Ce_{0.65}Zr_{0.25}Pr_{0.1}O_2$ and $Ce_{0.65}Zr_{0.25}Tb_{0.1}O_2$ samples (Figure 3c). The presence of this absorption band is associated with Pr^{3+} and Tb^{3+} ion transitions in their corresponding samples. The $Ce_{0.65}Zr_{0.25}Pr_{0.1}O_2$ sample showed that the interband transition peak moved to a higher wavelength (380nm) as compared to all other samples. This indicates that the Pr^{3+} ions in the system provoked a significant increase in the Ce^{3+} fraction on the surface, thereby increasing the charge-transfer gap between O 2p and Ce 4f orbitals as compared to all other samples.

The reducibility of $Ce_{0.65}Zr_{0.25}RE_{0.1}O_2$ samples calcined at 600°C was studied by using H_2-TPR experiments. The corresponding TPR profiles are shown in Figure 4. The $Ce_{0.75}Zr_{0.25}O_2$ sample exhibits a very broad reduction peak at 570°C along with a shoulder peak at lower temperatures (350-500ºC). It is hard to differentiate these two reduction peaks since they resemble a single reduction peak. An onset of H_2 consumption was observed around 320°C. Incorporation of small quantities of isovalent Zr^{4+} into a CeO_2 lattice enhanced its redox properties by creating structural defects with size effects and increasing the channel diameter for oxygen migration

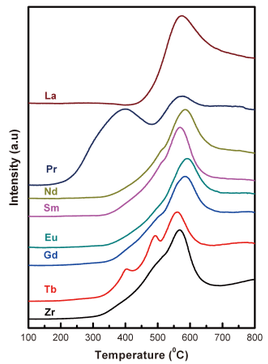

Figure 4.
H_2-TPR profiles of $Ce_{0.65}Zr_{0.25}RE_{0.1}O_{2-\delta}$ samples calcined at 600°C

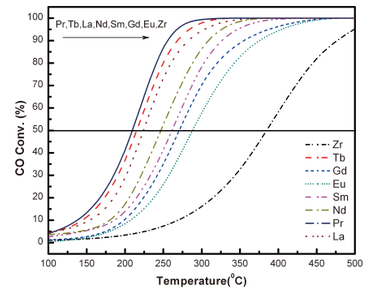

Figure 5.
Conversion of CO over $Ce_{0.65}Zr_{0.25}RE_{0.1}O_{2-\delta}$ samples calcined at 600°C as a function of reaction temperature.

in the lattice. This resulted in higher mobility of the lattice oxygen which led to one major low temperature peak in the TPR profile of ceria-zirconia solid solutions in contrast to ceria which had two main peaks. The higher mobility of the lattice oxygen caused reduction not just at the surface, but deeply extended into the bulk of the ceria-zirconia solid solution.

For $Ce_{0.65}Zr_{0.25}RE_{0.1}O_2$ samples, it can be observed in Figure 4 that the bulk reduction peak was around 550-570°C. The H_2-TPR profiles of $Ce_{0.65}Zr_{0.25}RE_{0.1}O_2$ (RE = Gd, Eu, Sm, Nd, La) samples also showed a shoulder peak at lower temperatures (350-500ºC) similar to the $Ce_{0.75}Zr_{0.25}O_2$ sample corresponding to surface reduction of the samples. It is quite interesting to see that the $Ce_{0.65}Zr_{0.25}Pr_{0.1}O_2$ sample showed two differentiable peaks instead of a very broad reduction peak which was observed for other $Ce_{0.65}Zr_{0.25}RE_{0.1}O_2$ samples. In this sample, the onset of H_2 consumption occurred at 180°C and the surface reduction peak was located around 375°C, a much lower temperature compared to other samples. The peak area of surface reduction was much higher than the peak area of bulk reduction, indicating that reducibility of this sample was much higher and can be reduced at lower temperatures than the other samples. Moreover, the addition of Pr induced ordered arrangements of vacancies, thereby creating a pathway for oxygen diffusion. This would promote oxygen ion diffusion from the bulk to the surface. As seen in Figure 4, the $Ce_{0.65}Zr_{0.25}Tb_{0.1}O_2$ sample also showed two reduction peaks corresponding to surface and bulk reduction peaks. It is interesting to see that the surface reduction peak split into multiple peaks. Generally, the TPR profile of $TbO_{1.75}$ shows reduction bands at 303, 667, 720°C. For this sample, the first two peaks at 400 and 490ºC can be attributed to the reduction of both Tb^{4+} and Ce^{4+} to Tb^{3+} and Ce^{3+}, respectively. The peak at 560ºC can be attributed to the bulk reduction of the sample. The reducibility of $Ce_{0.65}Zr_{0.25}RE_{0.1}O_2$ samples clearly shows that the Pr-doped CZO can be easily reduced at lower temperatures, indicating a higher mobility of surface oxygen at lower temperatures.

We next focused on the CO oxidation reaction which is most likely to be affected by the enhanced reducibility of the oxide solid solution. It is evident from Figure 5 that the $Ce_{0.65}Zr_{0.25}Pr_{0.1}O_2$ sample exhibited better activity in terms of total conversion as well as light-off temperature (50% conversion). The $Ce_{0.65}Zr_{0.25}Pr_{0.1}O_2$ sample exhibited 100% conversion at 300°C and light-off temperature of 208°C. The light-off temperatures of various catalysts followed the order: Pr>Tb>La>Nd>Sm>Gd>Eu>Zr. The oxidation of CO on ceria occurs via the Mars-van Krevelen redox type mechanism. In the absence of the oxygen feed, CO gets oxidized by consuming lattice oxygen and leaving the oxygen vacancy. In the presence of oxygen

feed, the lattice oxygen is replenished. Therefore, in the oxidation process, an oxygen vacancy is involved and acts as an active site for the dissociation of gaseous oxygen. Accordingly, in the oxidation process, vacancy plays an essential role. The lower reduction temperature and an increased ability to shift between Ce^{4+}/Ce^{3+} at much lower temperatures, as well as having high oxygen vacancies, are the keys for increased oxidation activity of the $Ce_{0.65}Zr_{0.25}Pr_{0.1}O_2$ sample. Development of these materials ($Ce_{0.65}Zr_{0.25}RE_{0.1}O_2$ (RE= Pr, Tb, La)) as anode supports for internal reforming SOFCs would be a topic of interest for future investigations.

Note

This article and images are cited from “Synergistic Interaction between Substrate and Seed Particles in Ultrathin Ultrananocrystalline Diamond Film Nucleation on SiO2 with Controlled Surface Termination” in *J Phys Chem C.* 2012; 116: 9180–9188.

References

[1] Hari Prasad D, Park SY, Ji HI, Kim HR, Son JW, Kim BK, Lee HW, Lee JH. *J Phys. Chem. C* 2012; 116: 3467-3476.

[2] Hari Prasad D, Park SY, Ji HI, Kim HR, Son JW, Kim BK, Lee HW, Lee JH. *Appl. Catal.* A 2012; 411-412: 160-169.

[3] Reddy BM, Gode T, Katta L. *J Phys. Chem. C* 2009; 113: 15882-15890.

[4] Hari Prasad D, Kim HR, Son JW, Kim BK, Lee HW, Lee JH. *Catal. Commun.* 2009; 10:1334-1338.

[**Technical Review**]

Rechargeable Batteries: Current Status and Future Perspectives

Soo Kim
Center for Energy Convergence Research
sookim@kist.re.kr

Won Chang Choi

Kyung Yoon Chung

Wonyoung Chang

Si Hyoung Oh

Introduction

A battery is an electrochemical device that converts chemical energy into electrical energy. Batteries can be classified as primary batteries or secondary batteries, based on reversibility. The reactions in secondary batteries are reversible so that they can be used for a number of cycles as “rechargeable batteries.”

The lead-acid battery was the first rechargeable battery invented by Gaston Planté in 1860. It consisted of two lead sheets separated by rubber strips rolled into a spiral [1]. Lead-acid batteries have been used mostly for automobile applications, because the batteries perform well at high current rates and cold temperatures. Alkaline batteries have also been widely used because they use alkaline KOH or NaOH electrolytes, which cause less degradation of the electrode materials as compared to the acid electrolytes [1].

Commercialized alkaline batteries can be used for a range of applications including portable home appliances, diesel engine starters, aircraft, and heavy-duty industrial equipment. Some examples of alkaline batteries include nickel-cadmium batteries, nickel-iron batteries, silver-zinc batteries, and nickel-zinc batteries. In the 1980’s, the nickel metal hydride (Ni-MH) battery was developed, replacing the toxic cadmium electrode with a hydrogen-absorbing alloy. Ni-MH batteries do not suffer from memory effects and offer two-to-three-times higher capacities than nickel-cadmium batteries (Figure 1).

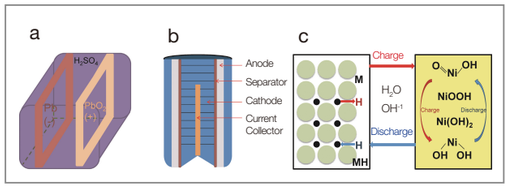

Figure 1. Various types of rechargeable batteries: (a) lead-acid battery; (b) alkaline battery; and (c) Ni-MH battery.

Background

Lithium ion batteries

Lithium ion batteries have been used with great success in the portable electronics market. The layered $LiCoO_2$ used as the cathode material in commercial lithium ion batteries enables the cells to achieve high energy densities. However, increasing interest in lithium ion batteries for applications in electric vehicles (EVs) and hybrid electric vehicles (HEVs) has necessitated alternative cathode materials due to the high cost, toxicity, and limited power capability of $LiCoO_2$ cathode materials. The lithium ion battery is composed of a cathode, anode, electrolyte, and separator. When the battery is charged, the lithium ions in the cathode material migrate through the separator to the anode with the flow of charging current and the external circuit, as shown in Figure 2.

During discharge, the lithium ions in the anode reverse their course and migrate to the cathode with the flow of discharging current through the external circuit. In order to achieve superior performance in lithium ion cells, cathode and anode materials should support a high degree of lithium insertion/extraction to maximize energy density. Also, the cathode material should have a low lithium chemical potential and the anode material should have a high lithium chemical potential to maximize cell voltage, and thus, energy density.

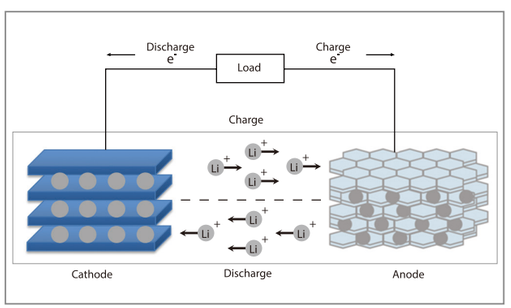

Figure 2. Schematic of lithium-ion battery operation.

In addition, voltage change in the cathode and anode materials during the charge-discharge process should be small. Finally, the lithium diffusion coefficient should be large for high-rate charge-discharge performance.

Layered structure

Layered $LiCoO_2$ is the most common cathode material found in commercial lithium ion batteries (Figure 3b). However, because of issues associated with the safety, cost, and toxicity of the cobalt, the development of alternate cathodes has been initiated during the past few decades. Many cathode candidates with different compositions, transition metals, or crystal structures have been extensively investigated. These include layered $LiNiO_2$ [2], $LiNi_{1-y}M_yO_2$ (M = Mn, Co, Al, etc.) [3–10], olivine $LiFePO_4$ [11–12], and spinel $LiMn_2O_4$ [13–14].

Layered structures are based on the general formula $LiMO_2$ (M = Mn, Co, Ni, Al, etc.) in which Li^+ and M^{3+} ions occupy the octahedral sites in the alternate (111) planes of the rocksalt lattice formed by a cubic close packing of oxide ions. A two-dimensional layered crystal structure is formed due to the large ionic radius and charge differences between the Li^+ and M^{3+} ions, resulting in a trigonal symmetry with the space group group $R\bar{3}m$. However, cation disorder between the Li^+ and M^{3+} layers often tends to occur as the size and charge differences decrease [15]. Layered $LiCoO_2$ has well-defined two-dimensional Li^+ ion pathways due to the large difference in ionic radius between Li^+ and Co^{3+} ions and good electronic conductivity from a direct Co-Co interaction in the edge-shared CoO_6 octahedra. Layered $LiCoO_2$ has been widely used in commercial lithium ion batteries mainly because it is easy to synthesize, with a reasonable capacity of ~140 mAh g^{-1}.

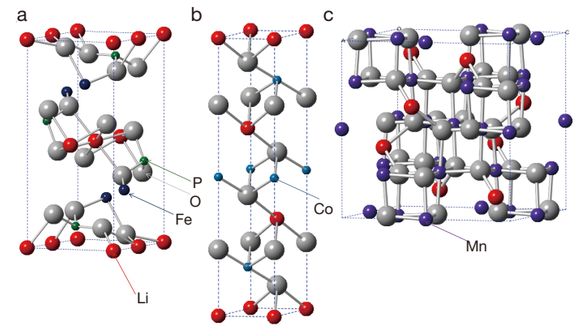

Figure 3. Structure of: (a) olivine $LiFePO_4$; (b) layered $LiCoO_2$; and (c) spinel $LiMn_2O_4$.

However, $LiCoO_2$ has some definite disadvantages as regards toxicity, cost, and chemical instability [16–21]. Layered $LiNiO_2$, which has the same structure as $LiCoO_2$, has been widely studied because it delivers a higher capacity: ~200 mAhg-1. Since the location of the $Ni^{3+/4+}$:e_g band is above the O^{2-}:2p band, lithium extraction does not cause a significant removal of electrons from the O^{2-}:2p band, and thus provides a greater utilization of lithium ions in $LiNiO_2$ [19, 22]. However, $LiNiO_2$ is difficult to synthesize, releases oxygen at elevated temperatures, and shows severe capacity fading. To improve cycle performance and resolve the safety problems of $LiNiO_2$, cation-substituted $LiNi_{1-y}M_yO_2$ (M = Mn, Co, Al) has also been intensively studied [3–10].

Olivine structure

Iron-containing compounds including FeOCl [23], $FePS_3$ [24], $KFeS_2$ [25], and FeS_2 [26] have been investigated as cathode materials because of the low cost and non-toxicity of iron. Among these compounds, the olivine $LiFePO_4$ has a theoretical capacity of ~170 mAh g^{-1}, operating at 3.4 V with excellent thermal stability [11] (Figure 3a). However, the olivine structure suffers from low electronic conductivity. To overcome this limitation, carbon or conducting polymer coating on the surface of the electrode materials and preparation of the powder in nanocrystalline form have been adopted [27–29].

Spinel structure

Electrochemical charging/discharging of spinel $LiMn_2O_4$ was first reported by Thackeray *et al.* [13] (Figure 3c). Since then, spinel $LiMn_2O_4$ containing inexpensive and environmentally benign Mn has been studied extensively as an alternate cathode material for lithium ion batteries. However, spinel $LiMn_2O_4$ suffers from severe capacity fade, especially at elevated temperatures, and delivers a slightly lower capacity around 120 mAh g^{-1}. Despite these problems, the inexpensive, nontoxic, and thermally stable $LiMn_2O_4$ has been very appealing for electric vehicle applications.

Anode materials

Carbon materials have been used as the anode material in commercial lithium-ion batteries because of their abundance, light weight, and safety compared to lithium metal. However, carbon shows a significant irreversible capacity loss in its initial cycles.

This irreversible capacity in the first cycle is generally attributed to solid electrolyte interfacial (SEI) layer

formation and side reactions of LiC_6 [30]. In order to improve the electrochemical properties, investigations have been conducted into structural modifications, texture control, and surface modification by mild oxidation [31]. Other alternative anode materials such as $Li_4Ti_5O_{12}$ [32–33], SnO_2 [34], and metal alloys [35–38] have also been proposed. However, the higher potential of $Li_4Ti_5O_{12}$ at around 1.5 V vs. Li/Li^+, the significant irreversible capacity of SnO_2, and the huge volume change of metal alloys are major challenges to overcome in the process of replacing carbon materials. Recently, Sony has adopted tin-based nanoparticles as the anode in lithium ion cells, delivering a much higher volumetric energy density than using carbon alone as the anode [39].

Experimental

Preparation

Typically, the electrode materials for lithium ion batteries are prepared by a solid-state reaction at a high temperature, transforming them into a desired structure. By introducing partial substitution of other transition metals, it is necessary to prepare the electrode materials precursor with co-precipitation for $LiNi_xCo_yMn_zO_2$ electrode materials (Figure 4).

Other synthetic methods to prepare the electrode materials include, but are not limited to, sol-gel synthesis, the microwave method, mechanochemical process, hydrothermal synthesis, emulsion, and spray-pyrolysis.

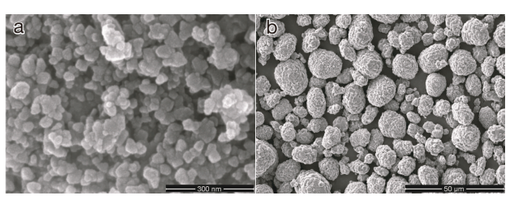

Figure 4. SEM images of electrode materials prepared by: (a) solid-state reaction; and (b) co-precipitation.

Electrochemical evaluations

The electrode material is usually mixed with carbon black and binder in 1-methyl-2-pyrrolidon to form slurry. The slurry is mixed in a homogenizer, coated onto aluminum foil using a doctor blade, and dried in an oven. The electrodes are rolled with a calendar press to obtain a desired packing density value. Finally, these electrodes are assembled in a dry room using lithium metal as the counter and reference electrodes with a layer of separator in a coin cell configuration (Figure 5).

Electrochemical performance

There are two important factors for rechargeable batteries: specific capacity and long-term cycleability. Specific capacity indicates the amount of lithium ions being charged and discharged from the chemical compounds. If the electrode material delivers a higher capacity, it means that more electricity can be generated for longer use. Another important factor is long-term cycle performance. Since rechargeable batteries can be used for a number of cycles, the stability of the structure during charge and discharge is a very important factor in determining whether the lithium-ion batteries can re-deliver the power consistently after being re-used a number of times. Electrochemical measurements to determine specific capacity and cycle performance are carried out in a multichannel battery tester (Figure 6).

Advanced *in situ* anaylsis

In situ x-ray analysis

In order to improve electrode materials and to further aid the development of new materials, it is important to understand the electrochemical reaction mechanism of the electrode materials during charge and discharge

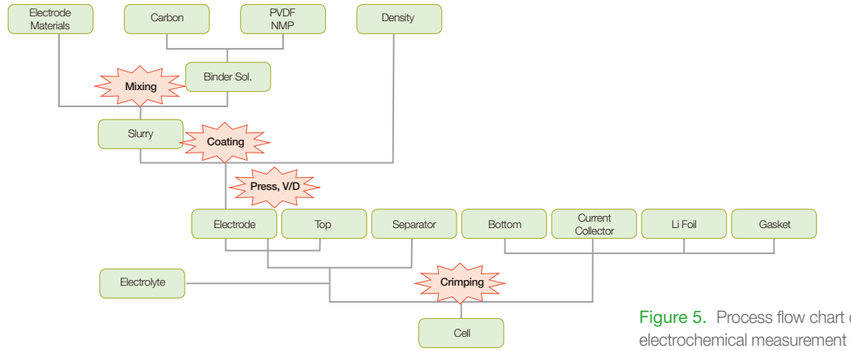

Figure 5. Process flow chart of coin cell fabrication for electrochemical measurement testing.

and to recognize their structural phase transitions at raised temperatures. Traditionally, *ex situ* x-ray diffraction was used to investigate the structural transition of the electrode materials. In this method, the cells including the electrode materials are charged or discharged to a desired voltage value, and then the cell is disassembled so that the active materials can be recovered to carry out the x-ray diffraction measurement.

However, this *ex situ* analysis does not describe the phase transition during the actual cell testing, but shows the structure indirectly after the end of the reaction. Thus, *in situ* x-ray measurement is now preferred in order to carefully examine the phase transition of the electrode materials during electrochemical testing.

One of the mostly commonly used x-ray analysis techniques involves synchrotron-based x-ray analysis of several types including (a) *in situ* time-resolved x-ray adsorption near edge structure spectroscopy, (b) XANES (x-ray absorption near edge structure), and (c) EXAFS (extended x-ray absorption fine structure). With *in situ* x-ray absorption spectroscopy, it is possible to determine the transition metal valence, site symmetry, covalent bond strength, atomic distance, and Debye-Waller factors.

In situ x-ray diffraction shows the structural changes, lattice parameters, and unit cell volume during electrochemical testing. Finally, time-resolved x-ray diffraction shows the structural changes that occur with increasing temperature up to 1000°C, stability of the electrode materials, and phase transitions of the precursors to the electrode materials during heat treatment. Modified coin cells are used for synchrotron-based *in situ* x-ray analysis (Figure 7).

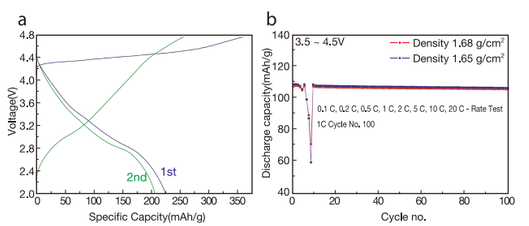

Figure 6. Electrochemical measurement: (a) capacity vs. voltage curves (Li_2MnO_3); and (b) rate and cycling tests ($LiMn_2O_4$).

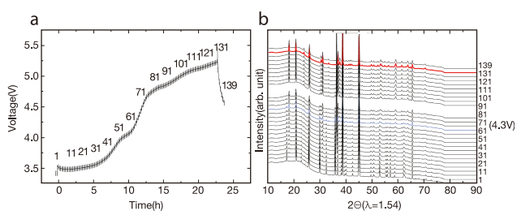

Figure 7. (a) Charge curve of $LiFePO_4$ up to 5.5 V at C/20 rate; and (b) corresponding *in situ* XRD patterns.

Transmission electronic microscopy

Material properties are highly dependent upon their fine-structures, such as the types of atoms and their positions. In the case of nano-size materials in particular, the addition or removal of atoms can change the electronic, mechanical, optical, or magnetic properties significantly. It is necessary to observe the position and order of atoms in fine-structures to predict the changes in material properties.

Intensive research efforts are on-going to develop nano-sized electrode materials for lithium ion batteries. Nano-sized electrode materials induce uniform electric fields within the particles, and the reaction does not solely occur at the bulk of the electrode materials in contrast to particles in ~μm scale. The materials have other advantages as well, such as the reduction of ionic diffusion length and a rapid reaction rate due to increased surface area. However, the reduction of particle size may cause the excessive formation of a solid electrolyte interface (SEI) film on the surface of the active materials, resulting in the dramatic decrease of charge/discharge efficiency during the formation cycle.

The dynamic nature of this nm scaled interface often makes it difficult to fully understand the fundamental reaction and degradation mechanism of the electrode materials . As a result, it is highly useful to investigate the relationships between the structure and properties on an atomic and nanoscale using high-resolution transmission electronic microscopy (TEM). Conventional spectroscopic techniques, such as x-ray and neutron diffractions, are powerful for investigating the average structural information through the entire sample, but are inadequate for exploring a local structure change with a high spatial resolution. Among many TEM-based analysis techniques, *in situ* TEM analysis is considered the most effective because it enables the observation of nanostructure growth [40, 41], solid-gas reaction in catalytic systems [42], materials phase transitions or deformation behaviors [43, 44], and particle nucleation and growth in solutions [45].

Although *ex situ* analysis based on electron beam imaging and spectroscopy has been widely used for probing the structural features of Li-ion battery systems, it does not allow full observation of the process during battery operation. Typically, there are two *in situ* TEM analysis techniques that can be used directly to research Li-ion battery materials.

First, *in situ* TEM analysis at varying temperatures can be used to observe the thermal stability and thermal decomposition mechanisms of various cathode and nanomaterials. This analysis ultimately provides valuable information about how to better design the thermally stable electrode materials for electric, plug-in hybrid electric vehicle (EV, PHEV, and HEV) applications. Although much attention has been paid to thermal stability at the charged state, the exact mechanism still remains uncertain.

Previous thermal abuse tolerance studies have reported that in a highly delithiated state, electrode materials can lose enough oxygen as temperatures increase to induce structural phase transitions, thereby leading to dangerous and catastrophic failures [46–50]. Our preliminary *in situ* heating experiment with a high-resolution environmental TEM (FEI Titan 80/300 ETEM) clearly showed the morphological and structural changes of the charged $Li_{1-x}Ni_{0.8}Co_{0.15}Al_{0.05}O_2$ ($0.5 \leq x \leq 0.9$) cathode material during heating at temperatures ranging from room temperature to approximately 400°C. A second type of *in situ* TEM analysis can be conducted for electrochemical testing.

The goal of the electrochemical *in situ* TEM is to allow real-time observation with high spatial resolution during electrochemical reactions and ultimately to describe the specific mechanisms of electrochemical reaction and degradation in *nm* scale. The first paper on *in situ* TEM observation during battery operation was reported by J.Y. Huang *et al*. in 2010 [51]. They reported the *in situ* observation of the lithiation of a SnO_2 nanowire during electrochemical charging and related electrochemical reaction-induced microstructural changes. However, this

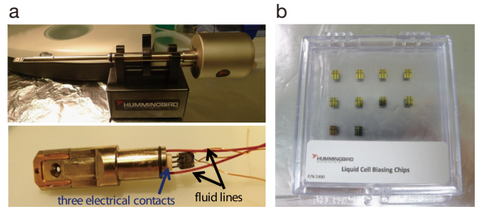

Figure 8. (a) Liquid electrochemical cell holder and (b) biasing chip. A liquid cell is placed at the tip of a liquid flow TEM holder. The TEM holder has three built-in contacts for biasing.

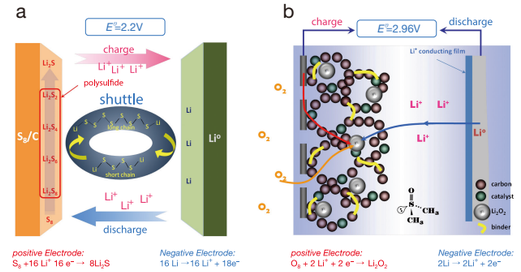

Figure 9. Schematic diagrams for (a) Li-sulfur and (b) Li-air batteries.

study as well as subsequent ones examined lithium ion batteries which operate with ionic liquid based electrolytes exhibiting negligible vapor pressure, making them suitable for the high vacuum system of TEM.

To observe complete solid-liquid interactions between the electrode/electrolyte interface under more realistic conditions, improvement involving liquid electrochemical cell holders and biasing chips are necessary. Figure 8 shows an example of a liquid cell holder for *in situ* TEM observation. The cell holder is made by stacking two prepatterned silicon microchips, one on each side of a SiN membrane.

The future: advanced llthium ion batteries

Li-sulfur and Li-air batteries

The advent of hybrid electric vehicles (HEVs) and load–leveling for intermittent energy sources have sparked a pressing demand for large-scale energy storage systems with a higher energy density and lower cost than conventional Li-ion battery systems, which utilize the intercalation of Li ions into host materials such as graphite and layered oxide. People now turn to more advanced systems such as Li-sulfur or Li-air batteries (Figure 9) which can produce, in principle, a ten-fold higher energy density than a $LiCoO_2$/graphite system and can potentially be manufactured more cheaply [52–54].

These systems utilize the conversion reactions of sulfur or oxygen molecules with Li ions on the positive electrode ($16Li + S_8 \rightarrow Li_2S$, $E^o = 2.2$ V for a Li-sulfur battery; $2Li + O_2 \rightarrow Li_2O_2$, $E^o = 2.96$ V for a Li-air battery). The theoretical energy density from these conversion reactions amounts to 2,500 Wh kg^{-1} for a Li-sulfur battery and 3,500 Wh kg^{-1} for a Li-air battery compared to just 400 Wh kg^{-1} for a $LiCoO_2$/graphite system. The Li-air battery has an additional advantage in terms of gravimetric energy density since oxygen is not loaded on the cathode initially, but is provided by air present during the discharge reaction.

This means that the weight of the Li-air battery system increases continuously as it is discharged. Many of the technological challenges which initially limited the use of these systems have been resolved, thanks to intensive on-going world-wide research in these areas [53–54]. Although these two battery systems have some features in common such as nearly identical discharge capacities and the use of metallic lithium on the negative electrode, the detailed reaction mechanisms and technological challenges they present are very different.

The safety problems associated with the formation of dendrite on the lithium anode are still one of the major hurdles to overcome and currently block commercialization potential. However, in the last several decades, there

has been progress in mitigating this issue by using such technologies as an alloying system, electrolyte additives, and protection by an Li+ conducting- membrane.

The principal drawbacks associated with Li-sulfur batteries arise from the low conductivity of sulfur (~10^{-15} S cm^{-1}) and the dissolution of intermediate reaction species (lithium polysulfides, Li_2S_n, $4 < n < 6$) into electrolytes, which lead to low discharge capacity, low rate capability, low coulombic efficiency and low cycling stability. The formation of nano-scale sulfur particles in a porous conductive matrix is a common approach to enhance the low electrochemical activity of sulfur, and improved capacity was reported by the imbibition of sulfur melt into a mesoporous carbon network. Many porous networks or encapsulating agents made of mesoporous or hollow carbon, CNT, MOF and conductive polymer have been applied to prepare various carbon/sulfur nano-composites with high discharge capacities and good rate capabilities [55–57].

Figure 10a shows a representative electrochemical performance with such a cathode. On the other hand, long-chain (higher order) lithium polysulfides such as Li_2S_8 and Li_2S_6 are generated on the cathode as an intermediate species during the charge or discharge process and readily dissolve in common electrolyte systems. This causes a shuttle reaction, especially during the charge process, between the cathode and anode. Many attempts have been made to control this phenomenon, including installing a physical barrier on the surface of the carbon/sulfur nano-composite, adding adsorbents with high surface areas on the cathode for surface adsorption, and substituting polymer electrolyte to slow the diffusion of bulky polysulfide to control the dissolution [58–60]. In another approach, lithium polysulfide is allowed to dissolve, but a Li^+-selective film is prepared on the anode surface to hinder the reduction of polysulfide to a shorter chain suppressing the shuttle reaction [61].

The first study of Li-air batteries was reported in 1996 by K. M Abraham *et al.* who proved that this type of rechargeable battery could be successfully constructed, and proposed a reaction mechanism based on the discharge product, although many features of the oxygen reduction reaction in aprotic solvent had been studied much earlier [62]. In the early stages of development, research was primary focused on preparing an electrically conductive porous carbon network with a high surface area. These properties are desirable for holding insoluble Li_2O_2 discharge product and catalysts to promote oxygen reduction reaction (ORR) and oxygen evolution reaction (OER), which occur from the decomposition of discharge product, assuming the reaction on the positive electrode is ideal. However, it became clear that ORR processes on the cathode in most battery electrolytes are not ideal, and in fact, are related to the decomposition of the electrolyte system [63, 64]. After thorough investigation, it has been found that the ORR process in most organic solvents generates lithium superoxide radicals, LiO_2.

The high reactivity of these lithium superoxide radicals causes nucleophilic reactions with carbons from many common electrolyte systems as well as structural components of the cell. A systematic study of various synthetic or commercially available electrolyte systems indicates that some types of ethereal solvents, e.g., dimethylformamide and dimethyl sulfoxide, show better stability than organic carbonates although an ideal electrolyte system that satisfies many criteria of the Li-air system has yet to be found [65-67].

Aside from the intriguing electrolyte problem, the decomposition of the ideal discharge product, Li_2O_2 is another major challenge.

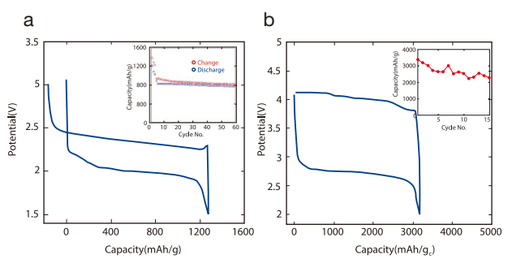

Figure 10. Discharge-charge curves and capacity retentions (inset) for: (a) Li-sulfur battery with carbon/sulfur nano-composite cathode and (b) Li-air battery with a metal oxide catalyst.

Lithium peroxide is usually found in submicron size on the electrode surface as it is formed from the disproportionation of the soluble lithium superoxide during the discharge process. The insulating and immobile character of this compound demands a highly efficient catalyst and a homogeneous distribution of the nano-sized catalyst throughout the cathode. As seen in Figure 10b, even with a state-of-the-art metal oxide catalyst, the discharge-charge curve still exhibits a significant overpotential during the charge process.

Conclusions

Li-sulfur and Li-air batteries have great potential as viable options for large-scale energy storage systems since they have high energy density and are manufactured at a relatively low cost. As regards the Li-sulfur battery, many technological issues related to its low conductivity and polysulfide dissolution have been successfully solved thanks to recent advances in this area, and commercial products are expected in the near future. On the other hand, intensive fundamental research is still required on the Li-air battery, specifically related to the activity of superoxide radicals and the catalysis for Li_2O_2 decomposition.

References

[1] Linden D, Reddy TB. Editors, *Handbook of Batteries,* 3rd Ed. McGraw-Hill, New York. 2001.
[2] Dahn JR, Von Sacken U, Michal CA. *Solid State Ionics.* 1990; 44: 87.
[3] Gummow RJ, Thackeray MM. *Solid State Ionics.* 1992; 53-56: 681.
[4] Rossen E, Jones CW, Dahn JR. *Solid State Ionics.* 1992; 57: 311.
[5] Delmas C, Saadoune I, Rougier A. *J. Power Sources.* 1993; 43-44: 595.
[6] Ohzuku T, Ueda A, Nagayama M, Iwakoshi Y, Komori H. *Electochem. Acta.* 1993; 38:1159.
[7] Zhecheva E, Stoyanova R. *Solid State Ionics.* 1993; 66: 143.
[8] Yoshio M, Noguchi H, Itoh J, Okada M, Mouri Y. *J. Power Sources.* 2000; 90: 176.
[9] Ohzuku T, Makimura Y. *Chem. Lett.* 2001; 8: 744.
[10] Ohzuku T and Makimura Y, *Chem. Lett.* 2001; 7: 642.
[11] Padhi AK, Nanjundaswamy KS, Goodenough JB. *J. Electrochem. Soc.* 1997; 144: 1188.
[12] Yamada A, Chung SC, Hinokuma K. *J. Electrochem. Soc.* 2001; 148: A224.
[13] Thackery MM, David WIF, Bruce PG, Goodenough JB. *Mater. Res. Bull.* 1983; 18: 461.
[14] Jang DH, Shin YJ, Oh SM. *J. Electrochem. Soc.* 1996; 143: 2204.
[15] Wu EJ, Tepesch PD, Ceder G. *Philosophical Magazine B.* 1998; 77: 1039.
[16] Reimers JN, Dahn JR. *J. Electrochem. Soc.* 1992; 131: 2091.
[17] Amatucci GG, Tarascon JM, Klein LC. *J. Electrochem. Soc.* 1996; 143: 1114.
[18] Chebiam RV, Kannan AM, Prado F, Manthiram A. *Electrochem. Commun.* 2001; 3: 624.
[19] Chebiam RV, Prado F, Manthiram A. *Chem. Mater.* 2001; 13: 2951.
[20] Choi J, Manthiram A. *J. Electrochem. Soc.* 2005; 152: A1714.
[21] Choi J, Manthiram A. *Solid State Ionics.* 2005; 176: 2251.
[22] Morales J, Perez-Vincente C, Tirado JL. *Mat. Res. Bull.* 1990; 25: 623.
[23] Whittingham MS. U. S. Patent 4049887. 1996.
[24] Thompson AH, Whittingham MS. *Mater. Res. Bull.* 1977; 12: 741.
[25] Jacobson AJ, Whittingham MS. U. S. Patent 4143213. 1978.
[26] Whittingham MS. Prog. *Solid State Chem.* 1978; 12: 41.
[27] Ravet N, Goodenough JB, Besner S, Simoneau M, Hovington P, Armand M. *Electrochem. Soc. Abstr.* 1999; 99-2: 127.
[28] Ravet N, Besner S, Simoneau M, Vallee A, Armand M, Magnan JF. European Patent 1049182A2. 2000.

[29] Huang H, Yin SC, Nazar LF, Electrochem. *Solid State Lett.* 2001; 4: A170.
[30] Besenhard JO. Editor, *Handbook of Battery Materials,* Wiley-VCH, Weinheim. 1999.
[31] Fu LJ, Liu H, Li C, Wu YP, Rahm E , Holze R, Wu HQ. *Solid State Sciences.* 2006; 8: 113.
[32] Murphy DW, Greenblatt M, Zahurak SM, Cava RJ, Waszczak JV, Hull GW, Hutton RS. *Rev. Chim. Miner.* 1982; 19: 441.
[33] Prosini PP, Mancini R, Petrucci L, Contini V, Villano P. *Solid State Ionics.* 2001; 144: 185.
[34] Morimoto H, Nakai M, Tatsumisago M, Minami T. *J. Electrochem. Soc.* 1999; 146: 3970.
[35] Yao NP, Heredy LA, Saunders RC. *J. Electrochem.* Soc. 1971; 118: 1039.
[36] Wen CJ, Boukamp BA, Huggins RA, Weppener W. *J. Electrochem. Soc.* 1979; 126: 2258.
[37] Wen CJ, Huggins RA. *J. Solid State Chem.* 1981; 37: 271.
[38] Zhang JJ, Xia YY. *J. Electrochem. Soc.* 2006; 153: A1466.
[39] http://www.physorg.com/news3061.html
[40] Harutyunyan AR, Chen GG, Paronyan TM, Pigos EM, Kuznetsov OA, Hewaparakrama K, Kim SM, Zakharov D, Stach EA, Sumanasekera GU. *Science.* 2009; 326: 116.
[41] Kim BJ, Tersoff J, Kodambaka S, Reuter MC, Stach EA, Ross FM. *Science.* 2008; 322: 1070.
[42] Hansen PL, Wagner JB, Helveg S, Rostrup-Nielsen JR, Clausen BS, Topsoe H. *Science.* 2002; 295: 2053.
[43] Shan ZW, Mishra RK, Asif SAS, Warren OL, Minor AM. *Nat. Mater.* 2008; 7: 115.
[44] Minor AM, Asif SAS, Shan ZW, Stach EA, Cyrankowski E, Wyrobek TJ, Warren OL. *Nat. Mater.* 2006; 5: 697.
[45] Zheng HM, Simith RK, Jun YW, Kisielowski C, Dahmen U, Alivisatos AP. *Science.* 2009; 324: 1309.
[46] Belharouak I, Lu WQ, Vissers D, Amine K. *Electrochem. Commun.* 2006; 8: 329.
[47] Belharouak I, Vissers D, Amine K. *J. Electrochem. Soc.* 2006; 153: A2030.
[48] Wang YD, Jiang JW, Dahn JR. *Electrochem. Commun.* 2007; 9: 2534.
[49] Belharouak I, Lu WQ, Liu J, Vissers D, Amine K. *J. Power Sources.* 2007; 174: 905.
[50] Wu L, Nam KW, Wang X, Zhou Y, Zheng JC, Yang XQ, Zhu I. *Chem. Mater.* 2011; 23: 3953.
[51] Huang JY, Zhong L, Wang CM, Sullivan JP, Xu W, Zhang LQ, Mao SX, Hudak NS, Liu XH, Subramanian A, Fan H, Qi L, Kushima A, Li *J. Science.* 2010; 330: 1515.
[52] Bruce PG, Freunberger SA, Hardwick LJ, Tarascon JM. *Nature Mater.* 2012; 11: 19.
[53] Ji X, Nazar LF. *J. Mater. Chem.* 2010; 20: 9821.
[54] Girishkumar G, McCloskey B, Luntz AC, Swanson S, Wilcke W. *J. Phys. Chem. Lett.* 2010; 1: 2193.
[55] Ji X, Lee KT, Nazar LF. *Nature Mater.* 2009; 8: 500.
[56] Jayaprakash N, Shen J, Moganty SS, Corona A, Archer A. *Angew. Chem. Int.* Ed. 2011; 50: 5904.
[57] Wang H, Yang Y, Liang Y, Robinson JT, Li Y, Jackson A, Cui Y, Dai H. *Nano Lett.* 2011; 11: 2644.
[58] Xi J, Evers S, Black R, and Nazar LF, *Nat. Commun.* 2011; 2 :325.
[59] Lee KT, Black R, Yim T, Ji X, Nazar LF, Adv. *Energy. Mater.* 2012; 10: 6
[60] Demir-Cakan R, Morcrette M, Nouar F, Davoisne C, Devic T, Gonbeau D, Dominko R, Serre C, Férey C, Tarascon JM. *J. Am. Chem. Soc.* 2011; 133: 16154.
[61] Aurbach D, Pollak E, Elazari R, Salitra G, Kelley CS, Affinito J. *J. Electrochem. Soc.* 2009; 156: A694.
[62] Abraham KM, Jiang Z. *J. Electrochem. Soc.* 1996; 143: 1.
[63] Laoire CO, Mukerjee S, Abraham KM, Plichta EJ, Hendrickson MA. *J. Phys. Chem. C.* 2009; 113: 20127.
[64] Freunberger SA, Chen Y, Peng Z, Griffin JM, Hardwick LJ, Bardé F, Novák P, Bruce PG. *J. Am. Chem. Soc.* 2011; 133: 8040.
[65] Oh SH, Yim T, Pomerantseva E, Nazar LF. *Electrochem. Solid-State Lett.* 2011; 14: A185.
[66] Chen Y, Freunberger SA, Peng Z, Bardé F, Bruce PG, *J. Am. Chem. Soc.* 2012; 134: 7952.
[67] Peng Z, Freunberger SA, Chen Y, Bruce PG. *Science.* 2012; 337: 563.

[**Feature Articles**]

Synthesis of Ionic Cellulose

Huyen Thanh Vo
Clean Energy Research Center
611007@kist.re.kr

Hyunjoo Lee
hjlee@kist.re.kr

Introduction

Cellulose, a linear 1,4-β-glucan polymer, is the most abundant organic compound on earth. About 33% of all plant matter is cellulose, and certain common plants have a particularly high content: cotton fiber (90%), wood (40-50%) and dried hemp (75%). For thousands of years, cellulose has served mankind as an indispensable material for clothing and housing and has contributed significantly to human culture since Egyptian papyrus was first introduced. Nevertheless, the use of this polymer as a chemical raw material began just 150 years ago with the discovery of the first cellulose derivatives. Today, more than 5 million tons of cellulose are produced annually.

Like other biomaterials, cellulose has poor solubility in water and organic solvent due to its strong inter- and intra-molecular hydrogen bonding. As a result, poisonous and/or explosive solvents such as CS_2 and NMMO are still used for the manufacture of cellulose-based artificial fibers such as rayon.

Cellulose possesses three hydroxyl groups at the C_2, C_3, and C_6 positions which are susceptible to chemical reactions such as esterification and etherification. Among the various chemical transformations of cellulose that involve these hydroxyl groups, the synthesis of water-soluble cellulose derivatives through the esterification reaction of cellulose with phosphorous-based acid has recently received considerable attention in the scientific community where research has identified many applications for the resulting phosphorous-containing cellulose derivatives as value-added materials in a variety of biomedical fields. The phosphorylation of cellulose has been conducted by treating cellulose with phosphorous-containing acids including H_3PO_4, P_2O_5, polyphosphorous acid $H_4P_2O_7$ or $H_5P_3O_{10}$, and chloride-based compounds such as PCl_3 or $POCl_3$. However, the products obtained from these reactions are often water-insoluble because these reactions occur in a heterogeneous process resulting in insufficient phosphorylation.

Ionic liquids (ILs) are now becoming an area of focus in various fields of

chemistry due to their unique properties such as negligible vapor pressures, wide liquid temperature ranges, and highly polar yet non-coordinating characteristics. In lignocellulosic biomass dissolution, some ionic liquids were found to have good solvating power not only for cellulose but also other biomacromolecules such as silk fibroin, lignin, starch, wool keratin, chitin/chitosane, soft wood and hard wood (Figure 1). The dissolution of cellulose in ILs depends on the ability of ILs to break strong inter- and intra-molecular hydrogen bonding in cellulose crystal structure. IL anion acts as a hydrogen bond donor and plays a key role in cellulose dissolution [1].

Recently, we found that simple dissolution of cellulose above 100℃ in IL of 1,3-dimethylimidazolium methyl phosphite ([DMIm][(MeO)(H)PO_2]) not only dissolves cellulose well but also induces the formation of phosphorylated cellulose. Synthesized phosphorous-containing ionic cellulose is highly soluble in water [2]. In this article, we introduce a method to synthesize water-soluble ionic cellulose and discuss its characterization.

Ionic cellulose synthesis

It is well established that cellulose can be dissolved in imidazolium and phosphonium-based ILs bearing a basic anion that is capable of interacting with the hydroxyl groups of cellulose. However, most investigations on ILs reported thus far have focused only on the degree of cellulose dissolution, not on structural modification. As the phosphorylation of cellulose by H_3PO_3 at an elevated temperature of 150°C is known to produce water-soluble phosphorylated cellulose, we anticipated that similar phosphorylation could take place by an IL bearing a phosphite anion. In this context, cellulose was reacted with [DMIm][(MeO)(H)PO_2] at 120°C for 1 h. The solution became transparent within 10 min, indicating that cellulose was completely dissolved in [DMIm][(MeO)(H)PO_2]. After 1 h of dissolution, the resulting transparent solution was cooled to room temperature, and water was then added to the solution to regenerate cellulose. As predicted, the solution remained transparent without producing any solid precipitates, suggesting the formation of a water-soluble

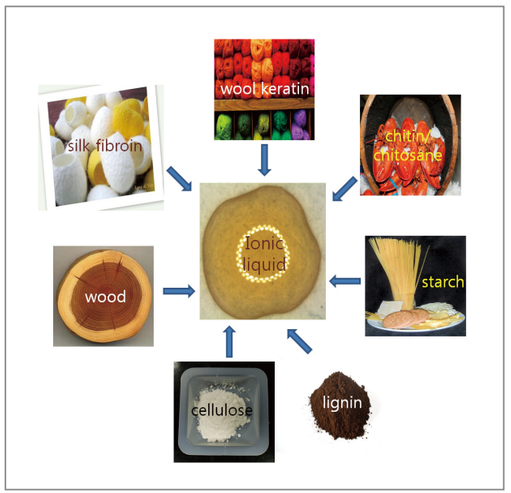

Figure 1. Lignocellulosic biomass can be dissolved in ionic liquids.

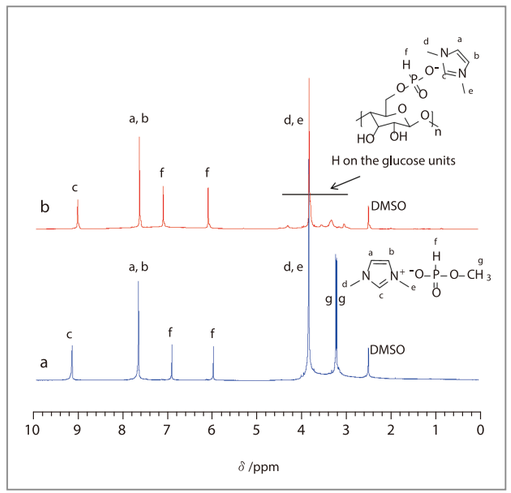

Figure 2. 1H NMR spectra of [DMIm][(MeO)(H)PO2] and regenerated cellulose in [D6]DMSO.: (a) [DMIm][(MeO)(H)PO2]., (b) Rregenerated cellulose after dissolution in [DMIm][(MeO)(H)PO2] at 120°C for 1 h.

cellulose derivative. Such a phenomenon has never been observed in the regeneration of cellulose dissolved in ILs.

In order to gain deeper insight into this phenomenon, we attempted to isolate the cellulose dissolved in [DMIm][(MeO)(H)PO_2] using acetonitrile as a precipitation solvent instead of water. The addition of acetonitrile into the solution of cellulose dissolved in [DMIm][(MeO)(H)PO_2] produced white precipitates, which were completely soluble in water. The characterization of the isolated solid product by ^{1}H NMR spectroscopy clearly revealed that the cellulose was phosphorylated upon dissolution in [DMIm][(MeO)(H)PO_2] (Figure 2).

From the presence of the characteristic peaks for the imidazolium moiety at 3.70, 7.21, and 8.44 ppm, and the doublet peak for the P-H bond in the 1H NMR spectrum of the solid product, it is obvious that the regenerated cellulose contained an imidazolium moiety and a phosphite group in a repeating glucose unit. The doublet peak corresponding to the methyl group of [DMIm][(MeO)(H)PO_2] at 3.32 and 3.35 ppm disappeared in the 1H NMR spectrum of the phosphorylated cellulose. This result strongly suggests that a hydroxyl group in the glucose unit was converted into a phosphite group by the interaction with methyl phosphite anion of [DMIm][(MeO)(H)PO_2] along with the concomitant loss of methanol, thereby resulting in the formation of dimethylimidazolium cellulose phosphite (Figure 3) .

The phosphorylation of cellulose by [DMIm][(MeO)(H)PO_2] was further investigated at various temperatures and times. The dissolution of cellulose in [DMIm][(MeO)(H)PO_2] was conducted at 120, 140, and 160°C, for 1 and 3 hour reaction times at the specified temperatures. As shown in Figure 4, the degree of phosphorylation (DS_P) was strongly affected by the dissolution temperature. Below the temperature of 100°C, the DSP value was negligible. However, with an increase of temperature over 120°C, DS_P values increased rapidly and reached 1.3 at 160°C for a 3 hour reaction. The DSP was also influenced by the dissolution time, but the effect was much more

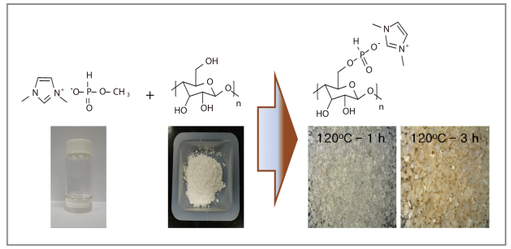

Figure 3. The phosphorylation of cellulose with [DMIm][(MeO)(H)PO_2].

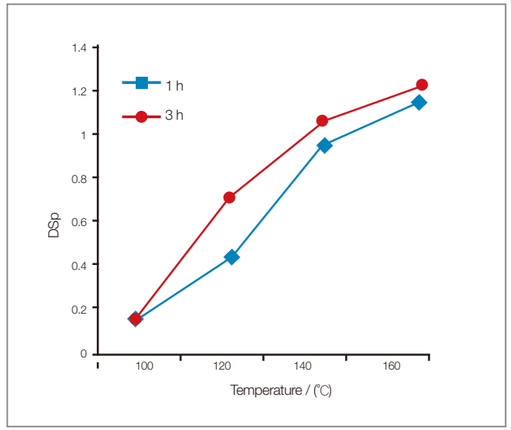

Figure 4. The relationship between phosphorous degree of substitution (DSP) and reaction temperature and time.

pronounced at lower reaction temperatures.

That is, at 120°C, the increase of the reaction time from 1 h to 3 h resulted in the DS_P value being raised up to 75%. In contrast, at 160°C, only a 7.4% increase of DS_P was attained with extension of the reaction time from 1 h to 3 h. The incorporation of [DMIm][(MeO)(H)PO_2] into cellulose and the dependence of the DS_P on temperature were further supported by the FT-IR spectra of A1, B1, and C1, shown in Figure 5. Upon the dissolution of cellulose in [DMIm][(MeO)(H)PO_2], new absorption bands appeared at 2351 and 1576 cm^{-1}, which corresponded to the P-H stretching frequency of phosphite and the C=N stretching frequency of the imidazolium ring,

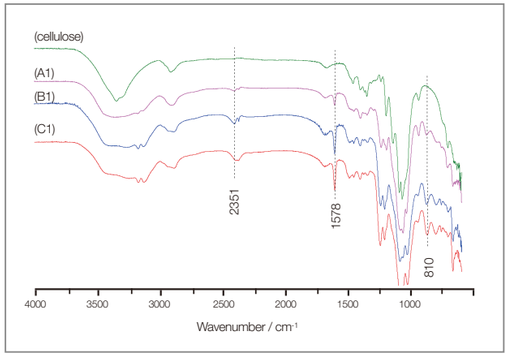

Figure 5. FT-IR spectra of cellulose and phosphorylated celluloses, A1, B1, and C1.

respectively [2]. A new band at 810 cm^{-1} corresponding to the P–O–C bond showed the interaction between the phosphite groups and glucose units. The intensities of these absorption bands increased with an increase of dissolution temperature.

The most interesting feature observed in the phosphorylation of cellulose using [DMIm][(MeO)(H)PO_2] is that the resulting phosphorylated cellulose derivatives were completely soluble in water even at a DS_P as low as 0.41 (Figure 6). This is in striking contrast with phosphorylation by phosphorous acid and molten urea, where a DS_P of at least 1.0 is required for the resulting phosphorylated cellulose derivatives to be fully water-soluble [3]. The amount of phosphorylated cellulose increased with the increase of DS_P. The highest solubility of 45g in 100g of water was attained at a DS_P of 1.30 (Figure 7). Such high water solubility of the phosphorylated celluloses prepared with [DMIm][(MeO)(H)PO_2] appears to be attributable to the ionic character of the resulting cellulose derivatives, which comprise an 1,3-dimethylimidazolium cation and a phosphite-containing anion in a repeating glucose unit.

The thermal properties of phosphorylated cellulose and crystalline cellulose were investigated via a thermogravimetric analysis (TGA). As shown in Figure 8, unmodified crystalline cellulose rapidly decomposed at temperatures over 300°C and less than 10wt% of

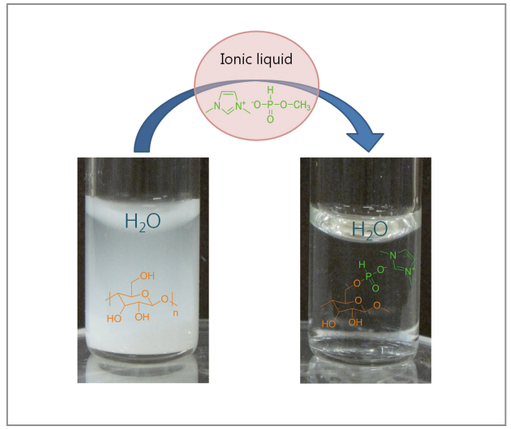

Figure 6. Photograph shows the solubility of cellulose (left) and phosphorylated ionic cellulose, A1 (right) in water at room temperature (0.15 g of sample in 1 mL of water).

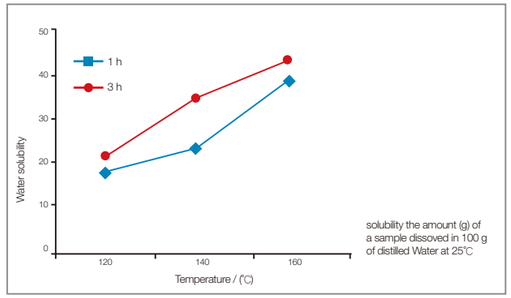

Figure 7. The relationship between water solubility of ionic cellulose and reaction temperature and time.

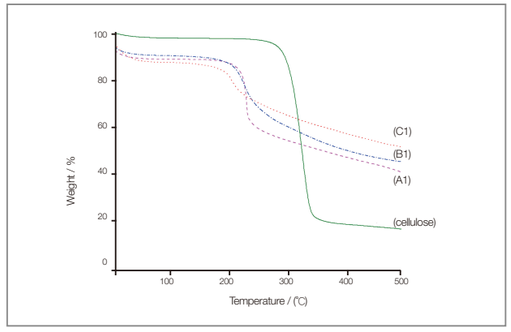

Figure 8. TGA curves of cellulose and phosphorylated celluloses, A1, B1, and C1.

its original weight remained at 500°C. In contrast, the phosphorylated cellulose decomposed at around 250°C, which is much lower than the temperature at which microcrystalline cellulose broke down.

The decomposition temperature of phosphoryl celluloses was lowered with the increase of DS_P, but the weight loss was smaller at higher DS_P. Above 250°C, the decomposition rate of phosphorylated celluloses proceeded much more slowly, and approximately 40 – 50% of residue remained at 500°C, depending on the DS_P. This behavior can be ascribed to the facile formation of polymetaphosphoric acid, which is known to inhibit further decomposition [3]. The obtained XRD patterns and SEM images showed that all phosphorylated celluloses were in amorphous states (Figures 9 and 10).

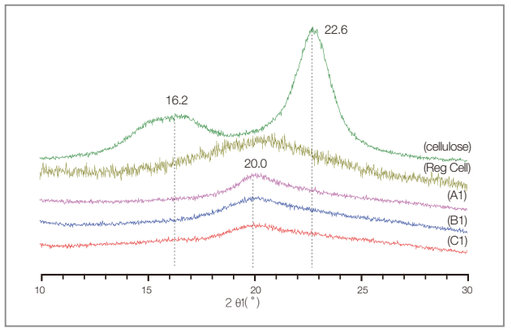

Figure 9. X-ray diffraction spectra of microcrystalline cellulose, regenerated cellulose obtained after dissolution of cellulose in [DMIm][(MeO)(H)PO_2] at 100°C for 1 h, and phosphorylated ionic celluloses.,

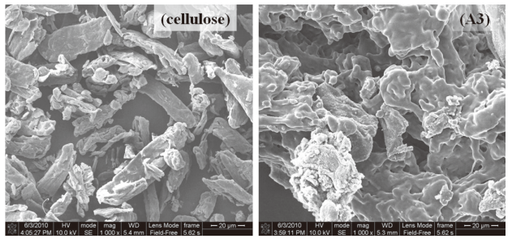

Figure 10. Scanning electron microscope images of (magnification x 1000) of microcrystalline cellulose and water-soluble ionic cellulose, A3.

Conclusion

Water-soluble ionic cellulose derivatives comprising an imidazolium cation and a phosphorylated cellulose anion were conveniently synthesized in high yields from the dissolution of cellulose in [Dmim][(MeO)(H)PO_2] at temperatures of 120°C and higher without employing an inorganic acid or an amine. The phosphorylation mainly occurred at the C6 position in AGU. The DS_P of phosphorylated cellulose could be controlled by adjusting reaction time and temperature. The DS_P increased with increasing reaction temperature and time, and reached a maximum DS_P value of 1.3 at reaction conditions of 160°C for 3 h. Unlike other types of phosphorylated cellulose reported so far, the ionic phosphorylated celluloses prepared in this study are soluble in water even at a DS_P as low as 0.41. The TGA experiment showed that the ionic phosphorylated celluloses have high char ratios of around 40 – 50% at 500°C, implying that they have flame retardant properties.

Note

This article and images are cited from “Ionic-Liquid-Derived, Water-Soluble Ionic Cellulose” in *Chemistry, A European Journal*. 2012; 18: 9019-9023.

References

[1] Vo TH, Kim CS, Ahn BS, Kim HS, Lee H. J. *Wood Chem. Technol.* 2011; 31: 89–102.

[2] Vo TH, Kim YJ, Jeon EH, Kim CS, Kim HS, Lee H. *Chem. Eur. J.* 2012; 18: 9019 – 9023.

[3] Suflet DM, Chitanu GC, Popa VI. *React. Funct. Polym.* 2006; 66: 1240–1249.

[**Feature Articles**]

Electrocatalyst Design for Proton Exchange Membrane Fuel Cells

Sung Jong Yoo
Fuel Cell Research Center
ysj@kist.re.kr

Introduction

Fuel cells are promising alternative devices for reducing our reliance on environmentally unfriendly fossil fuels. In particular, polymer electrolyte membrane fuel cells (PEMFCs), which efficiently convert chemical into electrical energy, possess great potential as substitutes for conventional combustion engines in future mobile applications. Over the past 20 years great progress has been made in many technical aspects related to the commercial large-scale deployment of PEMFCs, so that the manufacturing of stacks, their implementation in vehicles, and even extended road tests on our streets are nowadays standard practice. However, several problems must be overcome if fuel cells are to become economically viable. A pivotal issue is the overpotential associated with the slow kinetics of the oxygen reduction reaction (ORR; $(1/2O_2 + 2(H^+ + e^-)$ H2O)) at the cathode. The strategies to improve ORR kinetics are diverse, ranging from the bi-/multi-metallically alloying with transition metals (Co, Ni, Cr, Mn, Pd) and dealloying of selected Pt alloys to yield Pt core-shell catalysts [1, 2]. Recently, studies on Pt-based alloys have been conducted related to the correlation between the surface electronic structure of Pt as modified by a second transition metal and catalytic activity for the ORR [3]. Another tremendous challenge concerns stability issues such as metal dissolution and surface oxide formation, conditions which arise easily in the hostile electrochemical environment of a fuel cell [4]. Recently, some researchers have reported stable cathode catalysts by alloying Pt with early transition metals and have emphasized the importance of considering the stability of Pt-skin surface alloys and Pt

modified with Au clusters [2,5]. However, despite intense efforts to find a stable catalyst with good ORR kinetics, direct experimental investigation of interrelationships between stability and activity have rarely been pursued.

To achieve these performance goals at KIST, we have focused on electrocatalyst design by evaluating experimental results and developing theoretical calculations for screening both the activity and the stability of various transition metal alloys of Pt and Pd with different compositions, and then assessing these predictions with further experimentation. In this way we have been able to demonstrate new prospective electrocatalytic materials. Our results represent an important step forward toward resolving serious problems in fuel cell performance and making PEMFCs economically viable.

Fuel cell components and the challenge for commercialization

A fuel cell produces electricity from the electrochemical oxidation of hydrogen. It is manufactured as a stack of identical repeating unit cells comprising a membrane electrode assembly (MEA) in which hydrogen gas is oxidized on the anode and oxygen gas is reduced on the MEA cathode, all compressed by bi-polar plates that introduce gaseous reactants and coolants to the MEA and harvest the electric current (Figure 1).

The electrochemical reactions occur in the MEA electrodes, each attached to a proton exchange membrane that conducts protons but not electrons. The cathode ORR and anode hydrogen oxidation reaction both occur on the surfaces of Pt-based catalysts. Pure water and heat are the only byproducts. Porous gas diffusion layers transport reactants and product water between the flow fields and catalyst surfaces while exchanging electrons between them.

The viability of fuel-cell MEAs is determined by three major criteria: cost, performance and durability. The cathode ORR is six or more orders of magnitude

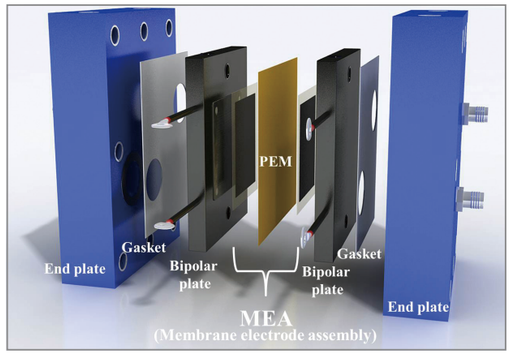

Figure 1. Fuel cell components.

slower than the anode hydrogen oxidation reaction and thus limits performance, so almost all research and development focuses on improving the cathode catalysts and electrodes. Most MEA catalysts used today are based on Pt, with the high price of this scarce precious metal having a decisive impact on costs. Fuel-cell vehicles in the test fleets monitored by the United States Department of Energy have used 0.4 mg of Pt per square centimetre, but in these vehicles the catalyst/MEA stability has still been short of the 5,000-hour durability target [6]. How to reduce costs by reducing cathode loadings to <0.1 mg Pt cm^{-2} without loss of performance or durability is the subject of most electrocatalyst research [6].

Electrocatalyst design

Density functional theory (DFT) calculations have become an important tool for understanding the properties of metal surfaces and their reactivity, including the effects of structure, alloying, and adsorption. This theoretical approach has begun to suggest the design of surfaces with specific catalytic properties of interest. In fuel cells, electrochemical reactions such as HOR and ORR have been explained by this theoretical approach. In the case of the ORR, it is truly needed to reduce a large overpotential even on Pt. Nørskov *et al.* have already

shown the origin of the ORR [7]. Furthermore, they suggested promising candidates with enhanced ORR rates and higher stability [8].

Alloying Pt with other transition metals can downshift the d-band center position of surface Pt [9]. This shift dominates the trends in binding the energy of adsorbates, i.e., oxygen-containing species. In the d-band model, the simplest one-electron description of the quantum mechanics of atoms and molecules interacting with a metal surface is assumed and provides the essential physics for understanding the concept of the interaction between metal and adsorbates. The narrow d-bands are a consequence of the small coupling matrix element Vdd between the localized d-states; one of the important conclusions from tight binding theory is that the band width is proportional to Vdd [10]. Since d-bands are narrow, the interaction of an adsorbate state with the d-electrons of a surface gives rise to bonding and antibonding states just as in a simple two-state problem, as shown in Figure 2.

In general, the coupling of the adsorbate states to the metal d-bands will depend on a number of parameters, i.e., the energy of the adsorbate state(s), the d-density of states projected onto the metal atoms, and the coupling matrix element. Therefore, changes in the position of the d-band cannot fully explain trends in the reactivity of all transition metals. However, if surface metal is fixed (for instance, an oxygen atom bonding to a Pt atom), its reactivity with different substrates can be conceptually explained with this model. This thesis is focused on the

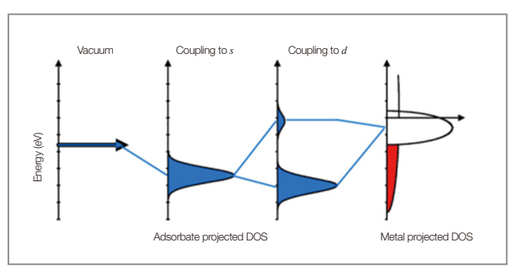

Figure 2. Schematic illustration of the formation of a chemical bond between an adsorbate valence level and the s- and d-states of a transition metal surface (reprinted from ref. 10).

oxygen reduction reaction. Therefore, the binding energy of oxygen is representative of the activity because oxygen has a scaling relationship with O_2, OH, and OOH.

As the d-band center shifts up, a distinctive antibonding state appears above the Fermi level. The antibonding states above the Fermi level are empty, and the bond becomes increasingly stronger as their numbers increase. Thus, strong bonding occurs if the antibonding states are shifted up through the Fermi level (and become empty), and weak bonding occurs if antibonding states are shifted down through the Fermi level (and become filled). Consequently, a Pt overlayer on different substrates (surface alloys) can result in different reactivity in the ORR.

Log on for new electrocatalysts

Our group reported a new set of more stable and active electrocatalytic cathode materials comprised of Pt-based alloys made of inner transition metals such as La. In particular, we considered Pt–La alloys and focused on their electronic effects to correlate activity to stability. To clarify these effects, we first introduced a correlation between the d-band structure of Pt, which is induced by charge transfer between Pt–La alloys, and the ORR activity/stability. By analyzing the d-band fillings and d-band vacancies of Pt–M alloys, we confirmed that the electronic effects govern not only ORR activity, but also stability under acidic conditions.

When Pt–La alloys are used, the changes in the electronic structure of Pt during the alloying with La facilitate the transition of the adsorbed OH to water by the modification of the binding energy of the oxygen-containing species (OCS). Further, appropriate parameters such as the d-band center can be helpful in discussing the electronic structure of Pt alloys. We measured the d-band centers for Pt3M alloys by using synchrotron-based high-resolution photoelectron spectroscopy; this methodology has been described previously [11]. The measurements of the d-band centers enable us to directly

correlate the variations in ORR catalytic activity with the variations in Pt_3M alloys. As shown in Figure 3, the d-band centers of Pt versus the kinetic current density exhibit a volcano curve. This result indicates that the ORR activity is given by the strength of the OCS–Pt bond interaction, which depends on the position of the Pt d-band states relative to the Fermi level. However, if the position of the d-band centers of Pt becomes extremely high, the ORR currents decrease because they are blocked due to the stronger adsorptive bond strength of the OCS. This situation leads to the maximum possible catalytic activity wherein the ability of the Pt_3La alloy to bind the OCS is neither too weak nor too strong.

As mentioned above, Pt activity is related to its d-band center position. Further, the d-band center position is directly related to the reactants, adsorption energies, and activation barriers [2,3]. The position of the d-band center depends on the electronic interactions between Pt and La. However, from an electronic viewpoint, the resulting structure suggests an inadequate electrode for the ORR because the effects of tensile strain on alloys affect the d-band structure (i.e., the d-band center); an increase in the lattice constant decreases the bandwidth, and the d-states increase in energy [2,3]. This leads to stronger adsorptive bond strengths for the OCS and the

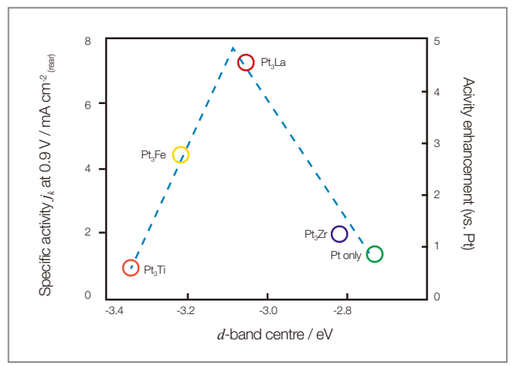

Figure 3. Kinetic current density (jk) for ORR on the Pt–M (M = Zr, La, Fe, and Ti) alloy and pure Pt electrodes in a 0.1 M $HClO_4$ solution, as a function of the measured d-band centers. The d-band centers were measured by high-resolution X-ray photoelectron spectroscopy (HR-XPS).

consequent blocking of the active sites. In such a case, an important question is how we can experimentally observe the downshifts of the d-band center on a Pt_3La alloy undergoing tensile strain.

We consider that the high electron affinity of Pt affects the electronic density of La and leads to depletions in the number of d-electrons in the La atoms. The intrinsic reason for the increase in the ORR activity on Pt_3La alloys is the electronic effect induced by the incorporation of atoms, such as La atoms with depleted electrons, into the Pt lattice. Despite the tensile strain, this electronic effect leads to a downshift in the metal d-band center and weakens the interactions between the substrate and adsorbate [12]. To evaluate this argument, we used measurements from X-ray absorption near-edge spectroscopy (XANES) on Pt–La alloys as well as the Pt L_{III} edges. One significant aspect of XANES analysis is that it can provide important information on the Pt d-band vacancy from an analysis of the Pt L_{III} white lines. Figure 4a shows the results of the calculation of the d-band vacancy of Pt as a function of the degree of alloying. In a previous study, the fractional changes in the number of d-band vacancies relative to the reference material were estimated from the differences between the amplitudes for the Pt L_{III} absorption edges of the sample (pure Pt and Pt–La alloys) and a Pt reference foil. This technique represents a new method of examining the role of the alloying element in Pt alloys in the d-band vacancy of Pt. Hence, we have also used this method to elucidate the differences in the degree of electrocatalysis in the case of Pt and Pt–La alloy electrocatalysts. As shown in Figure 4b, the number of Pt 5d holes in the case of all the Pt–La alloy samples is smaller than that in the case of pure Pt. The small vacancy of the Pt d-band means that the density of the Pt state increased from below the Fermi level to just above the metal Pt valence band, which shifted the d-band center downward in energy toward the Fermi level. In other words, the Pt_3La alloy electrode obtains O, OH, and OOH, thereby accelerating the desired oxygen-splitting reactions.

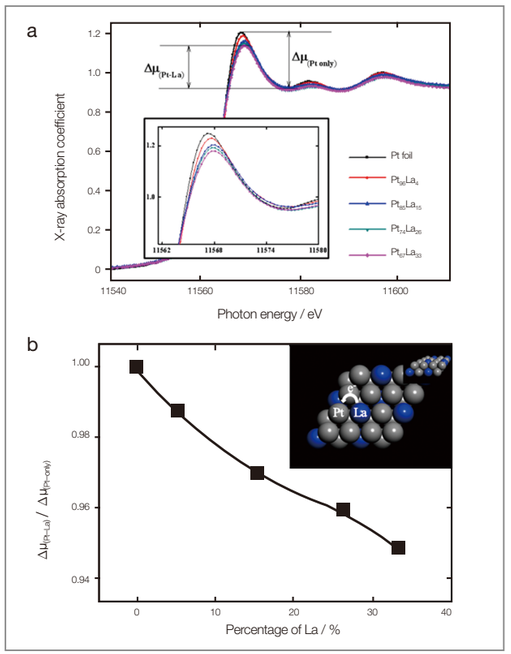

Figure 4. (a) X-ray absorption near edge structure (XANES) spectra obtained with the Pt–La alloy catalysts. (b) Comparison of the changes in the LIII-edge absorption peak as a function of the composition of Pt–La alloy catalysts.

In general, charge transfer can rarely be expected in the case of bimetallic alloys; rather, the d-bands maintain a constant filling (within the, so called, "rigid band model") [12]. However, strong electronic interactions related to the heterometallic Pt_3La bond formation between the large electronegativity (Pt) and small electronegativity (La) might substantially influence the d-band vacancy shifts. Since the bulk electronegativity of La (1.10) is considerably smaller than that of Pt (2.28), the formation of a metal–metal bond between La and Pt induces the electron density to flow from La to Pt. While the precise contributions of this effect on the experimentally observed lattice parameter shifts are still not fully understood, the two effects must be considered when analyzing d-band vacancy shifts. In order to elucidate the origin of the stability of Pt_3La alloy catalysts used in electrocatalytic ORRs, we compared a Pt electrode with Pt_3M electrodes in electrochemical environments. In a recent report, the electrocatalytic stability of the ORR was established to be a function of either the thermodynamically calculated heat of alloy formation or the calculated oxygen binding energy [4]. Although these results have provided valuable information, it has still not been possible to establish real systematic experimental trends. To date, variations in electronic structures have been employed to determine the trends in the electrocatalytic stability of the ORR across the periodic table. At this point, it is important to emphasize that the relationships summarized in Figure 5 are unique in establishing a correlation between the experimentally determined d-band vacancies of Pt_3M alloys and stability when the fillings of the d-band states are systematically changed across d-band vacancies. The stability effect for Pt_3M was determined using an accelerated stability test by continuously applying linear potential sweeps from 0.6 to 1.1 V, which caused surface oxidation/reduction cycles of the catalysts.

The accelerated stability measurements of the catalysts on an RDE was estimated by applying a potential sweep at the rate of 50 mV s^{-1} in an O2-saturated 0.1 M $HClO_4$ solution at 25°C. This potential region generally occurred during metal dissolution and surface oxide formation. Pt_3La alloy catalysts showed little decrease in activity after 3000 cycles.

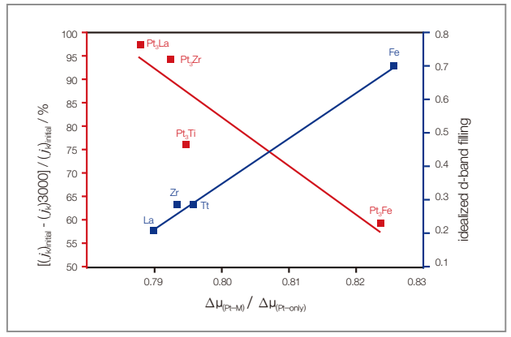

Figure 5. Variations in kinetic current density (j_k; red square symbols) at 0.9 V for ORR on Pt_3M (M = La, Zr, Ti, and Fe) electrodes after 3,000 cycles in a 0.1 M $HClO_4$ solution and idealized d-band filling (blue square symbols) as functions of the changes in the L_{III} edge absorption peak on Pt–M.

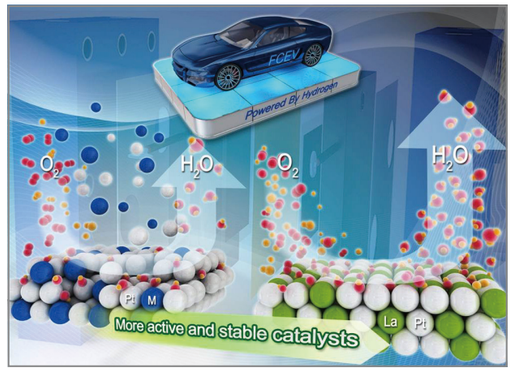

Figure 6. Schematic diagram of ORR on a Pt_3La alloy electrode

In particular, the correlation between the stability and d-band filling on the Pt_3M alloy catalysts exhibited a linear shape, thus implying that the stability is influenced by the nature of the d-band fillings of Pt_3M alloys. Therefore, the high stability of Pt_3La alloy catalysts can be understood in terms of metal–metal d-bands that are approximately half-filled. Half-filled metal–metal d-bands imply that each of the two elements in the band contributes half of the nine d-electrons for Pt, and La contributes one d-electron; moreover, the bonding states are filled while the anti-bonding states are empty. As shown in Figure 6, the knowledge obtained from the study of the electrocatalytic trends of the stability of the Pt_3M alloy catalysts can be used to explain the stability patterns as well as to provide fundamentals for realizing improvements in alloy cathode catalysts.

Conclusion

We have shown that substantially improved ORR electrocatalysis occurs at a Pt_3La alloy electrode. We have also revealed the principal role of the electronic effects of Pt3La alloys on the ORR. We have demonstrated that the relationship between the kinetic current density and d-band center of Pt_3M alloying exhibits a volcano curve trend. Further, the stability of the catalysts is given by a relationship between the numbers of d-band vacancies of Pt on the Pt_3M alloy electrodes as a function of the changes in the L_{III} edge absorption peak for Pt_3M. Our current research thus suggests possibilities for stabilizing Pt-based alloy catalysts while simultaneously increasing the ORR activity in electrochemical environments.

Note

This article is based on our recent papers: *Chem Comm*. 2011; 47: 11414., *Energy Environ Sci*. 2012; 5: 7521., *Int J Hydrog Energy*. 2012; 37: 4394.

References

[1] Yoo SJ, Park H-Y, Jeon T-Y, Park I-S, Cho Y-H, Sung Y-E. *Angew Chem Int Ed.* 2008; 47: 9307.
[2] Stamenkovic VR, Fowler B, Mun BS, Wang G, Ross PN, Lucas CA, Markovic NM. *Science.* 2007; 315: 493.
[3] Stamenkovic VR, Mun BS, Arenz M, Mayrhofer KJJ, Lucas CA, Wang CA, Ross PN, Markovic NM. *Nature Mater.* 2007; 6: 241.
[4] Greeley J, Nørskov JK. *J Phys Chem C.* 2009; 113: 4932.
[5] Zhang J, Sasaki K, Sutter E, Adzic RR. *Science.* 2007; 315: 220.
[6] U.S. DOE Hydrogen Program Annual Merit Review and Peer Evaluation Meeting, 2011.
[7] Nørskov JK, Rossmeisl J, Logadottir A, Lindqvist L, Kitchin JR, Bligaard T, Jonsson H. *J Phys Chem B.* 2004; 108: 17886.
[8] Greeley J, Stephens IEL, Bondarenko AS, Johansson TP, Hansen HA, Jaramillo TF, Rossmeisl J, Chorkendorff I, JK Norskov. *Nature Chem.* 2009; 1: 552.
[9] Kitchin JR, Norskov JK, Barteau MA, Chen JG. *J Chem Phys.* 2004; 120: 10240.
[10] Bligaard T, Norskov JK. *Electrochim Acta.* 2007; 52: 5512.
[11] Mun BS, Lee C, StamenkovicV, Markovic NM, Ross PN. *Phys Rev B.* 2005; 71: 115420.
[12] Mavrikakis M, Hammer B, Nørskov JK. *Phys Rev Lett.* 1998; 81: 2819.

[Feature Articles]

Environmental Catalyst Synthesis by Chemical Vapor Condensation(CVC) for Pollutant Decomposition

Jongsoo Jurng
Center for Environment, Health, and Welfare
jongsoo@kist.re.kr

Sungmin Chin

Eunseuk Park

Yeonseok Kim

Introduction

Our research has focused on developing nanosized catalysts for pollutant decomposition. Nanocatalysts composed of metal oxide are well-suited to environmental applications because their smaller particles and synthesis methods result in novel properties, one of which is increased surface area created by the use of smaller crystals.

Recently, several vapor-phase synthesis methods have been developed to synthesize nanosized catalysts. These methods include the flame-made process, hydrothermal process, spray pyrolysis and microwave plasma-torch process, as well as others. Among these methods, the chemical vapor condensation (CVC) process stands out as a particularly effective method for the direct synthesis of nanosized catalysts. The CVC process was chosen as the method for synthesizing nanocatalysts in our study [1].

We performed the synthesis of transition metal (Ti, Mn, V) oxides and metal oxide loading on TiO_2 by the CVC process. Using CVC-synthesized catalysts, we focused on the selective catalytic removal of NO_x (NH_3-SCR), VOCs (toluene) and 1,2-dichlorobenzene over metal (V_2O_5, Mn_2O_3) loading on TiO_2 catalysts. Generally speaking, our results indicated that pore size and specific surface area of a TiO_2 support were not reduced by metal loading because the loaded material was uniformly distributed on its inner surface, unlike in commercial TiO_2 particles. We found that the catalytic activity of synthesized nanocatalysts is higher than commercial catalysts, especially at lower reaction temperatures (~200°C).

Vapor-phase synthesis of nano catalysts

The production of nanosized catalysts can be approached by using liquid, gas (vapor-phase) or solid synthesis methods. The liquid methods include sol-gel, precipitation and hydrothermal methods. The solid methods involve techniques such as the direct crushing of bulk materials and mechanical alloying. The most common vapor-phase methods include spray drying, evaporation-condensation, chemical vapor deposition, flame synthesis and plasma methods. Production of TiO_2 nanoparticles by the vapor phase method is superior to that of the wet method (e.g. sol-gel process) due to the continuous production of high purity TiO_2 crystals.

Our research group developed the vapor-phase CVC method and has applied it to the production of various catalysts, such as titanium dioxide, manganese oxide, vanadium oxide and metal-loaded on TiO_2 supports. The particles produced through the vapor-phase CVC synthesis process (Figure 1) are advantageous for use in catalysts due to their homogeneous composition, adjustable size, crystallinity, shape, and microstructure.

Table 1 lists the vapor phase (CVC)-synthesized

	Materials	Precursors	Synthesis Methods	Analysis Method	Pollutants	Targets	Reference
Single Component	TiO_2	TTIP	CVC	XRD/TEM/XPS	O (Methylene blue)	Physico-chemical properties of the CVC-TiO_2 (synthesis condition-temperature, precursor concentration)	[2], [3]
				XRD/TEM/XPS	O (*E.coli*)	Antibacterial activity of nanocatalysts under UV(365nm) irradiation (*E. coli*)	[4]
	MnO_x	$Mn_2(CO)_{10}$: manganese(0) carbonyl		XRD/TEM/XPS	X	Synthesis of MnO_x by CVC & Identify the physic-chemical properties	[5]
	VO_x	$(VO(OC_2H_5)_3$: Vanadium(V) oxytriethoxide		XRD/TEM/XPS	X	Synthesis of VO_x by the CVC & Identify of the physic-chemical properties	[6]
CVC-TiO_2 Nano-composites	MnO_x/TiO_2	TTIP & Manganese acetate	CVC (TiO_2) & impregnation (Mn)	XRD/XPS/HR-TEM&mapping	O (VOCs :toluene) (5 wt% Mn/Ti)	Effects of the support catalyst characteristics and the catalytic oxidation of toluene over MnO_x/TiO_2 catalysts	[7]
				EXAFS/TPR/TPD	X (2-10 wt% Mn/Ti)	Determine the optimal Mn loading concentration	[8]
		TTIP & Manganese nitrate		XRD/XPS/UV -vis spec.	O (Methylene blue) (1 wt% Mn/Ti)	Methylene blue degradation of Mn/TiO_2 under UV irradiation	[9]
		TTIP & Manganese (acetate & nitrate)		XRD/TEM/XPS	O (NO oxidation) (10 wt% Mn/Ti)	NO oxidation of different Mn precursor impregnated on TiO_2	[10]
		TTIP & $Mn_2(CO)_{10}$: Manganese(0) carbonyl	CVC (one-step)	TGA/XRD/TEM/XPS	X (2-20 wt% Mn/Ti)	Synthesis of Mn/TiO_2 by the one-step CVC process	[11]
	V_2O_5/TiO_2	TTIP & Vanadium oxytripropoxide	CVC (mixing of Ti and V precursors)	XRD/TEM	O (1,2-DCB: dichlorobenzene)	Catalytic destruction of 1,2-DCB under various synthesis conditions (precursor heating temperature synthesis temperature)	[12]
			CVC (two-step)		X (5-20 wt% V/Ti)	Synthesis of VO_x/TiO_2 by the one-step CVC process	[13]
		TTIP & Ammonium metavanadate	CVC (TiO_2) & impregnation (V)	EDX mapping	O (1,2-DCB: dichlorobenzene)	Catalytic destruction of 1,2-DCB over V_2O_5(5wt%)/TiO_2	[14]
				XRD/TEM/XPS	O (Methylene blue)	Methylene blue degradation of VO_x(5wt%)/TiO_2 under UV-vis irradiation (550nm)	[15]

Table 1. Vapor-phase synthesized materials and their applications.

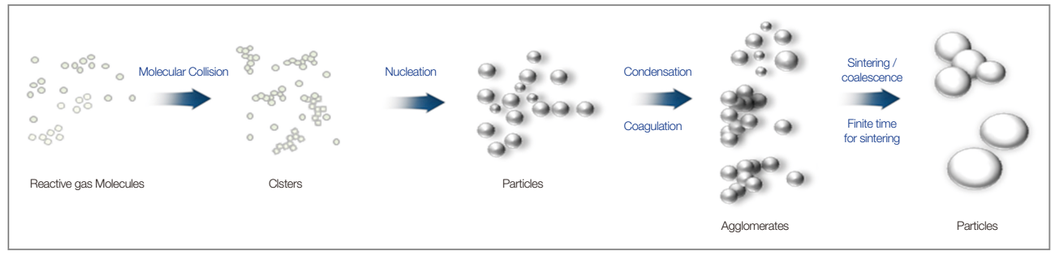

Figure 1. Scheme of CVC process.

materials and related environmental applications that our research group has investigated. The nanoscale materials produced via these CVC routes were applied as photocatalysts or catalysts for air pollution control purposes. CVC-synthesized TiO_2 particles (CVC-TiO_2) have a very high surface area of around 150 m^2/g, and are thus suitable as catalyst supports [2].

Characteristics of synthesized nanocatalysts

We developed a synthesis process for single and composite nanocatalysts by improving the chemical vapor condensation process. Our team has also manufactured nanocatalysts with diverse colors without coagulation (Figure 2) by building on prior research into evaporation temperature, reaction temperature, particle resident time within a reactor, reaction gas ratio, concentration of precursor and particle collecting methods and other conditions in an effort to further improve the surface characteristics of nanocatalysts proposed in other studies.

The physico-chemical properties of synthesized (CVC process) catalysts were analyzed by various techniques, including XRD, TEM, BET and XPS which are the best techniques for understanding the characteristics of materials. The synthesized catalysts showed smaller particle size, larger surface area, higher purity, and less agglomeration in comparison to catalysts of the same composition produced from other methods (conventional TiO_2-Degussa P25) [5,6].

The physical properties of the tested nanocatalysts are listed in Table 2. It is worth noting that the specific surface area (SSA) of TiO_2 particles synthesized by vapor-phase synthesis (CVC) was three times larger (ca. 150 m^2g^{-1}) than that of conventional TiO_2 particles. Also, when the CVC-TiO_2 catalyst was used as a support material and impregnated with various metal catalysts such as V_2O_5, the SSA increased six times (ca. 300 m^2g^{-1}) more than commercial catalysts.

Adding metal components to a commercial TiO_2 particle can reduce particle pore size and enable pore blocking. Consequently, the metal on synthesized nanocatalysts is dispersed well, creating a monodisperse of spherical shapes with diameters <10 nm, thus increasing the SSA. TEM mapping images photographed

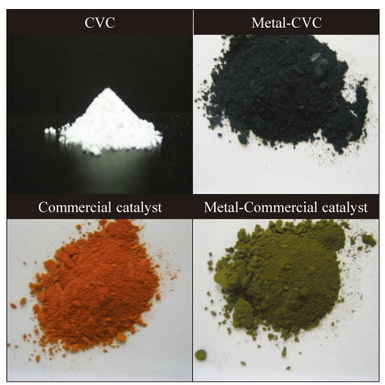

Figure 2. Photographs of nanocatalysts.

Sample	BET surface area (m^2 g^{-1})	Particle size (nm)[a]	OH (O1s) content (%)
CVC nanocatalyst	140-150	< 10	32.2
Metal-CVC nanocatalyst	250~300	< 10	37.1
Commercial nanocatalyst	45-50	> 20	14.3
Metal-commercial nanocatalyst	<50	> 20	15.2

Table 2. BET surface area, particle size and OH (O1s) content of nanocatalyst samples.

in this study also confirmed the monodisperse of metal (Figure 3) [8].

CVC-TiO_2 particles were found to have anatase content over 97% of its total components (Figure 4) with a very small rutile phase. Also, the ratio of their hydroxyl group (OH), which increases photocatalytic activity on the catalyst surface, was over 32%, which is more than twice that of commercial catalysts (14%).

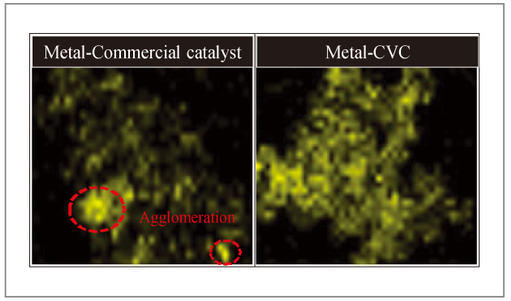

Figure 3. Metal dispersion of nanocatalysts.

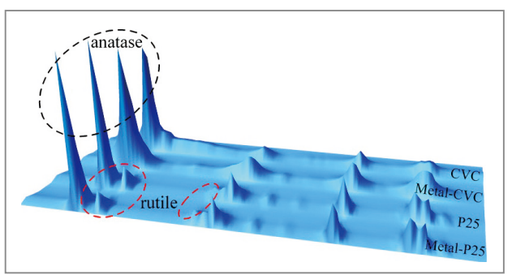

Figure 4. Crystal phase of nanocatalysts.

Photocatalytic removal using CVC TiO_2 nanocatalyst

These metal-loaded catalysts on CVC TiO_2 were applied to the removal of pollutants in air and water. Photocatalysis using TiO_2 is currently an important industrial process in wastewater treatment, heavy metal remediation, air purification, sterilization, and other environmental purification processes. We found that the photocatalytic degradation of organic matter with CVC TiO_2 nanoparticles was higher than that of commercial TiO_2 (P25). As illustrated in Figure 5, methylene blue (MB) decomposition tests using 120 min of UV irradiation revealed that over 80% of MB decomposed, leading the aqueous solution color to become thin compared with commercial catalysts. The higher SSA and enhanced crystallinity of CVC-TiO_2 photocatalysts had a beneficial

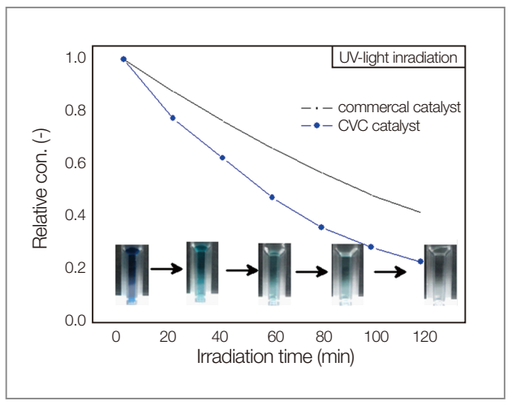

Figure 5. Photocatalytic degradation of MB under UV$^{254+185\,nm}$.

effect on photocatalysis and the abundance of anatase TiO_2 phase [3].

We also examined the photocatalytic decomposition of CVC TiO_2 and metal-loaded CVC TiO_2 under UV-visible irradiation. As shown in Figure 6, photocatalytic degradation of CVC TiO_2 was 2.5 times higher than the other catalysts (60 min visible irradiation) [9].

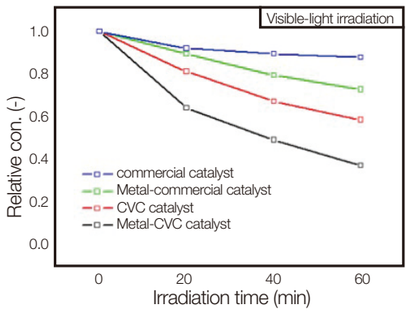

Figure 6. Photocatalytic degradation of MB under UV-visible light region.

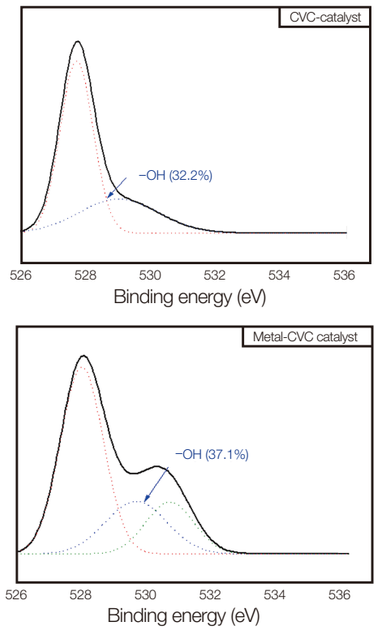

Figure 7. XPS spectra (O1s) of nanocatalysts.

In our study, the surface activation radical (OH group) was a major reason for improved results (Figure 7), as was the surface crystal phase, high SSA, and catalyst size [15]. Also, during metal impregnation, interaction with oxygen and metal oxides in the support lattice occurred, leading the band-gap energy to move to the visible light area and positively influencing visible photocatalytic activation.

Low-temperature catalytic decomposition of air pollutants

Further examination was conducted on the low-temperature oxidization ability of air pollutants using CVC-synthesized nanocatalysts, as well as the catalytic decomposition of VOCs (toluene), NO_x and 1,2-dichlorobenzene (1,2-DCB) over CVC-synthesized nanocatalysts (Figure 8).

First, in testing the removal of nitric oxide (NO_x), the synthesized catalyst showed up to 99% conversion efficiency in the lower temperature range (~250℃), which was superior to the maximum conversion ratio of 90% demonstrated by the commercial catalyst (~300℃). The commercial catalyst showed a sufficient removal efficiency at 300°C, but the CVC-synthesized catalyst showed over 80% of removal efficiency at 200°C, indicating a shift in reaction temperature to lower temperatures [10].

In the case of 1,2-DCB decomposition testing, a 90% efficiency was shown at a 200°C reaction temperature, while removal efficiency increased two times compared with the commercial nanocatalyst. The results from our prior tests suggest that this increased efficiency is due to the larger SSA value and higher V^{5+} content of the CVC-synthesized catalyst [12,14].

In the decomposition testing of VOCs (toluene), an excellent removal efficiency was also shown in the overall reaction temperature range, especially near room-temperature. Using CVC-synthesized nanocatalysts, overall conversion was good against pollutants compared

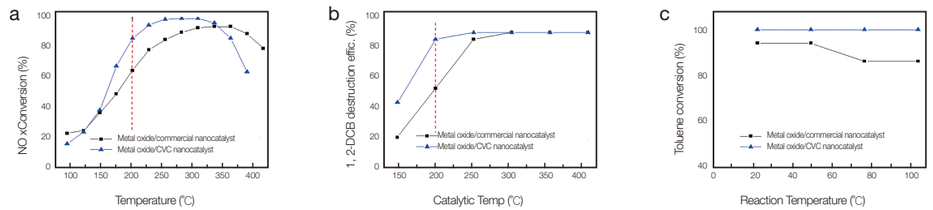

Figure 8. Catalytic conversion at different temperatures over nanocatalysts. (a) NO_x (b) Toluene (c) 1,2-DCB.

with commercial catalysts, as clearly shown in Figure 8, where the toluene oxidization ability was over 90% (under 40°C) [7]. Previous research has indicated a technical limitation at around 100°C reaction temperatures. Catalytic activity is different depending on the types of impregnated metal dispersion and of metal crystal phases. Furthermore, the issue of catalyst poisoning has yet to be resolved.

Photocatalytic disinfection of biological contaminants using CVC TiO_2 nanoparticles

The antibacterial activities of CVC-TiO_2 and commercialized TiO_2 nanoparticles (P25, Deggusa) against E. coli were investigated under UV-A irradiation. We found that the specific surface area and the crystallinity of CVC- TiO_2 nanoparticles varied depending on synthesis temperature and precursor vapor concentration. As a result, the CVC-TiO_2 nanoparticles showed a higher specific surface area and better crystallinity than that of P25 TiO_2. CVC-TiO_2 nanoparticles generated a larger amount of hydroxyl radicals than P25 TiO_2. Consequently, CVC-TiO_2 nanoparticles were more effective as an antibacterial photocatalyst than P25 TiO_2 under UV-A irradiation (Figure 9). The optimum synthetic conditions of CVC-TiO_2 nanoparticles for bactericidal effect were also found [4]

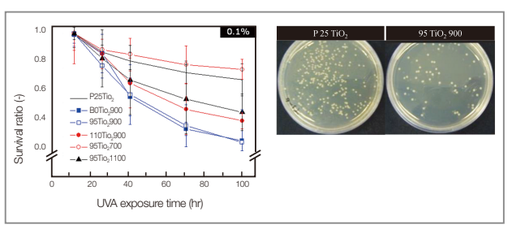

Figure 9. Antibacterial effects of CVC-TiO_2 and P25 TiO_2 nanoparticles under UV-A irradiation.

Visible-light-induced bactericidal activity of V_2O_5-TiO_2 nanoparticles

The bactericidal activity of TiO_2 nanoparticles under visible light is very important in regard to its practical applications. Therefore, we examined various pure and transition metal loaded TiO_2 nanoparticles synthesized by the CVC method in our lab.

In these experiments, the population of *E. coli* was shown to be significantly reduced by V_2O_5-TiO_2

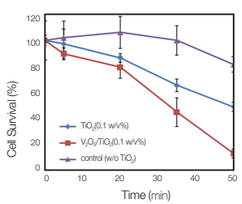

Figure 10. Survival of E. coli mixed with pure TiO_2 and V_2O_5-TiO_2 nanoparticles under fluorescent light illumination.

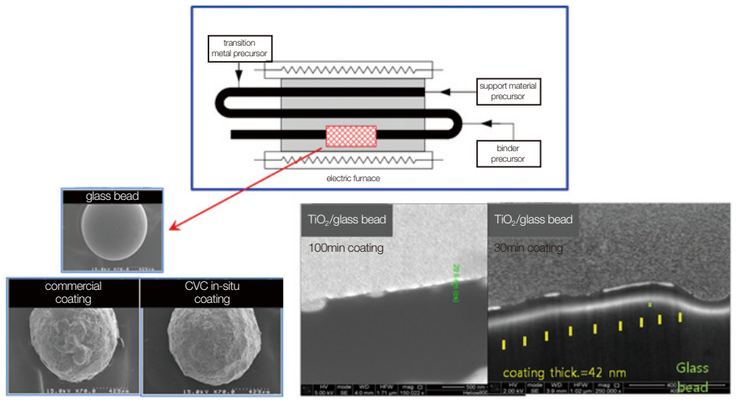

Figure 11. Images of nanocatalyst (synthesized TiO_2) coated beads.

nanoparticles under illumination with fluorescent light, whereas pure TiO_2 nanoparticles showed about a 3.3-fold lower antibacterial activity than the V_2O_5-TiO_2 nanoparticles (Figure 10). This result was most likely due to the change in surface conditions of the TiO_2 nanoparticles as a consequence of the loading of vanadium pentoxide on the TiO_2 nanoparticles. Both photo-catalysts showed similar antibacterial activity under UV-A (352 nm) irradiation.

Future plan

The goal for the research described in this article was the synthesis of the transition metal oxides Mn, V, and Ti oxides, and their application to the abatement of pollutants. Gaining this fundamental understanding of the properties of nanostructured catalysts, specifically their crystalline structures and morphology, electronic structures, and redox properties, is of great importance. In order to investigate the correlation between synthesis conditions and properties, the synthesis conditions of metal oxides by chemical vapor condensation should be further modified in order to develop and optimize production methods for well-defined, high quality catalysts [11].

The direct coating of TiO_2 nanoparticles onto glass beads using the CVC technique for environmental catalyst applications is already being studied by our research group. In preliminary testing, the thickness of the TiO_2 deposited onto the substrate was controlled by coating time. This allowed the TiO_2 catalyst to be completely deposited onto the glass bead, with a uniform shape, and with a reduced coating time (Figure 11). This simple process is an example of the continuing advances we are making in nanocatalyst development [13].

References

[1] Chang W, Skandan G, Hahn H, Danforth S, Kear B. *Nanostruct Mater* 1994; 4: 345.
[2] Chin SM, Park ES, Kim MS, Jurng JS. *Powder Technol.* 2010; 201: 171.
[3] Chin SM, Park ES, Kim MS, Bae GN, Jurng JS. *J Colloid Interf Sci.* 2011; 362: 470.
[4] Kim YS, Linh LT, Park ES, Chin SM, Bae GN, Jurng JS. *Powder Technol.* 2012; 215-216: 195.
[5] Le HA, Chin SM, Park ES, Linh LT, Bae GN, Jurng JS. *Chem Vapor Depos.* 2011; 17: 228.
[6] Le HA, Chin SM, Park ES, Bae GN, Jurng JS. *Chem Vapor Depos.* 2012; 18: 6.

[7] Park ES, Chin SM, Kim JS, Bae GN, Jurng JS. *Powder Technol.* 2011; 208: 740.
[8] Park ES, Chin SM, Le HA, Kim YS, Bae GN, Jurng JS. *Mater Res Bull.* 2012; 47: 1040.
[9] Park ES, Le HA, Chin SM, Kim JS, Bae GN, Jurng JS. *J Porous Mat.* 2012; 19:877.
[10] Park ES, Chin SM, Jeong JY, Jurng JS. *Micropor Mesopor Mat* 2012; 163: 96.
[11] Park ES, Chin SM, Kim YS, Bae GN, Jurng JS. *Powder Technol.* 2013; 233: 131.
[12] Chin SM, Jurng JS, Lee JH, Moon SJ. *Chemosphere* 2009; 75: 1206.
[13] Song MY, Chin SM, Jurng JS, Park YK. *Ceram Int.* 2012; 38: 2613.
[14] Chin SM, Park ES, Kim MS, Bae GN, Jurng JS. *Powder Technol.* 2012; 217: 388.
[15] Chin SM, Park ES, Kim MS, Bae GN, Jurng JS. *Mater Lett.* 2012; 75: 57.

Amygdalar stimulation produces alterations on firing properties of hippocampal place cells

The Journal of Neuroscience
2012; 32(33): 11424 –11434.

Eun Joo Kim, Earnest S. Kim, Mijeong Park, Jeiwon Cho, and Jeansok J. Kim
jeiwon@kist.re.kr (Co-Corresponding.)

Stress is a biologically ubiquitous factor that, when perceived uncontrollable by humans and animals, can have lingering adverse effects on brain and cognitive functions. We have previously reported that rats that experienced inescapable-unpredictable stress subsequently exhibited decreased stability of firing rates of place cells in the CA1 hippocampus, accompanied by impairments in CA1 long-term synaptic potentiation and spatial memory consolidation. Because the elevated level of glucocorticoid hormones and the heightened amygdalar activity have been implicated in the emergence of stress effects on the hippocampus, we investigated whether administration of corticosterone and electrical stimulation of the amygdala can produce stress-like alterations on hippocampal place cells. To do so, male Long–Evans rats chronically implanted with tetrodes in the hippocampus and stimulating electrodes in the amygdala were placed on a novel arena to forage for randomly dispersed food pellets while CA1 place cells were monitored across two recording sessions. Between sessions, animals received either corticosterone injection or amygdalar stimulation. We found that amygdalar stimulation reliably evoked distress behaviors and subsequently reduced the pixel-by-pixel correlation of place maps across sessions, while corticosterone administration did not. Also, the firing rates of place cells between preamygdalar and postamygdalar stimulation recording sessions were pronouncedly different, whereas those between precorticosterone and postcorticosterone injection recording sessions were not. These results suggest that the heightened amygdalar activity, but not the elevated level of corticosterone per se, reduces the stability of spatial representation in the hippocampus by altering the firing rates of place cells in a manner similar to behavioral stress.

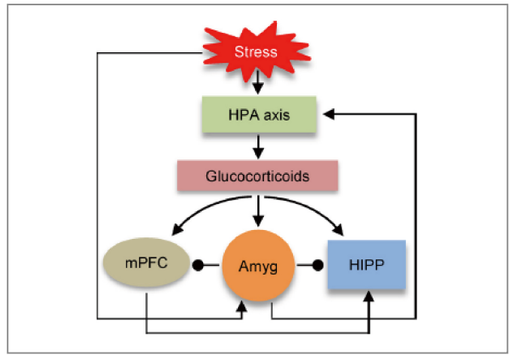

A hypothesized model of stress effects on hippocampal place cells. Stress triggers the HPA axis and heightens the amygdala (Ammg) activity. The HPA axis stimulates the release of glucocorticoids that directly initiate stress effects on the hippocampus (HIPP). The heightened amygdala activity will alter neuronal coding of hippocampal place cells, contributing to impairments in spatial information processing. The amygdala activity will also stimulate the HPA axis through the central amygdala output pathway, and suppress the cortical activity and thereby interfere with the cortico-hippocampal networking during spatial navigation.

Thermosensitive/magnetic poly(organophosphazene) hydrogel as a long-term magnetic resonance contrast platform

Biomaterials
2012; 33(1): 218-224.

Jang Il Kima, ChangJu Chun, Bora Kim, Ji Min Hong, Jung-Kyo Cho, Seung Hoon Lee, Soo-Chang Song
scsong@kist.re.kr

A thermosensitive/magnetic poly(organophosphazene) hydrogel (a magnetic hydrogel) was designed and synthesized for long-term magnetic resonance (MR) imaging. To turn a thermosensitive poly(organophosphazene) hydrogel (an original hydrogel) into a long-term MR contrast platform, cobalt ferrite ($CoFe_2O_4$) nanoparticles, which have hydrophobic surfaces, were bound to the original hydrogel via interactions between the hydrophobic surfaces of the nanoparticles and the L-isoleucine ethyl esters of the polymer. The magnetic hydrogel showed extremely low cytotoxicity and adequate magnetic properties for use in long-term MR imaging, in addition to possessing the same properties of the original hydrogel, such as viscosity, hermosensitivity, biodegradability, biocompatibility, a reversible sol-to-gel phase transition near body temperature, and injectability. The magnetic hydrogel was injected into a rat brain using stereotactic surgery. After the injection, the applicable potentiality as a long-term MR contrast platform was successfully estimated over 4-5 weeks. Consequently, it was shown that a magnetic hydrogel as a long-term MR contrast platform has the potential to be applied in a long-term theranostic hydrogel system. Furthermore, it is expected that this platform can be useful in the clinical field of incurable diseases due to either surgical difficulties or lethality, such as with brain tumors, when the platform is combined with therapeutic drugs for long-term MR theragnosis in further studies.

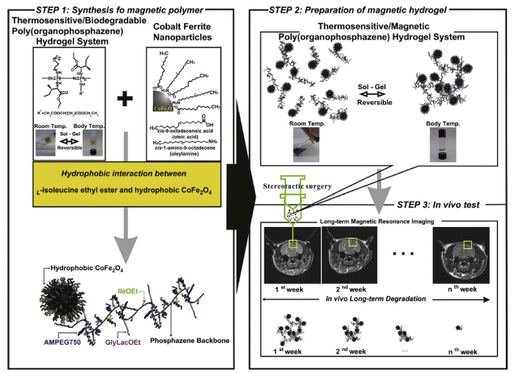

Schematic diagram showing process of synthesis of thermosensitive/magnetic poly(organophosphazene) hydrogel as a long-term MR contrast platform to *in vivo* estimation of long-term MR imaging reflecting the conditions of rat brains.

Three-dimensional hierarchical self-supported multi-walled carbon nanotubes/ tin(IV) disulfide nanosheets heterostructure electrodes for high power Li ion batteries

Journal of Materials Chemistry
2012; 22(18): 9330–9337.

Jin-Gu Kang, Gwang-Hee Lee, Kyung-Soo Park, Sang-Ok Kim, Sungjun Lee, Dong-Wan Kim, and Jae-Gwan Park
jgpark@kist.re.kr

Improving the power density of Li ion batteries (LIBs) is critically important for the development of high-end products and technologies. We investigated three-dimensional (3D) hierarchical self-supported multi-walled carbon nanotube (MWCNT)/tin(IV) disulfide nanosheet (SnS_2 NS) heterostructured electrodes, demonstrating superior rate capabilities of 480 and 420 mAh g^{-1} even at the very high c-rates of 5C and 10C (charging in 6 min), respectively. The reasons behind the enhancement of rate capabilities are discussed in detail with a focus on the roles of MWCNTs, which were grown directly on a metallic current collector. We also investigated the in-plane and plane-normal growth mechanisms of hexagonal SnS_2 NS from a crystallographic point of view.

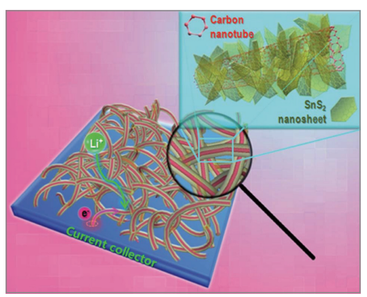

Schematic illustration of 3D hierarchical self-supported MWCNT/SnS_2 NS heterostructure electrodes.

Demonstration of a state-insensitive, compensated nanofiber trap

Physical Review Letters
2012; 109(3): 033603 1-5.

Goban, K. S. Choi, D. J. Alton, D. Ding, C. Lacroûte, M. Pototschnig, T. Thiele, N. P. Stern, and H. J. Kimble
kyung114@kist.re.kr

We report the experimental realization of an optical trap that localizes single Cs atoms $\simeq$215 nm from the surface of a dielectric nanofiber. By operating at magic wavelengths for pairs of counterpropagating red- and blue-detuned trapping beams, differential scalar light shifts are eliminated, and vector shifts are suppressed by ≈250. We thereby measure an absorption linewidth $\Gamma/2\pi$= 5.7±0.1 MHz for the Cs $6S_{1/2}$, F=4→$6P_{3/2}$, F'=5 transition, where $\Gamma_0/2\pi$=5.2 MHz in free space. An optical depth d$\simeq$ 66 is observed, corresponding to an optical depth per atom $d_1\simeq0.08$. These advances provide an important capability for the implementation of functional quantum optical networks and precision atomic spectroscopy near dielectric surfaces.

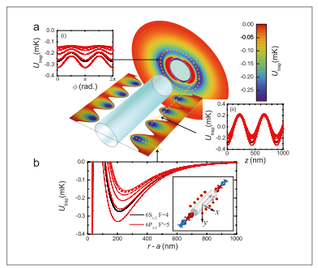

Adiabatic trapping potential U_{trap} for a state-insensitive, compensated nanofiber trap for the $6S_{1/2}$, F = 4 states in atomic Cs outside of a cylindrical waveguide of radius a = 215 nm. U_{trap} values for the substates of the ground level F = 4 of $6S_{1/2}$ (excited level F' = 5 of $6P_{3/2}$) are shown as black (red-dashed) curves. Due to the complex polarizations of the trapping fields, the energy levels are not the eigenstates of the angular momentum operators, but rather superposition states of the Zeeman sublevels. (a)(i) azimuthal $U_{trap}(\phi)$, (ii) axial $U_{trap}(z)$; and (b) radial $U_{trap}(r\text{-}a)$ trapping potentials. Input polarizations for the trapping beams are denoted by the red and blue arrows in the inset in (b).

rtho-Dichlorobenzene as a pore modifier for PEMFC catalyst electrodes and dense Nafion membranes with one porous surface

Journal of Materials Chemistry
2012; 22(29): 14602 – 14607.

Dirk Henkensmeier, Quoc Khanh Dang, N. Nambi Krishnan, Jong Hyun Jang, Hyoung-Juhn Kim, Suk-Woo Nam and Tae-Hoon Lim
henkensmeier@kist.re.kr

ortho-Dichlorobenzene (ODB) was investigated as a pore modifier for both Nafion membranes and proton exchange membrane fuel cell (PEMFC) catalyst layers. When ODB containing Nafion dispersions are cast into a film, evaporation leads to dense membranes with one highly porous surface layer occupying 20–30% of the overall thickness. Dense Nafion membranes with a porous top layer are interesting for use in membrane humidifiers, for increasing the electrode–membrane interface areas in electrochemical devices like fuel cells or electrolysers, and other applications. Fuel cell membrane electrode assemblies were obtained by spray coating commercial Nafion 212 membranes with ODB-containing catalyst inks. ODB does not poison the catalyst, and 54–120% higher potentials in comparison to the 217 mV obtained with an ODB free ink were achieved at 1.5 stoic air flow, 100% rh and a current density of 1 A cm^{-2}. This shows that the porous catalyst electrode structure is changed, resulting in a reduced contribution of mass transport limited overpotentials. Furthermore, MEAs prepared with ODB in the catalyst ink are less sensitive towards changes in the air flow rate and the cathode relative humidity (between 50% rh and 100% rh: 217–292 mV at 1 A cm^{-2} without ODB and 439–478 mV with ODB).

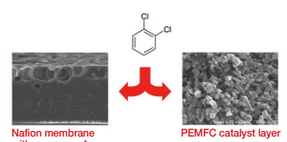

Gelation of natural polymer-dispersed suspensions under electric field

Soft Matter
2012; 8(2): 253-259.

Young Gun Ko and Ung Su Choi
uschoi@kist.re.kr

Potential applications for natural polymers have been intensively researched for a long time. Electrorheological (ER) fluids are a kind of colloidal suspension with rheological properties that can reversibly change within a millisecond over several orders of magnitude under a sufficiently strong electric field. By extension of the study on the properties of natural polymers to enlarge their applications, we briefly review ER materials based on natural polymers such as cellulose, starch, and chitosan. This highlight focuses on current research related to ER materials based on natural polymers and provides a perspective on this research.

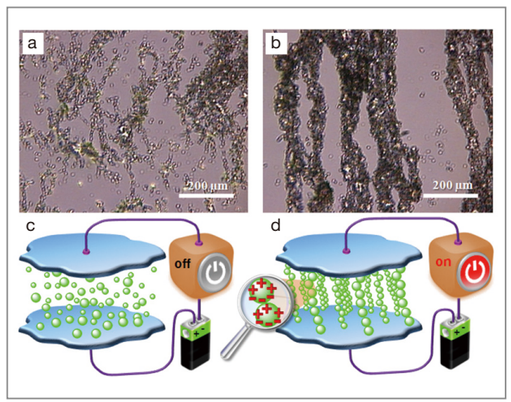

Figures (a) and (b) show the optical microscopy images of the chitosan particles in a suspension before and after application of a 3 kV/mm DC electric field. The structural patterns of the particles suspended in the ER fluid under the electric field are depicted in Figures (c) and (d).

FLEXIBLE ELECTRODES AND PREPARATION METHOD THEREOF, AND FLEXIBLE DYE-SENSITIZED SOLAR CELLS USING THE SAME

20120186644 (US)

KO, Min Jae / mjko@kist.re.kr

The present invention relates to a flexible photoelectrode and a manufacturing method thereof, and a dye-sensitized solar cell using the same. More particularly, the present invention relates to a flexible photoelectrode capable of forming a semiconductor electrode in a simple and stable manner with excellent photoelectric conversion efficiency at low temperatures on a plastic substrate. It is prepared by forming a nanocrystalline metal oxide layer calcined at high temperature on a high-temperature-resistant substrate, and transferring it to a flexible transparent substrate by a transfer method using an HF solution, and a flexible dye-sensitized solar cell comprising the same.

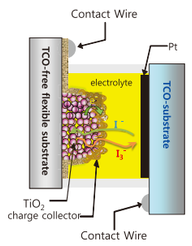

RANDOM GRAPHITE AND FABRICATION METHOD THEREOF USING GRAPHENE NANORIBBON

20120171109 (US)

LEE, Jae-Kap / jklee@kist.re.kr

This invention relates to random graphite, a type of graphite comprising three-dimensionally random graphene layers, and a fabrication method thereof which can be used at low temperatures below 100°C. Random graphite may have a large volume of empty space due to the presence of three-dimensionally random graphene nanoribbons and can be applied to Graphitic Intercalation Compounds (GICs) such as electrodes for Li-ion batteries.

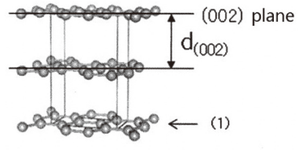

METHOD FOR FABRICATING GRAPHENE SHEETS OR GRAPHENE PARTICLES USING SUPERCRITICAL FLUID

20120171108 (US)

KIM, Jaehoon / jaehoonkim@kist.re.kr

This invention relates to a method for fabricating graphene sheets or graphene particles and includes: (a) dispersing graphene oxide in an alcohol solution to prepare a graphene oxide dispersion solution; (b) reducing the graphene oxide dispersion solution under a supercritical condition to prepare graphene sheets or graphene particles, each of which is as a cluster of the graphene sheets; and (c) separating the graphene sheets or graphene particles, followed by washing and drying. In addition, a method is presented for fabricating a graphene film configured in the form of a thin film using the graphene sheets or graphene particles fabricated according to the method described above.

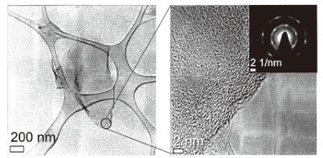

ROBOT CONTROL SYSTEM AND CONTROL METHOD USING THE SAME

20120130539 (US)

KIM, Do Ik / doikkim@kist.re.kr

This invention relates to a robot control system including a robot which receives a final operation signal computed by a mobile terminal and includes one or more driving machines operated according to the received final operation signal. Included in the invention is a mobile terminal which receives a robot status signal and controls the robot by generating the final operation signal for directly driving the one or more driving machines included in the robot.

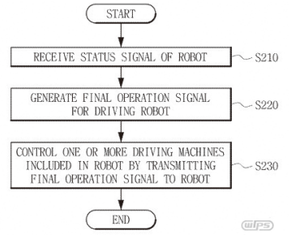

HIGH SENSITIVITY LOCALIZED SURFACE PLASMON RESONANCE SENSOR AND SENSOR SYSTEM USING SAME

20120105857 (US)

Lee, Kyeong Seok / kslee21@kist.re.kr

The present invention relates to a high sensitivity localized surface plasmon resonance sensor and a sensor system using the same, the sensor comprising: a first metal layer including a first metal; a second metal layer arranged parallel to the first metal layer and including a second metal; and a conductive cross-linking layer disposed between the first metal layer and the second metal layer, and made of a third metal with a corrosion response that is different than that of the first metal and of the second metal.

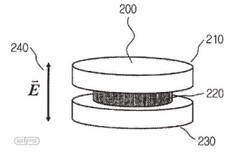

BIOMEDICAL IMPLANTS COMPRISING SURFACE-MODIFIED METAL PARTICLES AND BIODEGRADABLE POLYMERS, ITS USE FOR SUPPRESSING INFLAMMATION, AND PREPARATION METHOD THEREOF

20120070650 (US)

Han, Dong Keun / dkh@kist.re.kr

Disclosed are biomedical implants comprising surface-modified metal particles and biodegradable polymers, their use for suppressing inflammation, and a method for preparing a biomedical material, comprising: (a) modifying the surfaces of basic metal particles with a polymer to obtain surface-modified metal particles; and (b) mixing the surface-modified metal particles with a biodegradable polymer, followed by manufacturing a biodegradable biomedical implant, or coating the resulting mixture on a conventional biomedical implant.

FORWARD OSMOSIS MEMBRANES AND METHOD FOR FABRICATING THE SAME

20120012520 (US)

LEE, Seock Heon / seocklee@kist.re.kr

Disclosed are a forward osmosis membrane capable of ensuring resistance to microorganisms, improving water flux by forward osmosis, and minimizing reverse solute flux by maximizing tortuosity of the membrane, and a method for fabricating the same. The disclosed method for fabricating a forward osmosis membrane includes: preparing a filler material including a non-cellulose polymer; an organic solvent for dissolving the non-cellulose polymer; and a pore-forming agent for inducing pore formation in the non-cellulose polymer; coating the filler material on an osmosis membrane backing; and immersing the osmosis membrane backing coated with the filler material in water, so that the organic solvent and the pore-forming agent are evaporated, and pores are formed in the non-cellulose polymer as the non-cellulose polymer is solidified.

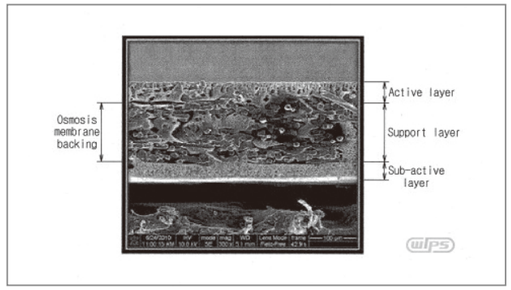

KIST-KMSA Research Camp

February 3-5, 2012

A research camp for the Korea Medical Student Association (KMSA) was held at KIST over a three-day period from February 3-5. Approximately 70 students from a number of universities including Yensei University, Catholic University of Korea and Korea University participated in the camp, whose purpose was to introduce biomedical engineering and brain science research to medical students. Students were organized into seven research areas, depending on their fields of interest: bio-materials, molecular imaging, medical simulation, medical robotics, neurobionics, fundamental neuroscience and subminiature medical devices. They received an introduction and overview of KIST's research labs and research processes as well as specifics regarding work at KIST in biomedical engineering and brain science research. In addition, special lectures were given by Professor Kim Sang Yoon of Asan Medical Center in Seoul and Professor Kim In Shin of Kyungpook University's medical school, who are currently pursuing joint research with KIST for the purpose of advancing fundamental technologies in biomedical engineering through clinically applicable medical technology. Mr. Choi Gui Won, director of the research camp, stated, "I hope that this event will offer an opportunity to enhance the level of interest of medical students on research in basic science, and sustain research opportunities by maintaining close cooperative relationships with researchers in the medical area in the future."

Danish R&D Delegation Visits KIST

February 7, 2012

An R&D delegation from Denmark visited KIST on February 7, 2012, to learn about the institute and to discuss future collaborative activities. The delegation met with Dr. Kil-Choo Moon, President of KIST, to discuss various topics such as Denmark's research strengths, particularly in the areas of biotechnology, energy, and nanotechnology. Dr. Moon introduced the delegation to KIST's main research areas and shared other information of common interest. Following the discussion, the delegation visited the Center for Intelligent Robotics, where they enjoyed a robot demonstration and participated in games using robots designed to assist the elderly. Dr. Mun Sang Kim, Director of the Center for Intelligent Robotics, also gave a brief presentation, highlighting current robot use in Denmark and discussing cases in which robots are used in the treatment of mental diseases.

Visit by Vietnamese Prime Minister and Delegation

March 28, 2012

The Honorable Prime Minister and First Lady of Vietnam (H.E Nguyen Tan Dung and Madame Tran Thanh Kiem) and an accompanying delegation from Vietnam visited KIST on March 28, 2012. The party of the Prime

Minister was greeted at KIST by the Honorable Minister of Education and Science, Ju Ho Lee, the President of KIST, Kil-Choo Moon, and 16 Vietnamese students, participants in the KIST IRDA program. Both parties discussed various means of cooperation in the areas of science and technology, and in particular, expressed a strong inclination towards the establishment of a science and technology research institute in Vietnam with KIST as the model. Following the meeting, all the participants moved to KIST's International Cooperation Center to view a demonstration of the KIST-developed robot *Mahru-Z* and to explore the capabilities of a large multi-touch screen developed at the Center for Cognitive Robotics. A commemorative photography session was organized with the Vietnamese IRDA students. It is anticipated that cooperation between KIST and Vietnam will be further expanded as a result of this visit by the Honorable Prime Minister and accompanying delegates from Vietnam.

Signing Ceremony for Science Sharing Fund Campaign

April 19, 2012

On April 19, 2012, KIST held a signing ceremony to kick off the KIST Science Sharing Fund Campaign whose objective is to have all KIST staff donate 1% of their annual salary to support science sharing activities. KIST's President, Dr. Kil-Choo Moon, proposed the establishment of an operating committee for the KIST Science Sharing Fund when presenting the idea of

"Sharing and Services" during his New Year's address in January of this year. A diverse range of constituent groups within KIST responded to his appeal, including the Research Advancement Council, Women Employees Association, and Labor Union, and an operating committee was subsequently established. The first responsibility of the committee will be to run the KIST Science Sharing Fund Campaign until 2015. The funds raised through this campaign will be used by KIST to promote activities such as scholarship projects for science and engineering students, support to educational institutions in developing countries, and provision of funds for researchers demonstrating exceptional academic research performance. President Moon stated that the campaign for employee contributions will allow the continuous pursuit of activities that can influence society more effectively than existing programs involving just a one-time contribution.

Joint Solar Cell Research Between KIST and Chungnam National University

Technology for the synthesis of a hybrid carbon-nano-tube/metallic-nano-particle for application in counter electrodes in solar cells was developed jointly by Chungnam National University and a KIST research team. A research team from the chemical engineering department of the College of Engineering at Chungnam National University in association with Dr. Lee Jung Gi, Director of the Energy Research Team

at KIST, successfully synthesized a carbon-nanotube/platinum-nanoparticle hybrid material to which platinum-nanoparticles, with a size range of 3~4nm, stably adhered to the surface of a multi-walled carbon-nanotube within ionized liquid at room temperature by applying the plasma reduction method. This process allowed the team to manufacture a conductive nano-coating and develop a dye-sensitized counter electrode for use in solar cells. This technology was selected as the cover article for the 28th issue of the *Journal of Materials Chemistry*, a globally respected academic journal in the field of material chemistry published by the Royal Society of Chemistry (RSC) in England. The development of effective dye-sensitized counter electrodes used in solar cells had been plagued with a number of hard-to-resolve problems, including having to use large quantities of expensive platinum to produce the electrodes, low electrical conductivity and electrical charge transmission resistance, and issues of instability in long-term repetitive usage. However, the team of Professor Choi Ho Seok was able to achieve much higher electric conductivity and electrical charge transmission resistance by using only 5% of the platinum used in the existing sputtering process, and was able to secure stability of the electro-chemical reaction even in 1,000 repetitions.

This technology is expected to be applicable in the future development of low-cost dye-sensitized solar cells, and in particular, represents a key fundamental technology in the development of elastic electrode materials used as conductive coating.

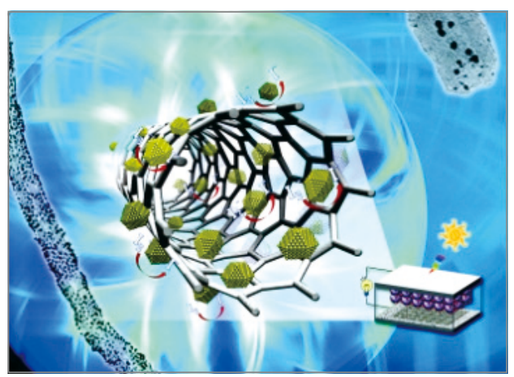

KIST-IRDA Colloquium with Egyptian Ambassador

July 16, 2012

The Egyptian Ambassador to Korea, H.E. Mohamed Elzorkany, was invited to speak at a colloquium on July 16, 2012, at the International R&D Academy (IRDA). IRDA had previously invited other ambassadors to speak as well in order to provide students with special insight into international political and social issues. At the colloquium, the Ambassador presented a lecture and had a lively discussion with over 80 IRDA students on the subject of "International and Political Issues." After the colloquium, students commented that they had gained additional insights into the radical political changes occurring in the Middle East, and on the global future. The Ambassador was welcomed to the colloquium by KIST President Dr. Kil-Choo Moon. The two men discussed further cooperation between Korea and Egypt and expressed their firm commitment and willingness to carry out S&T cooperation through KIST and the IRDA program. The Ambassador confirmed his view that Korea's growth was impressive and its expertise in S&T highly regarded. After the session, the Ambassador met with seven Egyptian IRDA students and encouraged them in their ongoing work. He advised them not to be influenced by their country's political issues, but rather to devote themselves to their academic pursuits for the future of Egypt and the rest of the world.

2012 Korea Science Creativity Festival

August 14-19, 2012

The 2012 Korea Science Creativity Festival was held over a six-day period in August at the KINTEX in Ilsan. This festival, the largest interactive festival of scientific culture in Korea, was organized according to the theme of *Creative World, Seeking Direction from Science* and exhibited more than 400 interactive programs prepared by more than 350 institutions. KIST's booth, which received more than 30,000 visitors during the festival, displayed exhibits in diverse areas such as brain science, water writing, smart windows, a solar city model, film speaker, an interactive snowboard training system, working robots, etc. The interest and participation level of festival visitors was greatly enhanced through the hourly performances of KIST robots as well as a photo-zone installation. The festival received favorable reviews from visitors because of its environment-friendly booths and interactive exhibits geared to children, making it an excellent opportunity to increase awareness of KIST and its outstanding research activities and to generate a positive attitude toward the institute among the general public.

Advanced Fiber Research at KIST

Fiber is the raw material for many products integral to daily life, from textiles to paper to packaging and filters, and the range of its applications is growing. KIST embarked on fiber research immediately after it was established. Following is a brief look at KIST's achievements in this field over time.

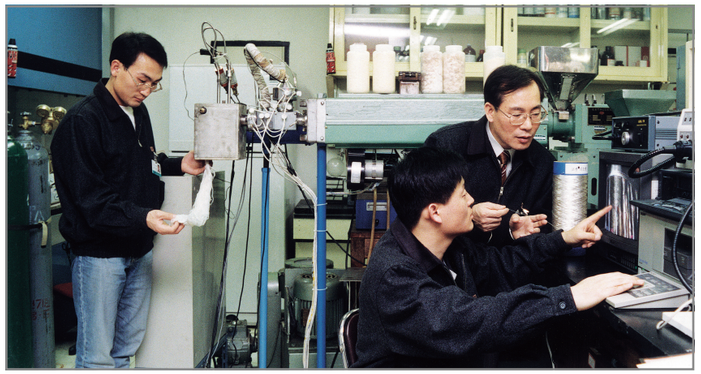

New aramid pulp source technology

• Aramid is a highly-advanced fiber able to protect bullets and withstand 500°C temperatures. U.S.-based DuPont held a virtual monopoly on aramid since development of Kevlar fiber in 1973.

• KIST began work on aramid in 1979. By 1984, the research team of Dr. Han Sik Yoon and Dr. Tae Won Son of KIST's polymer research department, in collaboration with Kolon Co., Ltd., developed the source technology for aramid pulp. They also simplified aramid production, reducing costs by two-thirds compared to Kevlar.

• Korea thus became only the third country, after the U.S. and the Netherlands, to master aramid technology.

• The KIST-developed fiber exhibited outstanding thermal and abrasion resistance, making it useful for applications in automobile brakes and clutches, engine gaskets, and construction.

• Given this fiber's unique micro-structure, it won patents in Korea, Europe and Japan. Nature devoted three pages to it in 1987.

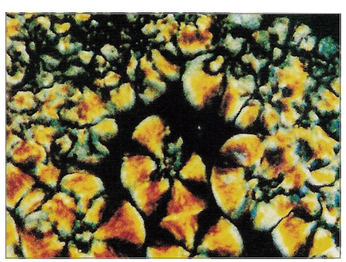

Non-polluting process for making artificial silk

• The production of artificial silk from cellulose involved the use of noxious chemicals that posed risks for both occupational health and environmental pollution.

• KIST began work on a new kind of artificial silk in 1989. After more than 13 years of research, the team of Dr. Wha Seop Lee and Dr. Seong Mu Jo of KIST's polymer research department succeeded in developing a new process that makes a product as comfortable as natural fiber but twice as strong as existing artificial silk. The new fiber, works well in blended-spinning applications with other natural and synthetic fibers.

• The new process used an aminoxide as a solvent. It is harmless to the human body and can be fully retrieved for recycling, eliminating both occupational health and pollution hazards in the production of artificial silk.

• In 2001 Korea became the first country in Asia to produce Lyocell, a fiber made with amineoxide solvent and cellulose extracted from wood pulp. As the conventional production procedures involving toxic materials, viscose process, have gradually been replaced, KIST's research on nontoxic approaches has been credited with helping to position Korea to expand production and export of high value-added artificial silk products.

Breakthrough in a separator with thermal resistance for larger batteries

• Separator with high thermal resistance and good power performance in mid- to large-size secondary batteries is very important because of increasing the risk of explosive heat generation.

• KIST's Center for Materials Architecturing the team of Dr. Seong Mu Jo, developed a new kind of separator with high thermal resistance using ultra-finefiber in the range of several nm to several thousand nm.

• This new separator material offers a greater surface area, a high porosity and superior power performance. It also shows minimal thermal contraction (less than 5%) and outstanding thermal stability even at 200°C.

• The new separator material is expected to have applications in batteries for electric vehicles, portable devices, and energy storage/power equipment.

• KIST's technology was transferred to a global chemical company, DuPont.

Converting agricultural waste into energy? We can do that!

This research center has been selected for a special interview in order to provide a brief introduction to the center and its working environment as well as highlight some of its activities, researchers and staff.

A team led by KIST's Dr. Dong Jin Seo has developed technology for the production of fuel ethanol using agricultural waste and has completed construction of a pilot plant in Indonesia.

Opportunity for win-win growth in energy development

An Indonesian laments: *There are so many palm trees in Indonesia; being able to produce palm oil from palm trees has been a huge help in our daily lives. However, we have no means of dealing with the residues generated by the extraction of oil and this has become a source of major stress.*

A KIST member answers: *Do not worry about palm tree residues—we will turn the residues into fuel!*

Dr. Dong Jin Seo of the Clean Energy Research Center at KIST has been extremely busy with the development of a pilot plant for the production of bio-ethanol using agricultural waste. Although he is fully occupied with directing research and traveling frequently between Indonesia and Korea, he nonetheless gets great pleasure out of providing scientific support to the Indonesians.

KIST and Changhae Engineering have developed production technology for fuel ethanol using agricultural waste, such as palm tree residues, and have established a pilot plant at the Chemical Research Lab under the management of the Indonesian Science Institute in Serpong, Indonesia. Dr. Seo has been appointed head of this project.

The project, executed as part of the *East Asia Climate Partnership Project* by the Korea International Cooperation Agency (KOICA), is unlike existing aid programs that simply provide one-way support in the areas of education, public health and medicine, agriculture, forestry and fisheries, and public administration. Instead, it capitalizes on opportunities for win-win growth in which both the donor and recipient of aid gain tangible benefits from the project. It has further significance by serving as a model for Official Development Assistance (ODA)* projects in the area of science and technology. The win-win aspect involves the construction of plants in Indonesia, which gains the technological know-how from Korea to turn palm tree waste into a marketable ethanol, while Korea can then import ethanol at a lower cost than could otherwise be found on the world market.

Dr. Seo states, "Indonesia is the world's biggest producer of palm oil, which is the raw material for bio-diesel, and as the country with the second largest area of tropical forest in the world, it is immensely interested in national development of bio-energy… unlike the existing ODA projects, it is significant that this project has established a new model for win-win between the provider and recipient of the aid."

The biggest advantage of the pilot plant that Dr. Seo's team developed is that next-generation bio-ethanol technology, yet to be commercialized globally, will be applied. The existing first-generation technology produces ethanol from food resources such as sugarcane or corn, but second-generation technology produces fuel ethanol by using agricultural waste.

Dr. Seo emphasizes that methods for producing fuel by using agricultural waste should continue to be researched despite numerous technological difficulties. He states, "obtaining bio-ethanol from sugarcane, wheat or corn, etc., is the easiest method, but this presents the problem of sustainability, as there are a large number of children suffering from hunger."

Near-death experiences in search of trees

I personally explored forests in Indonesia—Sumatra Island, Java Island, and others—in search of the most appropriate timber substance for conversion into fuel ethanol, and even had near-death experiences in the process. (Dr. Seo)

In December 2010, Dr. Seo, and other researchers were tasked with finding agricultural waste with a timber biomass substance appropriate for conversion into ethanol. They visited and explored forests in Indonesia.

The team lived in Indonesia with the assistance of the local people. Although the country's environment and cultures are completely different from Korea's, its kind, empathetic residents enabled the researchers to successfully complete their exploration. However, one facet of the local personality took the team by surprise--the locals were very aggressive when driving.

"We drove into the forest with the help of locals and found another car approaching us from the opposite side. Although our car should have reduced its speed, our driver continued to drive very fast. We were really surprised and alarmed. When we came very close to each other, our driver slowed down. Although we had been seriously concerned that we could die or sustain injuries from a vehicle accident at the time, we quickly became accustomed to such aggressive local driving habits," Dr. Seo says, laughing.

In addition, the team was constantly anxious that there could be setbacks to the schedule because the locals had a different concept of time than always-in-a-hurry Koreans.

Dr. Seo explains, "the locals had a tendency to work at a slower pace than Koreans because they live with such hot weather. However, because of their accommodating and kind personalities, they picked up speed when we asked them to work at a quicker pace. From their point of view, we probably were not welcome when it came to work, but they worked really hard nonetheless. We were really grateful for their efforts."

Palm trees lacked promise

During exploration of the forest, the team collected a total of four candidate trees based on the following criteria: possibility of conversion into fuel ethanol; ease of collection; and abundance of the tree. Initially, the palm tree did not seem the best choice.

"In fact, the palm tree was the third- to fourth-ranked candidate because it was too hard. Although converting a very hard timber substance into bio-ethanol is a difficult task, we took up the challenge, anyway." Dr. Seo justifies the reason for his choice by stating, "being able to extract bio-ethanol from extremely hard palm trees means that we can extract bio-ethanol from any tree." He adds, "there was an abundance of palm oil residues as there was no means of discarding


EFB Powder


EFB Feeding

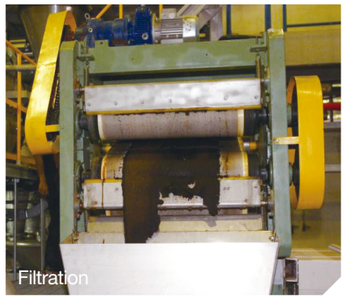
Filtration


Explosion

them other than burning them. In addition, it was categorized as an economically appropriate material because of the excellent collection route for palm oil residues."

Although the quantity of fuel ethanol that can currently be obtained from the pilot plant is only 10 liters per day, the team is planning to expand production capacity to 20,000-30,000 liters per day and commercialize the production once the technological potential is confirmed. Dr. Seo, in addressing the question that the yield from palm tree residue is too limited at the moment, emphasizes that his task is essential for the future energy security of Korea, Indonesia, and much of the world.

He says, "we should not be viewing these issues simply on the basis of current economic values. It is an important task to continue and further advance such projects for the sake of our descendants as the price of oil continues to increase and CO_2 emissions contribute to global warming."

Dr. Seo's team departed for Indonesia again in the middle of June after this interview was completed. Although these trips were initially difficult, in part because it was so hard to adjust to different culinary tastes, team members now find themselves longing for dishes containing local Indonesian spices. The team is planning to activate and operate the completed plant in Indonesia and to educate the locals once again on operating methods so that they can run the plant by themselves. In addition, the team, along with other interested parties, is planning to hold seminars related to the facility.

Official Development Assistance (ODA): Flow of funds provided by public organizations such as the central or local government of a country, or an institution that provides aid to developing countries or international organizations, for the enhancement of economic development and welfare in the developing country. The Development Assistant Committee (DAC), which is one of the representative committees of the OECD, is the cornerstone of this project. Korea joined the DAC as the 24th member country in 2010.

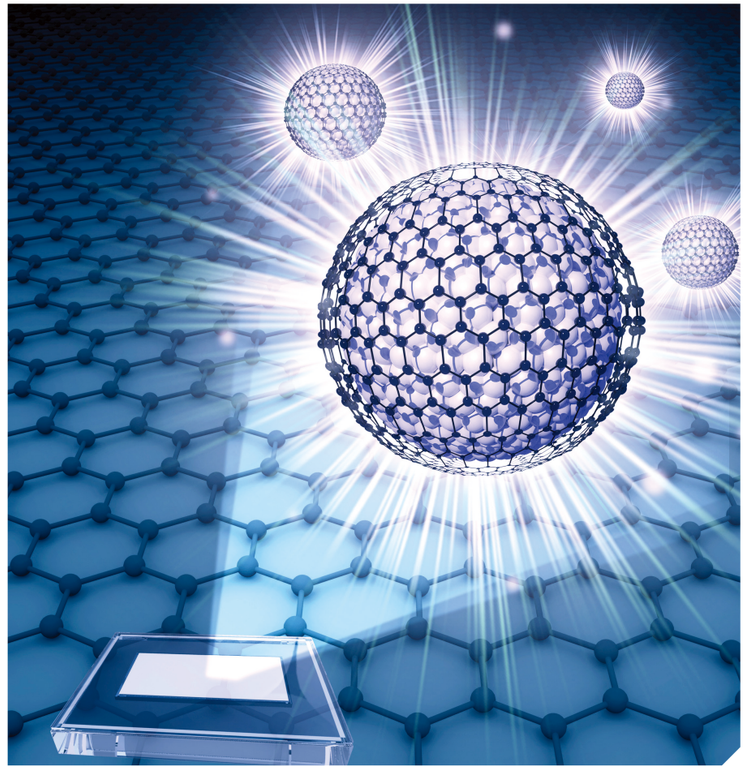

Cover: **Image of a light emission generated by using a quasi-ZnO-graphene QD as an emitting layer in a light-emitting diode.**
Taken from the technical review of Dr. Dong-Ick Son and Dr. Won-Kook Choi (see page 32).

Editorial Information

Editor-in-Chief
Byung Gwon Lee

Editorial Board Members
Hae-Young Koh
Hyun Kwang Seok
Il Ki Han
Joonyeon Chang
Youngsoon Um
Seok Won Hong
Jongjoo Kim
Seung Yun

Managing Editor
Kwihyang Han
kiwihyang@kist.re.kr
Editorial Office Telephone
+82-2-958-6313
Web Address
www.kist.re.kr/en

English Advisory Services
Anne Charlton
The Final Word Editing Services
the_final_word@live.com

Korea Institute of Science and Technology

Hwarangno 14–gil 5, Seongbuk–gu, Seoul 136–791, Republic of Korea
Tel +82–2–958–6313 www.kist.re.kr/en
E–mail kiwihyang@kist.re.kr